

UC San Diego

UC San Diego Electronic Theses and Dissertations

Title

Flexible finite-element modeling of global geomagnetic depth sounding

Permalink

<https://escholarship.org/uc/item/3f92r8tr>

Author

Ribaudo, Joseph Thomas

Publication Date

2011

Peer reviewed|Thesis/dissertation

UNIVERSITY OF CALIFORNIA, SAN DIEGO

**Flexible Finite-Element Modeling of Global Geomagnetic Depth
Sounding**

A dissertation submitted in partial satisfaction of the
requirements for the degree
Doctor of Philosophy

in

Earth Sciences

by

Joseph Thomas Ribaudo

Committee in charge:

Professor Catherine G. Constable, Chair
Professor Randolph E. Bank
Professor Steven C. Constable
Professor Jeffrey S. Gee
Professor Robert L. Parker

2011

Copyright
Joseph Thomas Ribaud, 2011
All rights reserved.

The dissertation of Joseph Thomas Ribaud is approved,
and it is acceptable in quality and form for publication
on microfilm and electronically:

Chair

University of California, San Diego

2011

DEDICATION

Dedicated to Adrienne, my wife and soul mate,
and to our daughter Nola.

TABLE OF CONTENTS

	Signature Page	iii
	Dedication	iv
	Table of Contents	v
	List of Figures	vii
	List of Tables	x
	Acknowledgements	xi
	Vita and Publications	xii
	Abstract of the Dissertation	xiv
Chapter 1	Introduction	1
	1.1 Background and Motivation	1
	1.2 Previous Work	5
	1.3 Outline	8
	References	10
Chapter 2	Scripted Finite-element Tools for Global Electromagnetic In- duction Studies	13
	2.1 Introduction	14
	2.2 Forward Modeling in 2D and 3D for Geomagnetic Depth Sounding (GDS)	17
	2.2.1 Governing Equations	18
	2.2.2 Implementation in FlexPDE	24
	2.2.3 Primary Field Models	25
	2.2.4 Response Functions	27
	2.3 Validation	28
	2.3.1 Frequency-domain Validation	28
	2.3.2 Time-domain Validation	35
	2.4 Conclusions	39
	2.5 Appendix: Analytic Solution for Earth Model in Uniform Primary Field	39
	2.6 Acknowledgments	42
	References	43

Chapter 3	The effect of on global response function estimates of Earth’s rotation through an asymmetric source field	47
	3.1 Introduction	48
	3.2 Method	49
	3.2.1 The Dipole Assumption	52
	3.2.2 Adding a Quadrupole Source	53
	3.2.3 Adding Rotation	62
	3.3 Conclusions	77
	3.4 Acknowledgments	78
	References	79
Chapter 4	FlexPDE Simulations For Comparison Of Global Induction Codes	81
	4.1 Introduction	81
	4.2 Model 1: North/South Hemispheres	83
	4.3 Model 2: East/West Hemispheres	85
	4.4 Model 3: Eccentrically Nested Spheres	104
	4.5 Model 6: 3D Surface Conductance Map Over Radial Conductivity Model	124
	4.6 Summary	146
	4.7 Acknowledgments	146
	References	147
Chapter 5	Conclusions and Future Outlook	149

LIST OF FIGURES

Figure 2.1:	Solution domain	16
Figure 2.2:	Global induction snapshot	17
Figure 2.3:	Amperian loop	23
Figure 2.4:	Earth model solutions vs. period	28
Figure 2.5:	Earth model solutions vs. radius	30
Figure 2.6:	Earth model solutions vs. colatitude	31
Figure 2.7:	Earth model c -responses vs. period	32
Figure 2.8:	Eccentrically nested spheres solutions vs. radius	34
Figure 2.9:	Rotating conductor snapshot	36
Figure 2.10:	Rotating conductor residuals	37
Figure 3.1:	Response functions vs. period	55
Figure 3.2:	Bias in $c_1(T)$ for a non-rotating Earth with Y_2^1 contamination .	57
Figure 3.3:	Bias in $c_1(T)$ for a non-rotating Earth with Y_2^1 contamination: geometrical effect	58
Figure 3.4:	Bias in $c_1(T)$ for a non-rotating Earth with Y_2^1 contamination: amplitude effect	59
Figure 3.5:	Bias in $c_1(T)$ for a non-rotating Earth with $\cos \phi$ -weighted Y_1^0 contamination	61
Figure 3.6:	Effective period vs. source period in a rotating Earth	64
Figure 3.7:	Comparison of synthetic $c_1(T)$ for periods of 5 and 10 days . .	69
Figure 3.8:	Bias in $c_1(T)$ for a rotating Earth with Y_2^1 contamination: scalar method	70
Figure 3.9:	Bias in $c_1(T)$ for a rotating Earth with Y_2^1 contamination: vector method	71
Figure 3.10:	Bias in $c_1(T)$ for a rotating Earth with $\cos \phi_1$ -weighted Y_1^0 pri- mary field: vector method	73
Figure 3.11:	Fit to BEM bias in $c_1(T)$ for Y_2^1 contamination	74
Figure 3.12:	Parameters for previous figure	75
Figure 3.13:	Fit to BEM bias in $c_1(T)$ for $\cos \phi_1$ -weighted Y_1^0 primary field .	76
Figure 3.14:	Parameters for previous figure	76
Figure 4.1:	Model 1 solutions	86
Figure 4.2:	Model 2 solutions: B_r along $\phi = 0.5^\circ$	88
Figure 4.3:	Model 2 solutions: B_θ along $\phi = 0.5^\circ$	89
Figure 4.4:	Model 2 solutions: B_ϕ along $\phi = 0.5^\circ$	90
Figure 4.5:	Model 2 solutions: B_r along $\phi = 90.5^\circ$	91
Figure 4.6:	Model 2 solutions: B_θ along $\phi = 90.5^\circ$	92
Figure 4.7:	Model 2 solutions: B_ϕ along $\phi = 90.5^\circ$	93
Figure 4.8:	Model 2 solutions: B_r along $\phi = 180.5^\circ$	94
Figure 4.9:	Model 2 solutions: B_θ along $\phi = 180.5^\circ$	95

Figure 4.10: Model 2 solutions: B_ϕ along $\phi = 180.5^\circ$	96
Figure 4.11: Model 2 solutions: B_r along $\phi = 270.5^\circ$	97
Figure 4.12: Model 2 solutions: B_θ along $\phi = 270.5^\circ$	98
Figure 4.13: Model 2 solutions: B_ϕ along $\phi = 270.5^\circ$	99
Figure 4.14: Model 2 solutions: B_r along $\theta = 45.5^\circ$	100
Figure 4.15: Model 2 solutions: B_θ along $\theta = 45.5^\circ$	101
Figure 4.16: Model 2 solutions: B_ϕ along $\theta = 45.5^\circ$	102
Figure 4.17: Model 3 solutions: B_r along $\phi = 0^\circ$	106
Figure 4.18: Model 3 solutions: B_θ along $\phi = 0^\circ$	107
Figure 4.19: Model 3 solutions: B_ϕ along $\phi = 0^\circ$	108
Figure 4.20: Model 3 solutions: B_r along $\phi = 90^\circ$	109
Figure 4.21: Model 3 solutions: B_θ along $\phi = 90^\circ$	110
Figure 4.22: Model 3 solutions: B_ϕ along $\phi = 90^\circ$	111
Figure 4.23: Model 3 solutions: B_r along $\phi = 180^\circ$	112
Figure 4.24: Model 3 solutions: B_θ along $\phi = 180^\circ$	113
Figure 4.25: Model 3 solutions: B_ϕ along $\phi = 180^\circ$	114
Figure 4.26: Model 3 solutions: B_r along $\phi = 270^\circ$	115
Figure 4.27: Model 3 solutions: B_θ along $\phi = 270^\circ$	116
Figure 4.28: Model 3 solutions: B_ϕ along $\phi = 270^\circ$	117
Figure 4.29: Model 3 solutions: B_r along $\theta = 45^\circ$	118
Figure 4.30: Model 3 solutions: B_θ along $\theta = 45^\circ$	119
Figure 4.31: Model 3 solutions: B_ϕ along $\theta = 45^\circ$	120
Figure 4.32: Model 3 solutions: B_r along $\theta = 135^\circ$	121
Figure 4.33: Model 3 solutions: B_θ along $\theta = 135^\circ$	122
Figure 4.34: Model 3 solutions: B_ϕ along $\theta = 135^\circ$	123
Figure 4.35: Model 6 conductance map	125
Figure 4.36: The coast effect	127
Figure 4.37: Model 6 solutions: B_r along $\phi = 0^\circ$	128
Figure 4.38: Model 6 solutions: B_θ along $\phi = 0^\circ$	129
Figure 4.39: Model 6 solutions: B_ϕ along $\phi = 0^\circ$	130
Figure 4.40: Model 6 solutions: B_r along $\phi = 90^\circ$	131
Figure 4.41: Model 6 solutions: B_θ along $\phi = 90^\circ$	132
Figure 4.42: Model 6 solutions: B_ϕ along $\phi = 90^\circ$	133
Figure 4.43: Model 6 solutions: B_r along $\phi = 180^\circ$	134
Figure 4.44: Model 6 solutions: B_θ along $\phi = 180^\circ$	135
Figure 4.45: Model 6 solutions: B_ϕ along $\phi = 180^\circ$	136
Figure 4.46: Model 6 solutions: B_r along $\phi = 270^\circ$	137
Figure 4.47: Model 6 solutions: B_θ along $\phi = 270^\circ$	138
Figure 4.48: Model 6 solutions: B_ϕ along $\phi = 270^\circ$	139
Figure 4.49: Model 6 solutions: B_r along $\theta = 45^\circ$	140
Figure 4.50: Model 6 solutions: B_θ along $\theta = 45^\circ$	141
Figure 4.51: Model 6 solutions: B_ϕ along $\theta = 45^\circ$	142
Figure 4.52: Model 6 solutions: B_r along $\theta = 135^\circ$	143

Figure 4.53: Model 6 solutions: B_θ along $\theta = 135^\circ$ 144
Figure 4.54: Model 6 solutions: B_ϕ along $\theta = 135^\circ$ 145

LIST OF TABLES

Table 2.1: Electrical conductivities used for validating Earth model simulations	30
Table 3.1: Electrical conductivities used for asymmetry studies	49
Table 4.1: Models 1 and 2 conductivity	83
Table 4.2: Model 1 conductance	83
Table 4.3: Model 1 runtimes	85
Table 4.4: Model 2 conductance	87
Table 4.5: Model 2 runtimes	87
Table 4.6: Model 3 runtimes	105
Table 4.7: Models 6 conductivity	124
Table 4.8: Model 6 runtimes	124

ACKNOWLEDGEMENTS

I am thankful for the support of my doctoral committee, and for their helpful suggestions with regard to the research presented in this body of work. As an advisor, coauthor, teacher, and friend Cathy Constable has been a constant source of insight and inspiration, and has spent a great deal of time guiding the development of this work and my education. She has helped me become a part of the scientific community by introducing me to other researchers in the field of global induction, by encouraging me to present at conferences and to attend the International Swarm meetings, and by helping me obtain funding through NASA's Earth and Space Science Fellowship. Steve Constable has included me in his group meetings, cruises, and his Seafloor Electromagnetics Consortium conferences. Steve introduced me to many exploration geophysicists, and has always been available to answer questions and provide insight. Bob Parker is a coauthor and has provided many insightful suggestions for my research. Together, Steve and Bob have taught several classes on electromagnetic methods and Earth conductivity that have been invaluable to me. Jeff Gee and Randy Bank have been consistently available and helpful in all of their duties as members of my committee.

Chapter 2, in full, has been submitted for publication to *Geophysical Journal International* as: Ribaudo, J.T., Constable, C.G., & Parker, R.L., Scripted nite element tools for global electromagnetic induction studies. The dissertation author was the primary investigator and author of this paper.

Alexei Kuvshinov and Jakub Velimský contributed solutions to Models 1 and 2 in Chapter 4. Jakub Velimský also provided the analytic solution for Model 3.

VITA

1996	B.A., Philosophy <i>summa cum laude</i> , Arizona State University
2003	B.S., Physics <i>summa cum laude</i> , Arizona State University
2003	B.A., Mathematics <i>summa cum laude</i> , Arizona State University
2003-2011	Graduate Teaching Assistant, University of California, San Diego
2005-2011	Graduate Student Researcher, Scripps Institution of Oceanography, University of California, San Diego
2011	Ph.D., Earth Science, Scripps Institution of Oceanography, University of California, San Diego

PUBLICATIONS

Ribaudo, J.T., Constable, C.G., Parker, R.L. (*submitted*), Scripted finite element tools for global electromagnetic induction studies, *Geophys. J Int.*

PRESENTATIONS

Ribaudo, J.T., Constable, C.G., (2007) Scripted Finite Element Methods Applied to Global Geomagnetic Induction, *Eos Trans. AGU*, 88(52), Fall Meet. Suppl., Abstract GP32A-05

Ribaudo, J.T., (2008) Can off-the shelf finite element codes be used for EM modeling?, Seafloor Electromagnetics Consortium Conference, La Jolla, CA

Ribaudo, J.T., Constable, C.G., (2008) Towards Realistic Global Geomagnetic Induction Modeling Using Scripted Finite Element Methods, *Eos Trans. AGU*, 89(53), Fall Meet. Suppl., Abstract GP51C-03

Ribaudo, J.T., (2009) Using off-the shelf finite element codes for EM modeling, Seafloor Electromagnetics Consortium Conference, La Jolla, CA

Ribaudo, J.T., Constable, C.G., Parker, R.L., (2009) Finite Element Modeling for Swarm Electromagnetic Induction Studies, Proceedings of ESA's Second Swarm International Science Meeting, WPP-303, Abstract S3-P02

Ribaudo, J.T., Constable, C.G., Parker, R.L., (2009) Simulation of Satellite Observations of Induced Magnetic Fields using Scripted Finite Element Methods, Eos Trans. AGU, 90(52), Fall Meet. Suppl., Abstract GP43C-07

Constable, C.G., Ribaudo, J.T., Smith, L., (2010) Global Geomagnetic Depth Sounding Using Satellite Data: Source Considerations and Response Function Estimates, IAGA WG 1.2 on Electromagnetic Induction in the Earth 20th Workshop, Abstract S9-01

Ribaudo, J.T., Constable, C.G., (2010) Simulating Geomagnetic Depth Sounding using a Time-domain Finite Element Method: effects of asymmetric external source fields, Abstract GP21B-05 presented at 2010 Fall Meeting, AGU, San Francisco, Calif., 13-17 Dec.

AWARDS AND HONORS

National Merit Scholar (1990)

Arizona State Regents Scholarship, ASU (1992 - 1996)

Arizona Power Authority Scholarship, ASU (2002)

SHIP recipient, UCSD Physics Department (2003)

NASA Travel Grant (2006)

NASA Earth and Space Science Fellowship Grant (2007 - 2010)

ABSTRACT OF THE DISSERTATION

Flexible Finite-Element Modeling of Global Geomagnetic Depth Sounding

by

Joseph Thomas Ribaldo

Doctor of Philosophy in Earth Sciences

University of California, San Diego, 2011

Professor Catherine G. Constable, Chair

Time-varying primary magnetic fields generated outside Earth by the magnetospheric ring current induce electrical currents in Earth's interior, which give rise to secondary magnetic fields with a complementary geometry. Geomagnetic depth sounding involves the analysis of magnetic field data to compute frequency-dependent response functions which yield information about the electrical conductivity of Earth's interior. I explore methods and results of forward-modeling global electromagnetic induction under a variety of assumptions about Earth conductivity and the spatial structure of the primary field. I begin by developing computational tools to perform time- and frequency-domain simulations of global induction in models with arbitrary conductivity and primary field structure us-

ing FlexPDE, a general-purpose software package that employs the finite-element method to solve partial differential equations. The method is shown to produce solutions with better than 1% accuracy when the simulated fields and response functions are compared to analytic solutions for a variety of problems in electromagnetic induction, and to qualitatively reproduce fields and response functions measured by satellites and observatories.

The technique is employed in combination with analytic methods to explore the effect on the response of Earth models to primary fields with asymmetric structure. Standard methods of producing response functions from scalar and vector magnetic data are compared, and scalar methods are found to generate responses with significantly greater spatial bias for models with non-zonal fields. I develop the mathematical formulation for including Earth-rotation in the forward models, and use it to calculate frequency-dependent estimates of the amount of non-zonal structure required to produce previously reported local-time bias in empirical satellite response functions.

Because it is difficult to validate solutions to induction problems that lack analytic solutions, we participate in an ongoing project with other researchers who simulate the global induction problem with different methods. We compare the synthetic fields calculated with the FlexPDE method to those calculated with the integral equation method and with the time-domain spectral method for a variety of conductivity models.

Chapter 1

Introduction

1.1 Background and Motivation

Knowledge of electrical conductivity (σ) is useful for characterizing certain properties of Earth's mantle including temperature, composition, and melt, water, and volatile content. Electromagnetic induction is governed by a diffusion equation, which makes induction studies less sensitive than seismic studies. However electrical conductivity in Earth varies over a wider range than density and seismic velocity, ranging from around 10^{-5} S/m in igneous rocks, to 5×10^5 S/m in the core (Constable, 2007). Conduction studies provide an independent means of gaining knowledge of processes in Earth's interior, including mantle convection and tectonic activity, and are an important complement to seismic studies, which are not sensitive to the same parameters. Conductivity studies have been used to test the Bercovici and Karato's (2003) transition-zone water filter hypothesis (Medin *et al.*, 2007), to look for the post-perovskite phase in the D'' layer at the base of the mantle (Velimsky, 2010), and to perform numerous examinations of the crust and upper mantle, including hydrocarbon exploration (Constable and Srnka, 2007), gas hydrate studies (Weitemeyer *et al.*, 2011), and exploration of undersea volcanoes (Myer *et al.*, 2006).

Geomagnetic depth sounding (GDS), or the use of magnetic field measurements to probe large-scale electrical conductivity, traces its beginnings to the first observations of electrical current in Earth's crust (or *telluric currents*), which oc-

curred in Norway in the early 19th century, and coincided with the advent of the telegraph. Electrical cables were grounded at both ends in order to provide an extended equipotential circuit that could be used for communication over hundreds of miles by messages encoded in voltage signals. Magnetic storms were known by then, having been discovered in 1722 (Graham, 1724), and during a large magnetic storm on April 16th, 1938 spontaneous electric potential differences of several hundred volts, much larger than standard telegraph voltages, were observed on these cables (Chapman and Bartels, 1940). Similar observations were made in England in 1847 (Barlow, 1849), and in Europe and America in 1859, with simultaneous observations of an especially large aurora (Clement, 1860).

The physical theory connecting magnetic storms and telluric currents is largely attributable to Gauss' separation of Earth's field into internal and external spherical harmonic components in 1839, and Maxwell's equations for electromagnetism in 1864. The latter was foreshadowed by the 1819 observations of Ørsted and Ampere regarding the magnetic fields produced by electric currents, and Faraday's empirical discovery of electrical currents induced by time-varying magnetic fields in 1831. Continuous magnetic field measurements began at the Greenwich observatory in 1847 with the invention of photographic recording techniques, and the first dedicated telluric current measurement circuits began operation at the same location in 1865 (Chapman and Bartels, 1940), in the form of perpendicular, grounded 15 km grounded cables. These developments allowed similarities between the two phenomena to be studied empirically.

Early mathematical methods for using magnetic fields for mantle conductivity studies involved modeling Earth as a smaller conductive sphere surrounded by an insulating shell, and estimating the thickness of the shell (250 km) based on magnetic measurements (Chapman, 1919). Later, it was shown that the magnetic observations were inconsistent with any conductivity model that does not increase with depth (Lahiri and Price, 1939), and the first non-uniform profile of estimated Earth conductivity was produced, extending to a depth of about 1000 km and proposing a rapidly increasing conductivity at a depth between 600 and 700 km, consistent with a seismic horizon at this depth. Attempts were made to

use the outward propagation of the secular variation of Earth’s core field to probe the lower mantle (McDonald, 1957), but it was later shown that such attempts were unreliable in the absence of independent information about the signal at the core-mantle boundary (Backus, 1983).

Banks (1969) used the first 3 harmonics of the 27-day solar rotation cycle and its associated recurrence of magnetic storms to produce a conductivity profile to a depth of 2000 km, under the assumption that the field from the magnetospheric ring current is uniform near Earth, and suggested a sharp conductivity increase at 400 km depth. Based on the attribution of this increase to the phase transition between olivine and spinel, he used this result to estimate the temperature of the mantle between 300 and 1000 km depth.

Banks also introduced the c -response for use with data collected from a single observatory under the assumption that the primary field is described by one spherical harmonic of degree n , and that the conductivity profile is purely radial:

$$c_n(\omega) = \frac{a \tan \theta B_r(\omega)}{2 B_\theta(\omega)}, \quad (1.1)$$

where ω is the radial frequency of the time-variations, a is Earth radius, r and θ are the radius and geomagnetic colatitude in a spherical coordinate system with its origin at Earth’s center, and B_r and B_θ are the associated components of the magnetic field. The c_n -response forms the basis of the GDS method. It was later adapted by for magnetotelluric studies, and its real part shown to be a measure of the depth of penetration of electromagnetic fields into Earth (Weidelt, 1972).

The development of a global network of magnetic observatories has allowed for the analysis of simultaneous fields in multiple locations. A modification of c_n exists for use under the assumption of more than one spherical harmonic term (Schmucker, 1970):

$$c = \frac{B_r}{\nabla_\tau \cdot \mathbf{B}_\tau}, \quad (1.2)$$

where $\nabla_\tau \cdot \mathbf{B}_\tau$ is the horizontal part of the divergence.

In combination with MT impedance estimates, (1.2) may be employed in a method to study lateral variations in Earth conductivity (Schmucker, 2003). For good results, the magnetic measurements must have sufficient coverage to

provide reliable estimates of lateral derivatives of the fields, which only occurs in Europe (Kuvshinov, 2010). By using local measurements of B_r from 24 European observatories directly in (1.2), and using the corresponding B_θ measurements to estimate spherical harmonic expansions of the field, Olsen calculated a European average of c for periods between 3 hours and one year (Olsen, 1998, 1999).

The advent of high-precision magnetic satellite missions came with NASA's 6-month Magsat mission in 1979-1980. This was followed by Denmark's Ørsted, Germany's CHAMP, and SAC-C, which is a cooperative project between NASA and Argentina. In combination, these last three missions have provided over a decade of continuous measurements of Earth's magnetic field at satellite altitude. The ESA project SWARM is expected to begin in 2012, and will include 3 CHAMP-style satellites flying in formation, which will help estimate the spatial structure of the magnetic fields.

Satellite data have some advantages over ground observatories. Magnetic satellites fly in polar orbits that are either stationary or nearly so with respect to local time, with orbital periods of around 100 minutes. This provides global coverage that includes the oceans, which are generally neglected by observatories, but also presents special challenges. Satellites are unable to differentiate between the time variation of the fields and their own motion through fields with spatial variation. In order to be useful for GDS, care must be taken to remove fields from crustal and atmospheric sources, as well as those from the core and its secular variation from the data. This is often done by subtracting those fields with a model like CHAOS (Olsen *et al.*, 2006), or CM4 (Sabaka *et al.*, 2004), and by carefully selecting data to sample only nightside midlatitudes, since these models usually do not adequately remove the auroral and field-aligned signals near the poles and Sq signals on the dayside. Lacking simultaneous coverage, satellites also have difficulty distinguishing higher degree and order structure in the primary fields. As such, uniform primary fields are generally assumed in the inversions of satellite data.

Estimates of depth-dependent Earth conductivity that have been produced from measurements of single satellites include those of Didwall (1984) using POGO

data, Olsen *et al.* (2003) using CHAMP data, and Constable and Constable (2004) using Magsat data. In these cases, the satellite data for each half-orbit is used to produce snapshots of the internal and external dipole coefficients at roughly 100 minute intervals. Cross-spectral methods are used to calculate $c_1(\omega)$, which is then inverted for mantle conductivity. Conductivity estimates have also been produced from simultaneous analysis of the Ørsted, CHAMP, and SAC-C data in a similar manner (Kuvshinov and Olsen, 2006), but these data do not lend themselves to analysis on a half-orbit basis because the satellites are not precisely coordinated. Instead cubic B-splines were used to parameterize their time-dependence.

Time-domain inversion of satellite magnetic data has been performed by Velímský *et al.* (2006) to generate 1D conductivity estimates from 11 magnetic storms measured by CHAMP in 2001–2003. Also operating in the time-domain, Martinec and Velímský (2009) used 1 year of CHAMP data to produce estimates of the lateral variation of electrical conductivity in the upper- and mid-mantle of 20% and 4%, respectively. In anticipation of the upcoming SWARM mission, fully 3D approaches to time- and frequency-domain inversion of satellite data have been introduced (e.g. Kuvshinov *et al.*, 2010), but not yet implemented.

1.2 Previous Work

An inherent requirement of all GDS inversion methods is the ability to accurately calculate the induced magnetic field for given conductivity and primary field structure. This is known as the *forward problem*, and is done by solving low-frequency approximations of Maxwell’s equations in the form of differential or integral equations. The body of work in this document describes my work in calculating and applying forward solutions with a combination of analytic procedures and numerical calculations. Other techniques for solving these equations exist, and have been used to explore global induction. Each has advantages and disadvantages.

My numerical solutions are calculated with a general-purpose differential equation solver called FlexPDE, that employs the *finite-element method* (FEM).

This package was chosen for its flexibility and ease of use. Since it is not designed to solve a particular physical problem, it can be employed for any problem that can be described with a soluble differential equation. The finite-element method is a fairly complicated problem, that uses an irregular numerical mesh as a computation domain, and iteratively solves the Galerkin (see Reddy, 1993) integral form of the governing equations in each cell of the domain until the estimated error falls below a given threshold. FlexPDE is controlled by a fairly simple script that allows the user to specify the qualitative details of the solution domain, the differential equations to be solved, and the error tolerance, but leaves the mathematical and computational details of mesh construction, integral formulation of the differential equations, solution algorithm, and error estimation to be controlled by pre-existing, selectable software routines. This means that solutions to a great number of global induction problems can be computed from a variety of solution routines with fairly minor modifications of a script. This allows the researcher to concentrate on the physical problems being simulated instead of on code production.

In general, the use of irregular meshes gives FEM the ability to account for complex geometries, and to provide for nearly arbitrary node density variations over the computation domain. This allows extra nodes to be placed in areas where the geometry is especially complex, or high solution precision is required, while allowing for lower node density in areas with simpler geometry or lower precision requirements. The mesh can also be adaptively refined throughout the solution process, meaning that nodes are added in areas with high solution gradients. One drawback of FEM is the time-consuming construction of the mesh and solution elements, and the large computational domain required for the solutions to decay at the boundaries.

Previous researchers have used FEM to explore global induction, but have written the computational codes themselves (Everett and Schultz, 1996). Others have modified the FEM approach by formulating the numerical solutions as sums of spherical harmonics and solving the induction equations in the time domain (Velimský and Martinec, 2005). This approach is referred to as the *time-domain spectral method*, and has the advantage of operating in terms of the basis functions

that are most commonly used in theoretical studies, but has difficulty accurately reproducing fields in the vicinity of lateral conductivity contrasts such as coastlines and has increased runtimes because each spherical harmonic term is solved separately. Time-domain operation also increases runtimes because the solution for each harmonic must be calculated at a great number of time steps over at least two periods for each frequency.

The *finite-difference method* (FD) is similar to FEM, except that it employs a regular cartesian grid as a computational domain and solves the governing equations in differential form. This allows for a simpler numerical implementation, but often requires blocky conductivity models without smooth surfaces, which can be problematic for spherical problems. The drawbacks of the FEM method also apply to the FD method, with the additional difficulty that the regular meshes only allow for limited variation in node density across the solution domain, meaning that greater solution precision comes with much higher memory requirements and runtimes. Some of these drawbacks have been reduced in the global induction problem with the *staggered grid* technique, which employs radial layers of rectangular cells similar to latitude-longitude grids (Uyeshima and Schultz, 2000). Another variation is a hybrid FD/FEM scheme called *triangular finite differences*, which solves the integral induction equations on radial layers of triangular cells (Weiss, 2010). This geometry avoids the node compression at the poles that results from the staggered grid approach. Both of these techniques allow for smooth spherical surfaces and node density that is more variable than in previous FD domains, although they still place limitations on the lateral placement of conductivity variations.

Another approach to the forward problem is called the *volume integral equation method* (IE) (Kuvshinov *et al.*, 2002a), and uses Green's function techniques to derive Fredholm-integral versions of Maxwell's equations. Unlike those in FD and FEM, the system matrices are dense, but only need to be formulated for radial layers with heterogeneous conductivity, and don't require preconditioning. For models with radially symmetric conductivity and heterogeneous surface conductance, the computation space is reduced to Earth's surface, as there is no requirement for the fields to decay to zero at the boundaries. Thus accurate solutions can be pro-

duced with high lateral resolutions and short runtimes. The disadvantage of the IE method is the considerable difficulty of its computational implementation.

1.3 Outline

The FlexPDE method for performing forward-calculations for geomagnetic induction is described in Chapter 2. The method is flexible enough to allow for a great variety of forward-models with only minor modifications of a short script and has the ability to operate in both time- and frequency-domains.. A technique for including an infinitely thin surface conductance layer via a novel boundary condition is also described. Validation of the technique is presented by comparison of FlexPDE magnetic fields and response functions to analytic and semi-analytic solutions for several electromagnetic induction problems: (1) concentric spherical shells representing a layered Earth in a time-varying, uniform, external magnetic field, (2) eccentrically nested conductive spheres in the same field, and (3) homogeneous spheres or cylinders, initially at rest, then rotating at a steady rate in a constant, uniform, external field.

In Chapter 3, I describe a method for calculating c_1 estimates for the global induction problem with non-zonal source fields, and use this method to examine longitude-dependent bias in response function estimates for a number of cases at periods between 10^4 and 10^8 seconds. I compare the bias that comes from source field geometry to that from the difference between the amplitudes of Earth's response to different primary fields. The method is further developed to incorporate Earth rotation, and the local-time bias in the resulting responses is calculated and compared to empirical response functions from the literature, and to previously published calculations from a simpler method that only allows for examination of long periods.

Chapter 4 deals with a collaborative project involving several other authors of global induction forward codes, in which we have agreed to compare simulation results for six different spherical induction models. I present FlexPDE solutions for four models of spherical conductors with uniform primary fields, including

radially conductive concentric spheres with different surface conductances in (1) Northern and Southern hemispheres, and (2) Eastern and Western hemispheres, (3) eccentrically nested spheres of different conductivity, and (4) radially conductive concentric spheres with Earth-like surface conductance map. The results for the first two models are compared with those of two other researchers, and the results of the others are compared with analytic solutions for identical or illustratively similar problems.

Conclusions are stated separately in each chapter and are summarized in Chapter 5, along with a discussion of their implications with respect to future research possibilities.

References

- Backus, G., 1983: Application of mantle filter theory to the magnetic jerk of 1969. *Geophys. J. R. astr. Soc.*, **74**(3), 713–746.
- Banks, R., 1969: Geomagnetic variations and the electrical conductivity of the upper mantle. *Geophys. J. R. Astron. Soc.*, **17**(5), 457–487.
- Barlow, W., 1849: On the spontaneous electrical currents observed in the wires of the electric telegraph. *Phil. Trans. R. Soc. Lond.*, **139**, 61–72.
- Bercovici, D., and Karato, S., 2003: Whole-mantle convection and the transition-zone water filter. *Nature*, **425**(6953), 39–44.
- Chapman, S., 1919: The solar and lunar diurnal variations of terrestrial magnetism. *Phil. Trans. R. Soc. Lond., A*, **218**, 1–118.
- Chapman, S., and Bartels, J., 1940: *Geomagnetism, Vols. I and II*. Clarendon Press Oxford.
- Clement, K., 1860: *Das grosse Nordlicht in der Nacht zum 29. Aug. 1859 und die Telegraphenverwirrung in Nord-Amerika und Europa*. Hamburg.
- Constable, S., 2007: Geomagnetism. In *Treatise on Geophysics*, editor G. Schubert, 237–276. Elsevier.
- Constable, S., and Constable, C., 2004: Observing geomagnetic induction in magnetic satellite measurements and associated implications for mantle conductivity. *Geochemistry Geophysics Geosystems*, **5**(1), Q01006.
- Constable, S., and Srnka, L., 2007: An introduction to marine controlled-source electromagnetic methods for hydrocarbon exploration. *Geophysics*, **72**(2), WA3.
- Didwall, E., 1984: The electrical conductivity of the upper mantle as estimated from satellite magnetic field data. *J. Geophys. Res.*, **89**(B1), 537–542.
- Everett, M., and Schultz, A., 1996: Geomagnetic induction in a heterogenous sphere: Azimuthally symmetric test computations and the response of an undulating 660-km discontinuity. *J. Geophys. Res.*, **101**(B2), 2765–2783.

- Graham, G., 1724: An account of observations made of the variation of the horizontal needle at london, in the latter part of the year 1722, and beginning of 1723. by mr. george graham, watchmaker, frs. *Phil. Trans. Lond.*, **33**(381-391), 96.
- Kuvshinov, A., 2010: Deep electromagnetic studies from land, sea, and space: Progress status in the past 10 years. *Surv. Geophys.*, 1–41.
- Kuvshinov, A., Avdeev, D., Pankratov, O., Golyshev, S., and Olsen, N., 2002: Modelling electromagnetic fields in a 3d spherical earth using a fast integral equation approach. *Methods in Geochemistry and Geophysics*, **35**, 43–54.
- Kuvshinov, A., and Olsen, N., 2006: A global model of mantle conductivity derived from 5 years of champ, ørsted, and sac-c magnetic data. *Geophys. Res. Lett.*, **33**(18), 18301.
- Kuvshinov, A., Velìmskỳ, J., Semenov, A., Pankratov, O., Toffner-Clausen, L., Martinec, Z., Olsen, N., Sabaka, T., and Jackson, A., 2010: L2 products and performances for mantle studies with swarm. *ESA Final Report, 2010*, **173**.
- Lahiri, B., and Price, A., 1939: Electromagnetic induction in non-uniform conductors, and the determination of the conductivity of the earth from terrestrial magnetic variations. *Phil. Trans. R. Soc. Lond., A*, **237**(784), 509–540.
- Martinec, Z., and Velìmskỳ, J., 2009: The adjoint sensitivity method of global electromagnetic induction for champ magnetic data. *Geophys. J Int.*, **179**(3), 1372–1396.
- McDonald, K., 1957: Penetration of the geomagnetic secular field through a mantle with variable conductivity. *J. Geophys. Res.*, **62**(1), 117–141.
- Medin, A., Parker, R., and Constable, S., 2007: Making sound inferences from geomagnetic sounding. *Phys. Earth and Planet. Inter.*, **160**(1), 51–59.
- Myer, D., Constable, S., and Key, K., 2006: Electromagnetic exploration of the loihi seamount. In *AGU Fall Meet. Suppl.*, volume 1, 0643.
- Olsen, N., 1998: The electrical conductivity of the mantle beneath europe derived from c-responses from 3 to 720 hr. *Geophys. J Int.*, **133**(2), 298–308.
- Olsen, N., 1999: Long-period (30 days–1 year) electromagnetic sounding and the electrical conductivity of the lower mantle beneath europe. *Geophys. J Int.*, **138**(1), 179–187.
- Olsen, N., Lühr, H., Sabaka, T., Manda, M., Rother, M., Tøffner-Clausen, L., and Choi, S., 2006: Chaosa model of the earth’s magnetic field derived from champ, ørsted, and sac-c magnetic satellite data. *Geophys. J Int.*, **166**(1), 67–75.

- Olsen, N., Vennerstrøm, S., and Friis-Christensen, E., 2003: Monitoring magnetospheric contributions using ground-based and satellite magnetic data. *First CHAMP Mission Results for Gravity, Magnetic and Atmospheric Studies*, 245–250.
- Reddy, J., 1993: *An introduction to the finite element method*, volume 2. McGraw-Hill New York.
- Sabaka, T., Olsen, N., and Purucker, M., 2004: Extending comprehensive models of the earth’s magnetic field with ørsted and champ data. *Geophys. J Int.*, **159**(2), 521–547.
- Schmucker, U., 1970: *Anomalies of geomagnetic variations in the southwestern United States*, volume 13. University of California Press.
- Schmucker, U., 2003: Horizontal spatial gradient sounding and geomagnetic depth sounding in the period range of daily variation. In *Protokoll "uber das Kolloquium elektromagnetische Tiefenforschung ISSN, 0946–7467*.
- Uyeshima, M., and Schultz, A., 2000: Geoelectromagnetic induction in a heterogeneous sphere: a new three-dimensional forward solver using a conservative staggered-grid finite difference method. *Geophys. J Int.*, **140**(3), 636–650.
- Velìmskỳ, J., 2010: Electrical conductivity in the lower mantle: Constraints from champ satellite data by time-domain em induction modelling. *Physics of the Earth and Planetary Interiors*, **180**(3-4), 111–117.
- Velìmskỳ, J., and Martinec, Z., 2005: Time-domain, spherical harmonic-finite element approach to transient three-dimensional geomagnetic induction in a spherical heterogeneous earth. *Geophys. J Int.*, **161**(1), 81–101.
- Velìmskỳ, J., Martinec, Z., and Everett, M., 2006: Electrical conductivity in the earth’s mantle inferred from champ satellite measurements – 1. data processing and 1-d inversion. *Geophys. J Int.*, **166**(2), 529–542.
- Weidelt, P., 1972: The inverse problem of geomagnetic induction. *J. Geophys.*, **38**, 257–289.
- Weiss, C., 2010: Triangulated finite difference methods for global-scale electromagnetic induction simulations of whole mantle electrical heterogeneity. *Geochem. Geophys. Geosyst.*, **11**(11), Q11010.
- Weitemeyer, K., Constable, S., and Tréhu, A., 2011: A marine electromagnetic survey to detect gas hydrate at hydrate ridge, oregon. *Geophys. J Int.*

Chapter 2

Scripted Finite-element Tools for Global Electromagnetic Induction Studies

Abstract

Numerical solution of global geomagnetic induction problems in two and three spatial dimensions can be conducted with commercially available, general-purpose, scripted, finite-element software. We show that FlexPDE is capable of solving a variety of global geomagnetic induction problems. The models treated can include arbitrary electrical conductivity of the core and mantle, arbitrary spatial structure and time behavior of the primary magnetic field. A thin surface layer of laterally heterogeneous conductivity, representing the oceans and crust, may be represented by a boundary condition at the Earth-space interface. We describe a numerical test, or validation, of the program by comparing its output to analytic and semi-analytic solutions for several electromagnetic induction problems: (1) concentric spherical shells representing a layered Earth in a time-varying, uniform, external magnetic field, (2) eccentrically nested conductive spheres in the same field, and (3) homogeneous spheres or cylinders, initially at rest, then rotating at a steady rate in a constant, uniform, external field. Calculations are performed in both the time and frequency domains, and in both 2-dimensional and 3-dimensional computational meshes, with adaptive mesh refinement. Root-

mean-square accuracies of better than 1% are achieved in all cases. A unique advantage of our technique is the ability to model Earth rotation in both the time and the frequency domain, which is especially useful for simulating satellite data.

2.1 Introduction

A particularly well-suited application of large-scale numerical solutions of partial differential equations is to the problem of Geomagnetic Depth Sounding (GDS), the analysis of magnetic field data in order to estimate Earth's electrical conductivity structure. Based on magnetic field measurements from surface observatories, and the Magsat, Ørsted, and CHAMP satellites, GDS has recovered valuable information about one-dimensional electrical conductivity structure of Earth's mantle (Didwall, 1984; Olsen, 1999; Olsen, Vennerstrøm, and Friis-Christensen, 2003; Constable and Constable, 2004; Kuvshinov and Olsen, 2006; Velimský, Martinec, and Everett, 2006; Medin, Parker, and Constable, 2007), and global three-dimensional inversions are now available (Kelbert, Schultz, and Egbert, 2009). The ability to simulate electromagnetic induction, that is, to solve the equations accurately, on a global scale has important implications for GDS. Most significantly, one can investigate the effects of the many simplifying assumptions commonly used in induction analysis. One of these assumptions is that the external magnetic field is symmetric around Earth's geomagnetic or rotational axis. This has long been known to be false (Campbell, 1997), especially during the main phase of geomagnetic storms (Daglis and Kozyra, 2002), but is also relevant at longer periods (Balasis and Egbert, 2006), and this asymmetry has been shown to confound the interpretation of Earth response functions estimated from satellite data (Balasis, Egbert, and Maus, 2004). Although dayside satellite data have usually been excluded from analysis, new techniques are being developed to incorporate the dayside Sq signal in induction studies (Everett, 2010). The effects of lateral variations in mantle conductivity (Schultz and Larsen, 1987, 1990) and the irregular distribution of the oceans on 1D response functions (Fainberg and Zinger, 1981; Fainberg, Kuvshinov, and Singer, 1990; Kuvshinov, Avdeev, and Pankratov,

1999; Kuvshinov, Olsen, Avdeev, and Pankratov, 2002b; Everett, Constable, and Constable, 2003) can also be explored.

Large-scale calculations can be carried out with a commercially available, general-purpose finite-element method (FEM) software program called FlexPDE. It allows the user to design and implement detailed simulations with a scripting language, leaving the mechanics of the solution of the partial differential equations to be managed by the program. A basic script can be adapted to a more complex problem without extensive and time-consuming code modification. FlexPDE features adaptive mesh refinement (AMR), and time-domain capabilities. The latter is especially important when considerations of Earth’s rotation and the motions of satellites make working in the frequency domain less practical. Similar calculations have been carried out by other workers using other numerical techniques, such as spectral finite elements (Velínský and Martinec, 2005), staggered-grid finite-difference formulations (Uyeshima and Schultz, 2000), triangular finite differences (Weiss, 2010), volume integral equations (Kuvshinov *et al.*, 2002a). Each approach has its advantages and disadvantages. Advantages of FlexPDE include time-domain capability, field solutions everywhere in the domain, arbitrary primary field structure, relative simplicity of coding, portability to a variety of platforms, and great flexibility in modeling, especially the ability to incorporate Earth rotation in the simulations.

Our main objective here is to assess the accuracy of the general-purpose code in the context of GDS. We first provide a short derivation of the governing differential equations used in our simulations, and the implementation in FlexPDE. We then describe several examples of electromagnetic induction problems with precisely known solutions that we have also solved with FlexPDE. We examine electromagnetic induction by a spatially uniform, oscillating primary field in nested concentric spherical shells of uniform conductivity (analytic solution given in Appendix 2.5), and in eccentrically nested spheres (Martinec, 1998). The final example is that of a homogeneous sphere or cylinder, initially at rest then set rotating steadily, in a uniform, constant primary field Parker (1966). We report the accuracy of the numerical solutions, the runtimes, and the number of

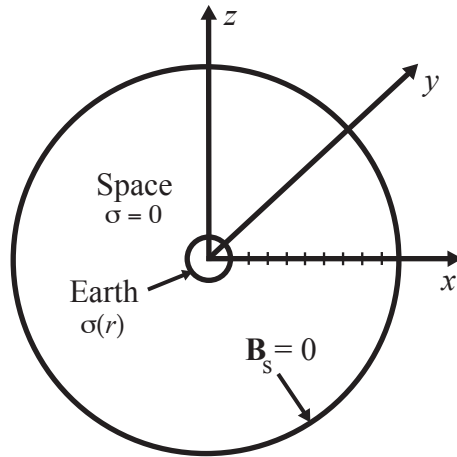


Figure 2.1: The solution domain for the global induction problem. Earth is modeled as a conductive sphere with outer radius $a = 6371$ km, while space is modeled as an infinitely resistive sphere with radius $10a$. The secondary field \mathbf{B}_s is generated by induced electrical currents in the conducting Earth, and is fully attenuated at the boundary of modeled space.

computational nodes for each example. We also discuss the analytic and simulated frequency response of the concentric spheres model, and its correspondence to empirical estimates from magnetic satellite data.

The calculations presented here are initial validations of a method we plan to apply to more complex problems. They are generally performed in a fully three-dimensional computational domain in order to provide preliminary accuracy estimates of 3D simulations. However, some global induction problems with azimuthal symmetry may be simulated in a two-dimensional computational domain. When possible, 2D simulations are preferable because the drastic reduction in the number of unknowns and solution nodes result in great gains in computational efficiency. We describe the results of our 2D simulations for the concentric shells and rotating conductor examples. FlexPDE scripts for the concentric shells example in 2D and 3D are available at <http://earthref.org/erda/1384> and <http://earthref.org/erda/1385>.

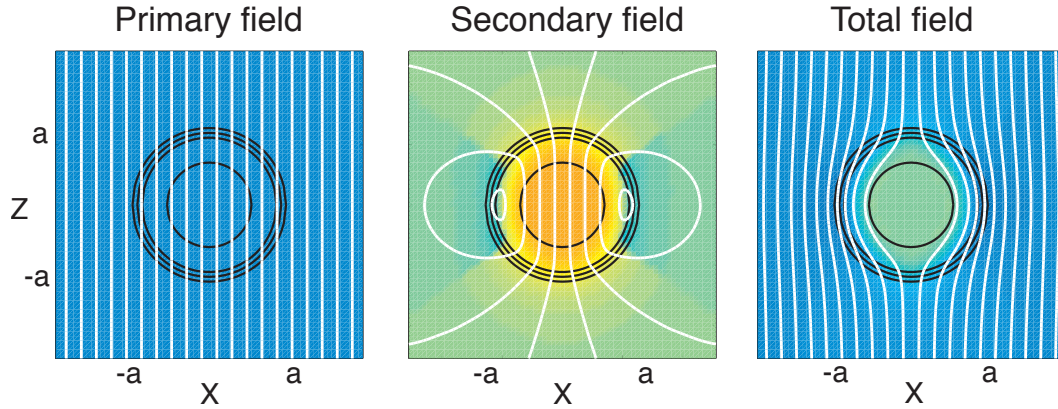


Figure 2.2: Snapshots of the primary (left), secondary (center), and total (right) magnetic induction fields for the case of a concentrically layered Earth in a uniform, z -directed primary field with a period of roughly 6.7 years. The black circles represent conductivity contrasts in Earth, including the surface, the top and bottom of the transition zone, and the core. The white curves are magnetic field lines. The colors represent the magnitude of the z -component of the field. Blue indicates an upward field, red a downward field, and green a weak or horizontal field. An animated version of this figure can be found at <http://earthref.org/erda/1137>

2.2 Forward Modeling in 2D and 3D for Geomagnetic Depth Sounding (GDS)

We introduce a 3D cartesian coordinate system with the origin at the center of Earth. The z -axis coincides with Earth's geomagnetic pole, and the plane of the x - and y -axes define the plane of the geomagnetic equator, as seen in Fig. 2.1, where Earth is modeled as a conductive sphere with radius $a = 6371$ km. The irregular finite-element mesh includes explicit interfaces at conductivity contrasts, although it is also possible to vary the conductivity within the separate regions as desired. Infinite space outside Earth is approximated as a shell of zero conductivity also centered on the origin, with radius $10a$ – large enough that the secondary field at the boundary of the model is negligible. This boundary condition is imposed by forcing the secondary potentials to vanish at the boundary. The primary magnetic field \mathbf{B}_p , is defined throughout the solution domain, including inside Earth (see Fig. 2.2), and has a P_1^0 structure with amplitude 100 nT for all simulations discussed

in this paper.

2.2.1 Governing Equations

We develop the governing equations of global geomagnetic induction in slightly different form from that used by other researchers (e.g. Everett and Schultz, 1995; Everett *et al.*, 2003; Velimskỳ and Martinec, 2005; Kuvshinov, 2008), who solve for the total induction field. Our approach is motivated by ease of implementation in FlexPDE. Specifically, it is more convenient to impose the primary field everywhere in modeled space, and solve for the secondary field. It is also useful to eliminate magnetic monopoles by using the potentials in our ultimate governing equations. (The decrease in accuracy resulting from numeric derivative calculations can be counteracted by applying FlexPDE’s error tolerance control to the resulting fields as well as the potentials.) Our approach is completely general, and is physically consistent with others in the literature, as will be demonstrated in section 2.3. Using this method, it is possible to visualize the secondary and total fields everywhere within the model, including inside Earth, which is useful for building intuition about complicated models.

The governing equations of global geomagnetic induction can be derived from the Pre-Maxwell equations (see e.g. Griffiths, 1999). According to Faraday’s Law,

$$\nabla \times \mathbf{E} = -\partial_t \mathbf{B}, \quad (2.1)$$

an electric field \mathbf{E} will be created and current ($\mathbf{J} = \sigma \mathbf{E}$, where σ is electrical conductivity) will run inside the conducting Earth in response to any changes of the magnetic field, $\partial_t \mathbf{B}$. (Note here our non-standard notation for partial derivatives.) This current will generate a secondary magnetic field \mathbf{B}_s . The shape of the secondary field will be dictated by Ampere’s Law (with displacement currents neglected as usual),

$$\nabla \times \mathbf{B}_s = \mu_0 \sigma \mathbf{E}. \quad (2.2)$$

Inside Earth, the secondary field will point in the direction opposing the time derivative of the total field $\partial_t \mathbf{B}$, while largely reinforcing this vector outside Earth.

For our purposes, the total magnetic field \mathbf{B} is simply the vector sum of the primary and secondary components. All other magnetic fields are neglected. Note that in the above discussion, Faraday's Law refers to the total magnetic field and Ampere's Law refers only to the secondary field.

In order to satisfy the law of no magnetic monopoles

$$\nabla \cdot \mathbf{B} = 0, \quad (2.3)$$

it is convenient to recast these equations in terms of the magnetic vector potential $\mathbf{A} = \mathbf{A}_p + \mathbf{A}_s$, where

$$\mathbf{B} = \nabla \times \mathbf{A}. \quad (2.4)$$

Then (2.2) becomes

$$\nabla \times \nabla \times \mathbf{A}_s = \mu_0 \sigma \mathbf{E}, \quad (2.5)$$

and (2.1) becomes

$$\nabla \times \mathbf{E} = \nabla \times -\partial_t \mathbf{A}, \quad (2.6)$$

which implies that \mathbf{E} can be written

$$\mathbf{E} = -\partial_t \mathbf{A} - \nabla V. \quad (2.7)$$

for some scalar field V . In the absence of time variation it becomes clear that V is the standard electric scalar potential, which is only non-zero in cases with externally imposed electric fields, unbalanced electric charge, or electric polarization.

We invoke the Coulomb Gauge ($\nabla \cdot \mathbf{A} = 0$) and use the vector identity

$$\nabla \times \nabla \times \mathbf{A} = \nabla(\nabla \cdot \mathbf{A}) - \nabla^2 \mathbf{A} \quad (2.8)$$

in combination with (2.5) and (2.7) to form the induction equation:

$$\nabla^2 \mathbf{A}_s = \mu_0 \sigma (\partial_t \mathbf{A} + \nabla V). \quad (2.9)$$

We also force the electric current to be solenoidal within Earth:

$$\nabla \cdot (\sigma \partial_t \mathbf{A} + \sigma \nabla V) = 0, \quad (2.10)$$

while the electric scalar potential obeys Laplace's equation in space:

$$\nabla^2 V = 0. \quad (2.11)$$

Taken together, (2.9)–(2.11) uniquely determine the magnetic fields in Earth and space when appropriate boundary conditions are specified, and \mathbf{A} is required to be continuous throughout the modeling domain (Biro and Preis, 1989). They are specified as the governing equations in the FlexPDE script. The program automatically converts them to the weak formulation and solves them.

These equations are appropriate for real-valued components in time-domain simulations. In the frequency domain, each component becomes complex, essentially doubling the number of unknowns. The time-dependence is assumed to be of the form $e^{i\omega t}$.

Modifications for 2D simulations

In simulations with azimuthal symmetry (or *limited 3D* simulations), V and A_z both vanish. Since the pathways of electric current are purely azimuthal, they are also uniformly conductive, so there is no electric polarization. Since our system is charge-neutral and has no externally imposed electric fields, we get

$$V = 0. \quad (2.12)$$

Since the current pathways are purely azimuthal, (2.7) implies that \mathbf{A} can be written

$$\mathbf{A} = A_\phi \left(\frac{-y}{\sqrt{x^2 + y^2}} \hat{\mathbf{x}} + \frac{x}{\sqrt{x^2 + y^2}} \hat{\mathbf{y}} \right), \quad (2.13)$$

for some scalar A_ϕ that is independent of longitude ϕ . Thus we can say

$$A_z = 0, \quad (2.14)$$

where we are neglecting any constant magnetic fields that do not contribute to induction.

In limited 3D simulations (2.10) becomes unnecessary, (2.9) becomes

$$\nabla^2 \mathbf{A}_s = \mu_0 \sigma \partial_t \mathbf{A}, \quad (2.15)$$

and $A_z = 0$ is imposed. This amounts to a reduction in the number of unknowns by a factor of two when performed in a full 3D computational mesh, thus decreasing the required computation time.

Limited 3D problems can also be performed on 2D computational meshes, with the z -axis representing the geomagnetic pole and the x -axis representing the geomagnetic equator. The y -axis points into the computational plane and remains unmodeled. In this case, A_x vanishes within the computational domain (although its y -derivative does not), and the only variable to be determined is A_y .

In this case operators containing derivatives in the y -direction must be modified to explicitly reflect the assumed azimuthal symmetry. Specifically, the Laplacian must be calculated

$$\nabla^2 \mathbf{A}_s = \left(\partial_{xx} A_{sy} + \partial_{zz} A_{sy} + \frac{\partial_x A_{sy}}{x} - \frac{A_{sy}}{x^2} \right) \hat{\mathbf{y}}. \quad (2.16)$$

Additionally, the curl must be modified so that (2.4) becomes

$$\mathbf{B} = -\partial_z A_y \hat{\mathbf{x}} + \left(\partial_x A_y + \frac{A_y}{x} \right) \hat{\mathbf{z}}. \quad (2.17)$$

Modeling Fine-scale Structure with Boundary Conditions

At periods less than a few days, Earth's global inductive response is influenced by the oceans and other near surface effects (Everett *et al.*, 2003). It is often useful to include a thin ocean layer atop the radial conductivity model. Modeling such an ocean by explicitly including a very thin conductive shell in the finite-element mesh would be computationally expensive and would exceed the node density limits of FlexPDE. Instead, we can impose a novel boundary condition at the interface between Earth and space that is suggested by Price (1949). The current in the ocean layer is approximated by a surface current

$$\mathbf{j} = -\hat{\mathbf{r}} \times \nabla_s \psi, \quad (2.18)$$

where $\hat{\mathbf{r}}$ is the outward-pointing radial unit vector, ∇_s is the surface-parallel component of the ∇ operator, and ψ is a scalar current function that satisfies

$$\nabla_s \cdot (\tau^{-1} \nabla_s \psi) = \partial_t B_r. \quad (2.19)$$

Here, τ is surface conductance, B_r is the radial component of the magnetic field.

The surface current will cause a discontinuity in the surface-parallel component of the magnetic field \mathbf{B}_{\parallel} that can be calculated with the integral formulation of Ampere's Law,

$$\oint \mathbf{B} \cdot d\mathbf{l} = \mu_0 I_{enc}, \quad (2.20)$$

where I_{enc} is the total current passing through a surface bounded by a closed path \mathbf{l} . Consider a rectangular amperian loop defined by \mathbf{l} , with dimensions $L \times H$ and a plane perpendicular to \mathbf{j} as seen in Fig. 2.3. If the loop is small enough that the current is effectively constant over the long side of the rectangle, then (2.20) becomes

$$\mathbf{B}_{\parallel}^+ \cdot \mathbf{l}^+ + \mathbf{B}_{\parallel}^- \cdot \mathbf{l}^- = \mu_0 j L, \quad (2.21)$$

where \mathbf{l}^+ is the upper horizontal segment of \mathbf{l} , and \mathbf{l}^- is the lower parallel segment. Since $\mathbf{l}^+ = -\mathbf{l}^- = L$, the discontinuity in the component of \mathbf{B}_{\parallel} perpendicular to the current is

$$\left(\mathbf{B}_{\parallel}^+ - \mathbf{B}_{\parallel}^- \right) \cdot \hat{\mathbf{l}}^+ = \mu_0 j, \quad (2.22)$$

where $\hat{\mathbf{l}}^+$ is the unit vector in the direction of \mathbf{l} . If we rotate the amperian loop so that its plane is parallel to the current we get $I_{enc} = 0$, so the component of \mathbf{B}_{\parallel} parallel to the current is continuous. Likewise, the surface-perpendicular component of the field is continuous because of (2.3). These results can be summarized as

$$\hat{\mathbf{r}} \times (\mathbf{B}^+ - \mathbf{B}^-) = \mu_0 \mathbf{j}. \quad (2.23)$$

To state this in terms of the vector potential, we note that (2.4) implies that \mathbf{B}_{\parallel} involves the radial derivative of the surface-parallel part of the vector potential \mathbf{A}_{\parallel} . Specifically,

$$\hat{\mathbf{r}} \times \mathbf{B} = \nabla A_r - \partial_r \mathbf{A} \quad (2.24)$$

$$= \nabla_s A_r - \partial_r \mathbf{A}_{\parallel}. \quad (2.25)$$

Plugging (2.25) into (2.23) gives the boundary condition for the Earth-space interface:

$$\partial_r \mathbf{A}^+ - \partial_r \mathbf{A}^- = -\mu_0 \mathbf{j}. \quad (2.26)$$

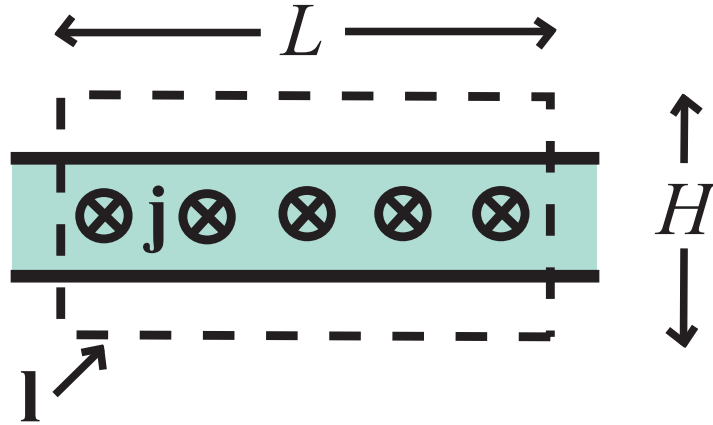


Figure 2.3: An amperian loop \mathbf{l} with length L and height H around a sheet of current \mathbf{j} , which flows into the page.

Note that both the vector potential itself and the gradient of its radial component remain continuous across the interface. The surface gradient $\nabla_s A_r$ from (2.25) cancels in (2.23), and is therefore not referenced in the imposed boundary condition. The radial derivative of A_r plays no part in the determination of \mathbf{B}_{\parallel} , thus it should not be made discontinuous. This will happen automatically since \mathbf{j} has no radial component because of (2.18), so the boundary condition given by (2.26) only affects the radial derivative of the surface-parallel part of \mathbf{A} .

Enforcing this boundary condition at the Earth-space interface incorporates the inductive effect of the oceans and continents into the solution process. In detailed Earth simulations, a conductance map like that of Everett *et al.* (2003) can be used for τ . The treatment shown here assumes that the surface is electrically isolated from the mantle, which means that vertical currents crossing from the mantle into the ocean and crust are neglected. The effect of this is a bias in \mathbf{B} magnitudes near coastlines that run perpendicular to current flow (Kuvshinov *et al.*, 1999). This bias is more pronounced at higher frequencies. It may be possible to improve our method in the future by incorporating these vertical currents into the technique, in a manner analogous to Vasseur and Weidelt (1977).

2.2.2 Implementation in FlexPDE

FlexPDE allows a choice of quadratic or cubic basis functions for its solutions (we choose a quadratic basis for all of our calculations) and employs a modified Newton-Raphson solution algorithm (see *e.g.* Reddy 2005), where the linear system solution is iterated until the estimated solution accuracy is less than the requested error tolerance. If the system iterates five times without this occurring, the solution mesh, which has triangular cells in 2D and tetrahedral cells in 3D, is adaptively refined and the linear system is regenerated and iteration begins. Thus accuracy within a model can be controlled by the user in two ways: requested error tolerance, and initial mesh density.

In all of our models, we set an error tolerance of 0.1%, which means that after five iterations the program will split any cell in which the integrated error in any variable is estimated to be greater than 0.1% relative to the variable range. The error is estimated by forming the Galerkin integral of the governing equation for each variable U over each cell, and computing a residual R . Then the variable error estimate dU in that cell is calculated from

$$dU = D^{-1}R \tag{2.27}$$

where D is the diagonal of the Jacobian matrix of derivatives of the Galerkin integral. Although our modeling variables are the magnetic vector potential and electric scalar potential, we require the program to apply this error tolerance to the resulting magnetic field components as well. This is necessary because the fields are calculated as spatial derivatives of the potentials, and are subject to additional error introduced by the numerical processes. By applying the error tolerance routine to the fields, FlexPDE will iterate until the fields are appropriately accurate despite the numerical differentiation. FlexPDE's estimates are not the true errors in the solution. We can discover the actual accuracy only in those cases where there is an analytic solution or some other procedure with guaranteed accuracy, which is of course the case for the systems considered here. Our objective in validation is to discover the true error by finding the misfit between the precise solution and that provided by FlexPDE.

We impose a similar starting mesh in each of our models, unless otherwise stated. Near the edge of modeled space, where the secondary field falls to zero and spatial resolution is not a concern, the initial mesh is coarse, with the nodes roughly 10,000 km apart. Near and inside Earth, the initial spacing decreases so that the nodes are much closer together (~ 580 km apart in a 3D model, or ~ 250 km apart in a 2D model) and are adaptively refined as needed. This mesh is near the limits of the program's initial mesh density, as implemented on our system (a 2008 MacPro with 18 GB RAM, running four simultaneous threads). It is possible to decrease the runtime of any of the calculations at the expense of a decrease in accuracy or spatial resolution. For example, the nested eccentric spheres simulation runs in 34 minutes at an error tolerance of 0.1% (for an excitation period of ~ 242 days). The runtime increases to 3.5 hours for the same simulation when the error tolerance is decreased to 0.01%.

2.2.3 Primary Field Models

In FlexPDE it is convenient to impose the primary field \mathbf{B}_p (via the associated vector potential \mathbf{A}_p , stated in cartesian coordinates) everywhere, including inside Earth. The program then solves for the secondary vector potential \mathbf{A}_s and the electric scalar potential, when applicable. A spherical harmonic representation of the primary field is easily imposed by casting the primary vector potential in terms of the complex poloidal magnetic scalar $P_p = -(p_l^m)_p Y_l^m$:

$$\mathbf{A}_p = \mathbf{r} \times \nabla P_p, \quad (2.28)$$

$$(p_l^m)_p = -a \frac{1}{(l+1)} k_l^m \left(\frac{r}{a}\right)^l, \quad (2.29)$$

where k_l^m is the external gauss coefficient of degree l and order m , r is the spherical radius (or distance to the origin placed at Earth's center) and Y_l^m are spherical harmonics (Backus *et al.*, 1996, p. 185).

To a first-order approximation, the external field from the ring current is uniform, with the form

$$\mathbf{B}_p = -k_1^0(t) \hat{\mathbf{z}}, \quad (2.30)$$

and is thus generated by the vector potential

$$\mathbf{A}_p = \frac{k_1^0(t)}{2} (y \hat{\mathbf{x}} - x \hat{\mathbf{y}}). \quad (2.31)$$

Additional components of the external field may be added to make the primary field more realistic. The most obvious example is a Y_2^1 component, representing either Sq (Kuvshinov *et al.*, 1999), or the enhanced magnitude of the external field on the nightside resulting from the non-axisymmetric component of the ring current (Balasis *et al.*, 2004).

Since electromagnetic induction is driven by time-variation of the magnetic field, Earth's rotation through an asymmetric primary field complicates the analysis of induction fields (Balasis *et al.*, 2004). Induction occurs in a reference frame that rotates within the magnetosphere along with Earth, and this rotation changes the frequency content of the primary field as seen at a particular location on Earth. However satellite measurements are collected in a reference frame that is largely stationary with respect to the magnetosphere, which leads to a discrepancy between the frequencies to which the Earth responds, and those at which the response is observed in satellite data. For this reason it can be useful to model Earth rotation in conjunction with non-axisymmetric primary field models. The results of such simulations will be discussed in Chapter 3.

Secondary Fields

FlexPDE allows for the calculation and visualization of the fields everywhere within the model domain. The magnetic fieldlines of an azimuthally symmetric system can be displayed with contour lines of the flux function $f = r_c A_\phi$, where r_c is the cylindrical radius. The primary and secondary fields can be viewed independently or superposed, which can yield additional insight into the problem. Fig. 2.2 shows a sample snapshot of the individual and superposed synthetic field magnitudes (color) and field lines (white curves). Note that time-variation in the primary field occurs everywhere in the model, including Earth's core. To counteract such changes, electric current in the core and mantle generates the secondary fields seen in the center panel, with the familiar shape of an internal dipole. The

combined field on the right demonstrates the exclusion of magnetic variations from the highly conductive core.

2.2.4 Response Functions

A common approach to global conductivity studies (Lahiri and Price, 1939; Banks, 1969) is to decompose the measured field into a sum of internal and external parts with coefficients $i_1^0(t)$ and $e_1^0(t)$ by solving for them in the equation

$$\begin{pmatrix} -\cos(\theta) & 2\left(\frac{a}{r}\right)^3 \cos(\theta) \\ \sin(\theta) & \left(\frac{a}{r}\right)^3 \sin(\theta) \end{pmatrix} \begin{pmatrix} e_1^0(t) \\ i_1^0(t) \end{pmatrix} = \begin{pmatrix} B_r(t) \\ B_\theta(t) \end{pmatrix}, \quad (2.32)$$

where θ is magnetic colatitude and r is radial distance. The frequency-domain response functions Q and c are estimated from these time-series using cross-spectral techniques. Specifically,

$$Q(\omega) = \frac{i_1^0(\omega)}{e_1^0(\omega)}, \quad (2.33)$$

and

$$c(\omega) = \frac{E_0(\omega)}{\partial_r E_0(\omega)}, \quad (2.34)$$

where E_0 is the amplitude of the electric field at Earth's surface (Weidelt, 1972). Given the assumption that $l = 1$, $m = 0$, and Earth's conductivity is radially stratified, (2.34) becomes (Constable, 1993)

$$c(\omega) = a \frac{1 - 2Q(\omega)}{2(1 + Q(\omega))}, \quad (2.35)$$

The c -response can provide information about the depth of penetration of the external field into the crust or mantle, and exact knowledge of it over all frequencies is sufficient to recover Earth's 1D conductivity structure (Bailey, 1970). Other response functions exist that can be used for models with 3D conductivity or source fields (Kuvshinov, 2010).

Synthetic data are collected from the simulations in a manner very similar to satellite measurements. For each frequency or timestep, 201 vector \mathbf{B} data points are collected along a given longitude meridian, evenly spaced from -50° to $+50^\circ$ geomagnetic latitude. Each longitude sampled in this way represents a satellite half-orbit, to be analyzed by the above methods. In contrast to most realistic

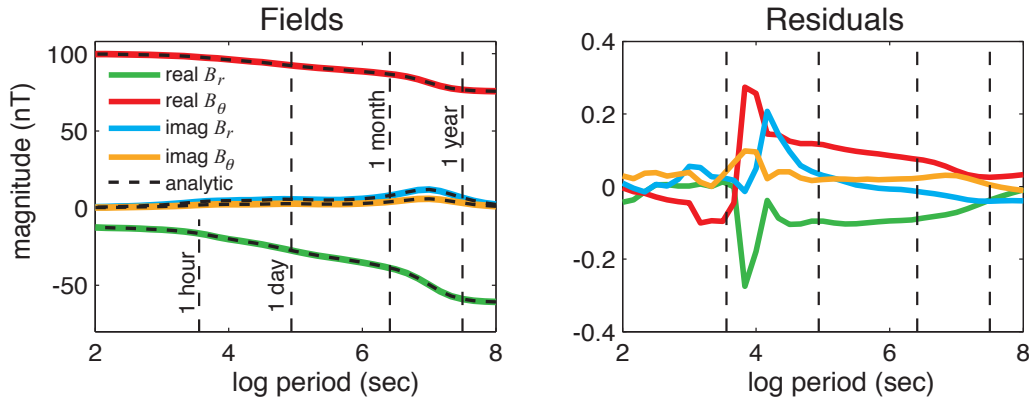


Figure 2.4: The magnetic field components and residuals relative to analytic solutions of the frequency-domain Earth model simulation measured at a single satellite observation point (400 km altitude, colatitude $\theta = 45^\circ$, longitude $\phi = 42.2^\circ$), plotted as a function of the logarithm (base 10) of the excitation period. The first panel shows the magnitudes of the modeled fields: real B_r (green), imaginary B_r (blue), real B_θ (red), and imaginary B_θ (orange), overlain by the analytic solutions (dashed black). The second panel shows the residuals for the same components. The dashed vertical lines indicate periods of 1 hour, 1 day, 1 month, and 1 year.

satellite data, synthetic data can be collected simultaneously at any number of geographic longitudes, *i.e.* at multiple local times. This means that response functions can be calculated as a function of either geographic longitude or local time. Geographic response functions are useful when the conductivity model is laterally heterogeneous. Local-time responses can be used for validating axisymmetric models, and for examining the effect of Earth’s rotation through a non-axisymmetric primary field.

2.3 Validation

2.3.1 Frequency-domain Validation

Earth Model: Concentric Homogeneous Spherical Shells

The numerical solution is validated by comparison to various classes of spherical induction problems with analytic or semi-analytic solutions. An im-

portant case is that of concentric conductive spheres in a time-varying, uniform primary field. The analytic solution for a system of conductive spheres is given in Appendix 2.5. Now, V and the radial and polar components of \mathbf{A} are known to be zero, and the governing equations are adjusted accordingly.

Figs 2.4–2.7 show comparisons of our 3D frequency-domain modeling results to the analytic solution for the case of a three-layer mantle overlying a highly conductive core. The conductivity of each layer is listed in Table 2.1, and is motivated by bounds determined by Medin *et al.* (2007). The response of this model to uniform external fields was studied at periods from several minutes to 3 years.

In actual satellite mantle conductivity studies, the short-period range of the c -response is limited by the orbital period of the satellite, which is generally 60–120 minutes, giving a Nyquist period of roughly 10^4 seconds. The long-period range in such studies is limited by the length of available time-series and the possibility of contamination of the induction signal by the secular variation of Earth’s main field, which could manifest itself as reduced correlation between the internal and external fields. For these reasons, current studies rarely explore periods much longer than 100 days.

Simulations were run sequentially from long period to short, with the computation mesh being retained from one period to the next, to reduce the time required for mesh generation. This means that each model retained the extra nodes resulting from adaptive refinement from previous runs. The initial 3D mesh contained 121,866 nodes, while the final mesh contained 1,895,969 nodes. The longer periods required shorter runtimes than the short periods; the period with the shortest runtime was under 5 minutes, while the longest runtime was just under four hours.

Being azimuthally symmetric, this model is also amenable to solution in a 2D mesh, which was carried out in a manner similar to the 3D models, but with far fewer nodes (initial mesh: 11,713 nodes, final mesh: 90,787 nodes) and faster runtimes (shortest runtime: less than 30 seconds, longest runtime: less than 11 minutes).

Table 2.1: Electrical conductivities used in Earth model simulations. Mantle values are motivated by Medin *et al.* (2007).

Region	Depth (km)	σ (S/m)
Upper mantle	0–400	0.01
Transition zone	400–800	0.1
Lower mantle	800–2871	1.0
Core	2871–6371	5×10^5

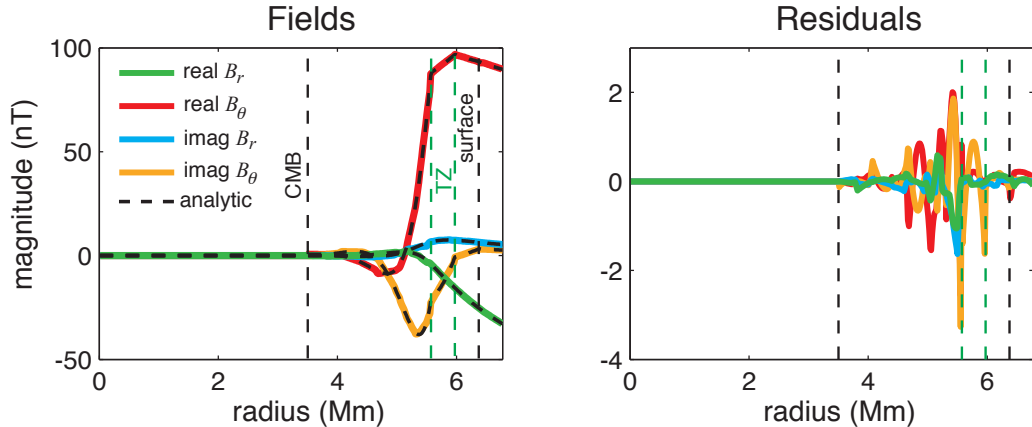


Figure 2.5: The magnetic field components and residuals of the frequency-domain Earth model simulation vs. radius at constant colatitude ($\theta = 45^\circ$) and longitude ($\phi = 42.2^\circ$) for excitation period $T = 4.64 \times 10^5$ seconds, or about 5.4 days. The dashed vertical lines indicate σ contrasts at the boundaries of the spherical shells representing the core and layered mantle.

In Fig. 2.4, the real and imaginary parts of the radial and polar components of the 3D model’s magnetic field are plotted vs. period at a single satellite measurement location. Also shown are the residuals (analytic solution minus FlexPDE solution). The results show excellent agreement, with an rms error less than 0.1 nT for each component, and a maximum error in any component of less than 0.3 nT. In the corresponding 2D model the errors are slightly higher: the rms error is less than 1 nT for each component, while the maximum error is less than 2 nT. The 2D errors are similar in value to those found in 3D models with the error tolerance (see section 2.2.2) increased from 0.1% to 1%. If necessary, the errors can be made smaller by imposing a smaller error tolerance at the expense of longer runtimes.

Fig. 2.5 shows the components and residuals at the same colatitude and

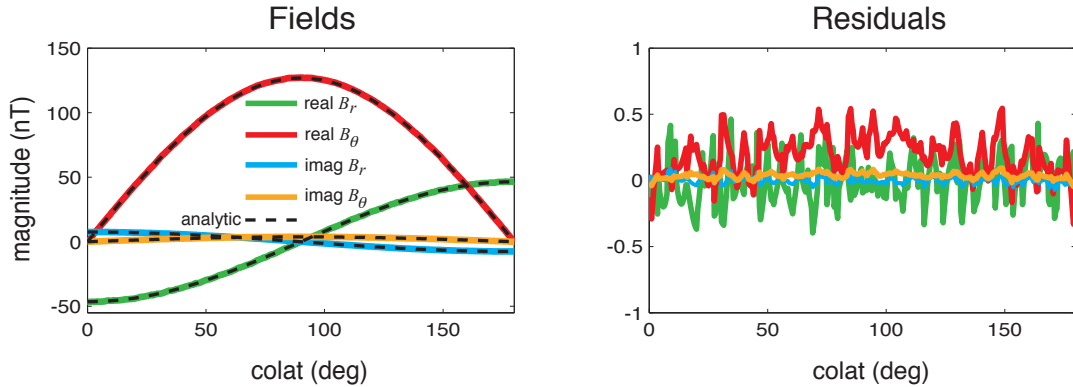


Figure 2.6: The magnetic field components and residuals of the frequency-domain Earth model simulation vs. colatitude at satellite altitude (400 km) and constant longitude ($\phi = 42.2^\circ$) for $T = 4.64 \times 10^5$ seconds.

longitude as the previous figure as a function of radius, for a single period ($T = 4.64 \times 10^5$ seconds). The boundaries of the homogeneous conductive shells are also shown. The results are quite good, with a rms misfit less than 0.4 nT along the track for all components. The residual of the polar component reaches 3.3 nT at a point within the mantle, near the conductivity contrast at 800 km. This is probably due to the discretization of the mesh, and the misfit is seen to increase at conductivity interfaces. The error remains much lower outside of Earth, where empirical measurements can actually be performed. Similar results are found along radial tracks of other colatitudes, and at other frequencies. The corresponding rms misfit along the track in the 2D model is less than 2 nT, while the maximum error is less than 8 nT.

The same components and residuals are shown in Fig. 2.6 along a satellite half-orbit (all latitudes along a single longitude at an altitude of 400 km) at the same period as in Fig. 2.5. The simulation results again show good agreement with the analytic solution, with an rms misfit in all field components of less than 0.3 nT, and a maximum residual of less than 0.6 nT. Similar results are found at all frequencies. The corresponding rms misfit in the 2D simulation is just over 0.1 nT and the maximum residual is less than 0.2 nT.

Synthetic c -responses estimated from frequency-domain simulations are shown in Fig. 2.7. The residuals for these responses have an rms value of 1.9 km for the

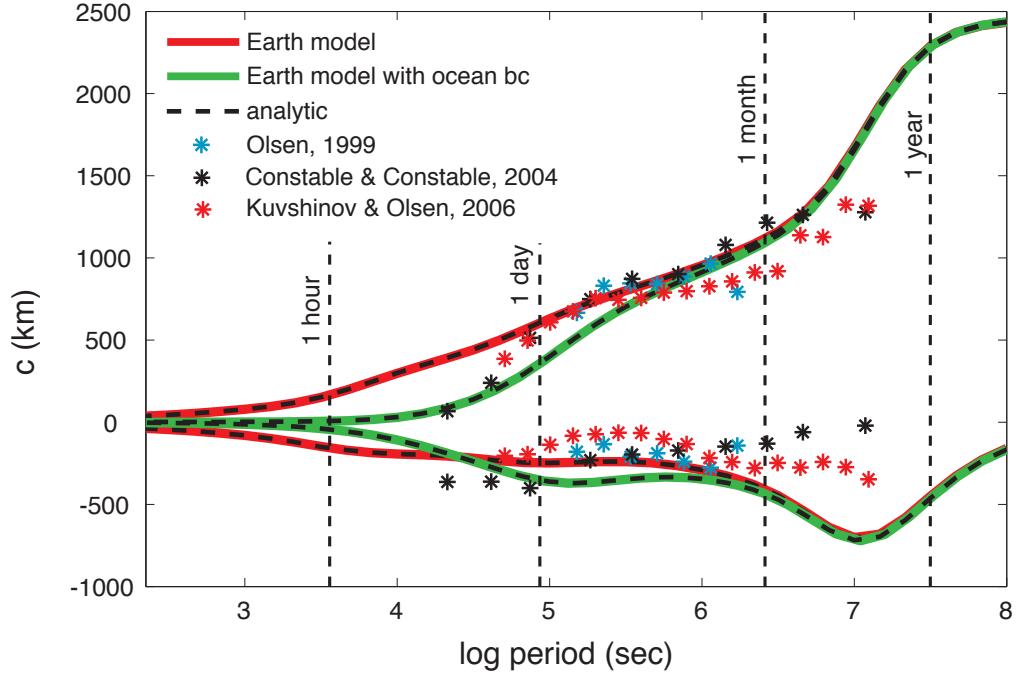


Figure 2.7: The synthetic c -response calculated from the frequency-domain Earth model simulations. The red lines are the real (positive) and imaginary (negative) parts of c for the Earth model, with conductivity described in Table 2.1. The green lines indicate the response of the same model overlain by a global 3 km ocean. The dashed black curves overlying the red and green curves indicate the analytic solutions for both of these models. Also indicated are empirical estimates of the Earth's c -response, derived from satellite magnetic measurements.

real part and 0.7 km for the imaginary part, with a maximum value of 3.1 km for all excitation periods. Also shown is the response of the same conductivity model overlain by a global surface ocean of conductance $\tau = 9000$ S, along with the analytic solution. The ocean was included via the boundary condition (2.26) and solved in 3D simulations. Two dimensional simulations with this boundary condition yielded similar results, but with slightly smaller residuals.

The inclusion of the global ocean allows induced electric current to run in the conductive seawater, which decreases the amplitude of the magnetic fields at the seafloor, and thus reduces the depth of penetration of the fields into the mantle. This penetration depth is the physical interpretation of the real part of c , which explains its reduction at periods less than ten days. A similar effect occurs in the imaginary part of c , but the physical interpretation of this quantity is less intuitive. At longer periods, the skin depth in seawater is large enough to allow the fields to pass through the ocean largely unimpeded, which results in the c -responses at these periods being insensitive to the presence of the ocean.

3D Conductivity Model: Eccentrically Nested Spheres

To validate the technique with fully 3D geometry, we simulated induction in a 6371 km conductive sphere ($\sigma = 1$ S/m) with an off-axis spherical inclusion ($\sigma = 10$ S/m) with radius 3500 km centered at radius $r = 2700$ km, colatitude $\theta = 40^\circ$, and longitude $\phi = 35^\circ$ for $T = 2.094 \times 10^7$ seconds. This conductivity model is fully 3D and has twice the number of unknowns of an analogous limited 3D model. However, this model contains only one conductive inclusion inside Earth and has a relatively long period. At an error tolerance of 0.1%, the simulation required only 109,021 nodes – fewer than the multiple-frequency Earth model calculation described above, and requiring no AMR – and the runtime was 33 minutes. This produced fields with errors of roughly 0.1 nT outside Earth, but that reached 1.2 nT inside Earth. In order to reduce these errors to less than 0.6 nT everywhere, we reduced the error tolerance to 0.01%. This more accurate simulation did require AMR, ending up with 231,677 nodes and a runtime of 3.5 hours.

The results are compared to the analytic solution of Martinec (1998) in Fig.

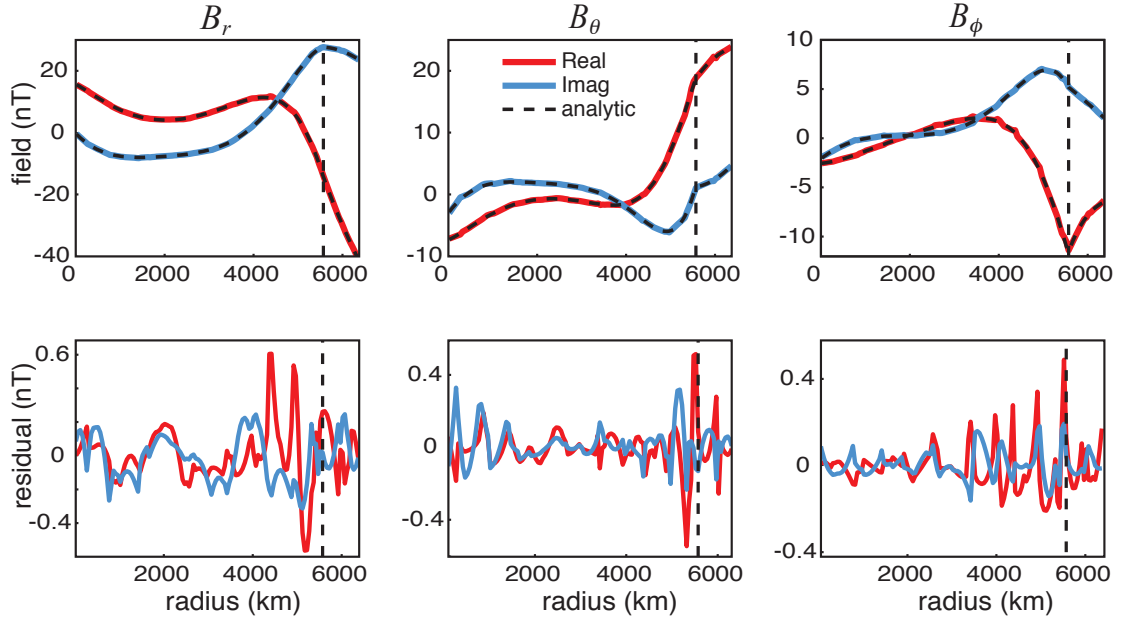


Figure 2.8: The magnetic field components and residuals of the eccentricly nested spheres simulation at constant colatitude ($\theta = 13^\circ$) and longitude ($\phi = 0^\circ$) as a function of radius, for $T = 2.094 \times 10^7$ seconds (or about 242 days). The top panels show the real (solid red line) and imaginary (solid blue line) magnitudes of the \mathbf{B} -field components, overlain by the analytic solutions (dashed black lines). The bottom panels show the residuals with respect to the analytic solution (Martinec, 1998). The left panels refer to B_r , the middle to B_θ , and the right to B_ϕ . The vertical dashed line indicates the location of the boundary between the inner and outer spheres along the radial measurement profile.

2.8, which shows the value of the simulated components of the magnetic field, the analytic solution, and the residuals as a function of radius. The rms of the residual in this measurement is less than 0.2 nT for all components.

2.3.2 Time-domain Validation

Rotating Conductor in a Uniform Field

To test the accuracy of the time-stepping capability of FlexPDE, the case of a rotating homogeneous 6371 km sphere in a 100 nT uniform y -directed magnetic field was modeled in the time domain. The analytic solution for this case is given by Parker (1966). In this problem, the conducting sphere (surrounded by vacuum) is initially at rest and permeated by the magnetic field. At time $t = 0$, the sphere begins to rotate around the z -axis at constant angular speed $\omega = 1.96 \times 10^{-6}$ rad/s, corresponding to a rotational period of 37.1 days. The behavior of the system is dependent on the magnetic Reynolds number $R_m = \mu_0 \omega \sigma a^2 = 100$. The simulation is carried out in the rotating coordinate system of the sphere, 50 time steps for each complete rotation. The initial node spacing inside the conductor was roughly 580 km, giving a total 102,993 nodes in the full model, while the final mesh had 103,023 nodes. The complete 100 step calculation ran in approximately 1 hour and 12 minutes.

Fig. 2.9 shows a snapshot of the magnitude of the numerical solution (top) and its residual (bottom) after 100 time steps on a cross-sectional plane at the equator. The figure also shows time-series of the field components at two points inside and two points outside the conductor. The residuals in the field components remain below 3 nT within the solution domain, with an rms value of 1 nT. The largest residuals once again occur within the conductor adjacent to the interface.

Since solution accuracy can be partially controlled in FlexPDE via the node-density of the solution mesh, we also performed this simulation with an initial node spacing within the conductor of roughly 710, 910, 1300, and 2100 km. We show in Fig. 2.10 the rms error within the area of interest as a function of 3D node spacing for simulations with $R_m = 100$ and $R_m = 3213.4$.

This spherical induction problem is not axisymmetric, and is not amenable

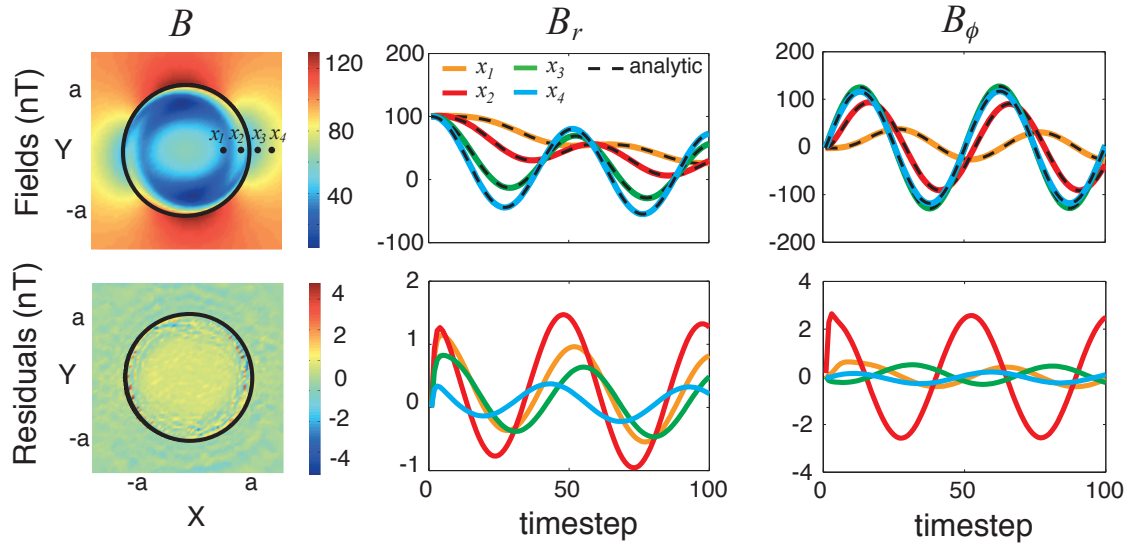


Figure 2.9: Snapshot of the magnetic field magnitude and residuals on the x - y plane for the time-domain simulation of a rotating ($T = 37.1$ days) conductive sphere in a constant, uniform external field. The top left panel shows the B-field magnitude in nT at time $t = 74.2$ days, as calculated by FlexPDE after 100 timesteps. The top middle and right panels show time-series of the B_r and B_ϕ calculated on the x -axis of the rotating frame at $x_1 = 4718$ km (orange), $x_2 = 5927$ km (red), $x_3 = 7137$ km (green), and $x_4 = 8347$ km (light blue). Each of the bottom panels indicates the measured misfit for the panels directly above. An animated version of this figure can be found at <http://earthref.org/erda/1136>

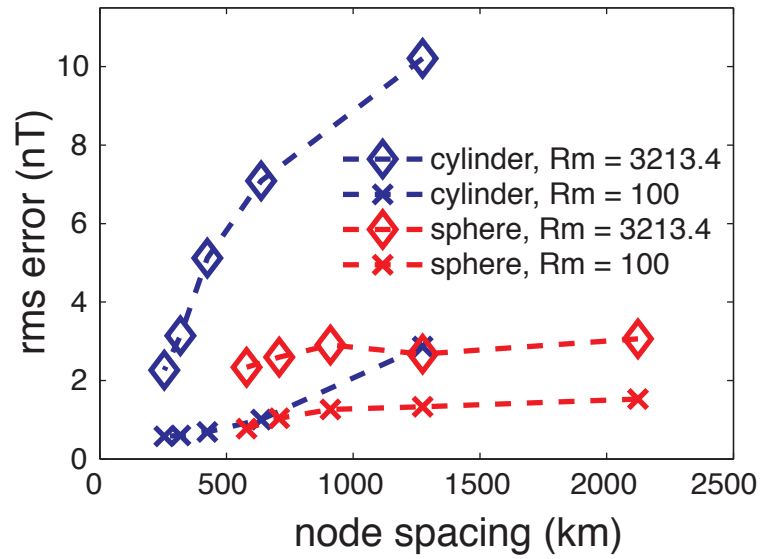


Figure 2.10: The rms residual field magnitude in the 100th timestep of the rotating conductor simulations plotted as a function of the node spacing of the computational mesh inside the conductor. The blue symbols refer to 2D simulations of infinitely long cylinders; the red symbols refer to 3D simulations of conductive spheres. The conductivity in each case is $\sigma = 1$ S/m, and the radius of the conductors is 6371 km. The diamonds indicate a rotational period of 1.15 days (magnetic Reynolds number $R_m = 3213.4$); the x's indicate a rotational period of 37.1 days ($R_m = 100$).

to 2D simulation. However, running such a problem with the magnetic field lying always in the plane of the 2D computation mesh is physically identical to the rotation of an infinitely long conductive cylinder within a uniform field orthogonal to the cylinder axis, as long as the assumption of axisymmetry is not applied to the calculation of spatial derivatives (*i.e.* (2.16) and (2.17) are replaced with the standard 2D Laplacian and curl) . This problem also has an analytic solution (Parker, 1966). We performed such a 100-step time-domain simulation with a primary field magnitude and conductivity identical to the 3D spherical case, with initial node spacings within the sphere of 250, 320, 429, 640, and 1300 km. The rms misfit in the 250 km case was 0.6 nT, and the maximum residual was 1.4 nT. Fig. 2.10 shows the rms misfit as a function of 2D node spacing.

Time-stepping Earth Model

The concentric spherical shells Earth model from section 3.1.1 can also be validated for any given period in the time domain, by imposing a time-varying primary field of constant period. When this was performed for a number of periods in 2D and 3D with eight timesteps per cycle, it was found that the results were similar in accuracy to the frequency-domain validations discussed above. In all cases, it was necessary to allow a single initial cycle to pass in order for transient effects to be minimized as the system reached steady-state. This implies that synthetic data should be trimmed appropriately prior to analysis in future time-domain simulations, and extends the runtime of time-domain simulations used for long-period, deep mantle conductivity studies. It should be noted that time-domain simulations of global geomagnetic induction based on realistic primary field magnitudes may require shorter timesteps than those implied in these validations in order to accommodate the high-frequency content and sudden magnetic storms found in the realistic primary field.

2.4 Conclusions

We successfully validated a 2D and 3D simulation technique for the global geomagnetic induction problem. The technique allows for nearly arbitrary conductivity and primary field structures, and is easily adapted for Earth rotation. A laterally-varying surface conductance can be imposed via a boundary condition at the Earth-Space interface.

The synthetic fields show good agreement with analytic solutions for electromagnetic induction in concentric spheres, eccentrically nested spheres, and rotating uniform conductors. The absolute error of the FlexPDE solution is dependent on the conductivity values, geometry, and excitation period of the system being simulated, as well as on node spacing and the location of the measurement, with higher errors in areas of nonzero conductivity. Acceptable errors (a few nT inside Earth and less than 1 nT in space) are attainable on our system. The associated error in global c -response estimates is roughly 1-2 km. The rms errors of the region including Earth and 2000 km of surrounding space are generally of the order of the error tolerance set by the user.

We have shown FlexPDE to be a highly effective tool for solving a wide variety of the geophysical problems in electromagnetic induction. The capability to produce time- and frequency-domain solutions of induction in a rotating Earth in within a variety of non-axisymmetric primary fields is especially scientifically valuable. Such solutions will be discussed in a forthcoming paper.

2.5 Appendix: Analytic Solution for Earth Model in Uniform Primary Field

We study induction in a spherically layered body, excited by a single spherical harmonic source field, degree l . We extend the treatment in Chapter 5 of Backus *et al.* (1996), henceforth BPC. Everything is time periodic with radian frequency ω . The external magnetic field is harmonic; we take the source field to be uniform and axial for simplicity, *i.e.* $l = 1, m = 0$. Then the magnetic scalar

potential is Ω with

$$\Omega = a \left[k \left(\frac{r}{a} \right) + g \left(\frac{a}{r} \right)^2 \right] \cos \theta, r \geq a \quad (2.36)$$

where k is the amplitude of the uniform driving field and $g = g_1^0$ is the Gauss coefficient of the induced axial dipole. According to BPC page 198, if

$$Q(\omega) = \frac{g(\omega)}{k(\omega)} \quad (2.37)$$

then

$$\frac{\partial_r p}{p(r)} = -\frac{1}{a} \frac{4Q(\omega) + 1}{2Q(\omega) - 1}, \quad (2.38)$$

where $p = p_1^0$.

The scalar obeys the ordinary differential equation BPC (5.4.20) which, when $l = 1$ and $m = 0$ becomes

$$\partial_r^2 p + \frac{2}{r} \partial_r p - \left(\frac{2}{r^2} + i\omega\mu_0\sigma(r) \right) p = 0. \quad (2.39)$$

Let the sphere be divided into N concentric shells with radii $0 < r_1 < r_2 \cdots < r_N = a$ and corresponding conductivities σ_n . Let the poloidal scalar in the n^{th} shell be $p_n(r)$. Then the solution to (2.39) is the combination of spherical Bessel functions

$$p_n(r) = \begin{cases} A_n j_1(k_n r), & n = 1 \\ A_n h_1^{(1)}(k_n r) + B_n h_1^{(2)}(k_n r), & n > 1 \end{cases} \quad (2.40)$$

where $k_n = (1 - i)\sqrt{\omega\mu_0\sigma_n/2}$ and the Bessel functions are explicitly

$$h_1^{(1)}(z) = -\frac{e^{iz}}{z} \left(1 + \frac{i}{z} \right); \quad h_1^{(2)}(z) = -\frac{e^{-iz}}{z} \left(1 - \frac{i}{z} \right) \quad (2.41)$$

$$j_1(z) = \frac{h_1^{(1)}(z) + h_1^{(2)}(z)}{2} = \frac{\sin z}{z^2} - \frac{\cos z}{z} \quad (2.42)$$

and $j_1(0) = 0$. Because of the complex form of k , $|h_1^{(1)}(kr)|$ decreases exponentially with increasing r , while $|h_1^{(2)}(kr)|$ grows with increasing r . In fact for high frequencies, $h_1^{(1)}$ may be utterly negligible compared with $h_1^{(2)}$ almost everywhere. We can in principle discover the coefficients A_n and B_n from the fact that p_n and $\partial_r p_n$ are continuous at r_n . The absolute size of the solution will vary over an

enormous range if the frequency is large, and will cause numerical problems with a straightforward evaluation. One answer to this difficulty is to start the solution for p several skin depths below the surface, not at $r = 0$ and use an artificial boundary condition $p = 0$ there.

Another approach is to follow the quantity on the left of (2.38) from the bottom to the surface; this ratio never becomes excessively large or small since it is the derivative of the log of p . Then we can work backwards from (3). We illustrate. Let $C_n = a\partial_r p(r_n)/p(r_n)$. Within the n^{th} shell, when $n > 1$

$$C_n = a \frac{A_n d_1 + B_n d_2}{A_n h_1 + B_n h_2} \quad (2.43)$$

$$C_{n-1} = a \frac{A_n d_1^- + B_n d_2^-}{A_n h_1^- + B_n h_2^-} \quad (2.44)$$

where we reduce notational clutter with these abbreviations:

$$h_j = h_1^j(k_n r_n); \quad h_j^- = h_1^j(k_n r_{n-1}); \quad (2.45)$$

$$d_j = \partial_r h_1^j(k_n r_n); \quad d_j^- = \partial_r h_1^j(k_n r_{n-1}). \quad (2.46)$$

Rearranging (2.43) we have

$$\frac{A_n}{B_n} = - \left(\frac{C_n h_2 - b d_2}{C_n h_1 - b d_1} \right). \quad (2.47)$$

And of course (2.44) is just

$$C_{n-1} = a \frac{d_1^-(A_n/B_n) + d_2^-}{h_1^-(A_n/B_n) + h_2^-}. \quad (2.48)$$

Substituting (2.47) into (2.48) gives

$$C_n = a \frac{C_{n-1}(d_2 h_1^- - d_1 h_2^-) + a(d_1 d_2^- - d_2 d_1^-)}{C_{n-1}(h_2 h_1^- - h_1 h_2^-) + a(h_1 d_2^- - h_2 d_1^-)}. \quad (2.49)$$

This expression allows us to move up through the shells to the top, provided we can evaluate C_1 . This is easy from (2.40):

$$C_1 = \frac{a \partial_r j_1(k_1 r_1)}{j_1(k_1 r_1)}. \quad (2.50)$$

Notice that in (2.49) each factor involving the very small $h_1^{(1)}$ is always multiplied by $h_1^{(2)}$ (or its derivative) which is almost its reciprocal, thus keeping the product

of the two fairly near unity no matter how large or small the individual factors themselves may become. To take advantage of this fact, symbolic manipulation of (2.41) and (2.42) may be required in order to convert (2.49) and (2.50) into a form that avoids numerical overflow or underflow. Finally,

$$c(\omega) = \frac{a}{1 + C_N}. \quad (2.51)$$

If the magnetic fields are needed in addition to the c -response, then knowledge of C_n throughout the system, can be converted to knowledge of A_n/B_n through (2.47) although this value may become very large. From continuity of p and (2.40) with $n > 1$

$$A_n h_1^- + B_n h_2^- = A_{n-1} h_1^{--} + B_{n-1} h_2^{--} \quad (2.52)$$

where $h_j^{--} = h_1^j(k_{n-1}r_{n-1})$. Thus

$$A_n \left(h_1^- + \frac{h_2^-}{A_n/B_n} \right) = A_{n-1} \left(h_1^{--} + \frac{h_2^{--}}{A_{n-1}/B_{n-1}} \right), \quad (2.53)$$

so A_n can be transferred from one level to the next. The overall scaling comes from BPC (5.3.15) which implies that

$$p(r_N) = a(g - k/2). \quad (2.54)$$

2.6 Acknowledgments

This work was supported by NASA Headquarters under the NASA Earth and Space Science Fellowship Program - Grant NNX07AQ94H. The authors would also like to thank Steven Constable, Alexei Kuvshinov, and Mark Everett for useful discussions, Mark Everett and Zdeněk Martinec for providing computer code for calculating analytic solutions, and two anonymous reviewers for helpful suggestions that improved this manuscript.

Chapter 2, in full, has been submitted for publication to Geophysical Journal International as: Ribaudo, J.T., Constable, C.G., & Parker, R.L., Scripted nite element tools for global electromagnetic induction studies . The dissertation author was the primary investigator and author of this paper.

References

- Backus, G., Parker, R., and Constable, C., 1996: *Foundations of Geomagnetism*. Cambridge Univ Pr.
- Bailey, R., 1970: Inversion of the geomagnetic induction problem. *Proc. Roy. Soc., A*, **315**(1521), 185–194.
- Balasis, G., and Egbert, G., 2006: Empirical orthogonal function analysis of magnetic observatory data: Further evidence for non-axisymmetric magnetospheric sources for satellite induction studies. *Geophys. Res. Lett.*, **33**(11), 11311.
- Balasis, G., Egbert, G., and Maus, S., 2004: Local time effects in satellite estimates of electromagnetic induction transfer functions. *Geophys. Res. Lett.*, **31**, 16610.
- Banks, R., 1969: Geomagnetic variations and the electrical conductivity of the upper mantle. *Geophys. J. R. Astron. Soc.*, **17**(5), 457–487.
- Biro, O., and Preis, K., 1989: On the use of the magnetic vector potential in the finite-element analysis of three-dimensional eddy currents. *IEEE Trans. Magn.*, **25**(4), 3145–3159.
- Campbell, W., 1997: *Introduction to geomagnetic fields*. Cambridge Univ Pr.
- Constable, S., 1993: Constraints on mantle electrical conductivity from field and laboratory measurements. *J. Geomagn. Geoelectr.*, **45**(9), 7070–728.
- Constable, S., and Constable, C., 2004: Observing geomagnetic induction in magnetic satellite measurements and associated implications for mantle conductivity. *Geochemistry Geophysics Geosystems*, **5**(1), Q01006.
- Daglis, I., and Kozyra, J., 2002: Outstanding issues of ring current dynamics. *J. Atmos. Sol. Terr. Phys.*, **64**(2), 253–264.
- Didwall, E., 1984: The electrical conductivity of the upper mantle as estimated from satellite magnetic field data. *J. Geophys. Res.*, **89**(B1), 537–542.

- Everett, M., 2010: Spatiotemporal sampling of sq+-induced geomagnetic responses at leo satellite altitude for a radially conductive earth. *Geophys. J Int.*, **183**(3), 1185–1198.
- Everett, M., Constable, S., and Constable, C., 2003: Effects of near-surface conductance on global satellite induction responses. *Geophys. J Int.*, **153**(1), 277–286.
- Everett, M., and Schultz, A., 1995: Geomagnetic induction in eccentrically nested spheres. *Phys. Earth Planet. Int.*, **92**(3-4), 189–198.
- Fainberg, E., Kuvshinov, A., and Singer, B., 1990: Electromagnetic induction in a spherical earth with non-uniform oceans and continents in electric contact with the underlying medium i. theory, method and example. *Geophys. J Int.*, **102**(2), 273–281.
- Fainberg, E., and Zinger, B., 1981: Electromagnetic induction in a spherical model of the earth with a real distribution of near-surface conductivity. *Phys. Earth Planet. Int.*, **25**(1), 52–56.
- Griffiths, D., 1999: *Introduction to electrodynamics*, volume 3. prentice Hall New Jersey;.
- Kelbert, A., Schultz, A., and Egbert, G., 2009: Global electromagnetic induction constraints on transition-zone water content variations. *Nature*, **460**(7258), 1003–1006.
- Kuvshinov, A., 2008: 3-d global induction in the oceans and solid earth: recent progress in modeling magnetic and electric fields from sources of magnetospheric, ionospheric and oceanic origin. *Surv. Geophys.*, **29**(2), 139–186.
- Kuvshinov, A., 2010: Deep electromagnetic studies from land, sea, and space: Progress status in the past 10 years. *Surv. Geophys.*, 1–41.
- Kuvshinov, A., Avdeev, D., and Pankratov, O., 1999: Global induction by sq and dst sources in the presence of oceans: bimodal solutions for non-uniform spherical surface shells above radially symmetric earth models in comparison to observations. *Geophys. J Int.*, **137**(3), 630–650.
- Kuvshinov, A., Avdeev, D., Pankratov, O., Golyshev, S., and Olsen, N., 2002a: Modelling electromagnetic fields in a 3d spherical earth using a fast integral equation approach. *Methods in Geochemistry and Geophysics*, **35**, 43–54.
- Kuvshinov, A., and Olsen, N., 2006: A global model of mantle conductivity derived from 5 years of champ, ørsted, and sac-c magnetic data. *Geophys. Res. Lett.*, **33**(18), 18301.

- Kuvshinov, A., Olsen, N., Avdeev, D., and Pankratov, O., 2002b: Electromagnetic induction in the oceans and the anomalous behaviour of coastal c-responses for periods up to 20 days. *Geophys. Res. Lett.*, **29**(12), 14409.
- Lahiri, B., and Price, A., 1939: Electromagnetic induction in non-uniform conductors, and the determination of the conductivity of the earth from terrestrial magnetic variations. *Phil. Trans. R. Soc. Lond., A*, **237**(784), 509–540.
- Martinec, Z., 1998: Geomagnetic induction in multiple eccentrically nested spheres. *Geophys. J Int.*, **132**(1), 96–110.
- Medin, A., Parker, R., and Constable, S., 2007: Making sound inferences from geomagnetic sounding. *Phys. Earth and Planet. Inter.*, **160**(1), 51–59.
- Olsen, N., 1999: Induction studies with satellite data. *Surv. Geophys.*, **20**(3), 309–340.
- Olsen, N., Vennerstrøm, S., and Friis-Christensen, E., 2003: Monitoring magnetospheric contributions using ground-based and satellite magnetic data. *First CHAMP Mission Results for Gravity, Magnetic and Atmospheric Studies*, 245–250.
- Parker, R., 1966: Reconnexion of lines of force in rotating spheres and cylinders. *Proc. Roy. Soc., A*, **291**(1424), 60–72.
- Price, A., 1949: The induction of electric currents in non-uniform thin sheets and shells. *The Quarterly Journal of Mechanics and Applied Mathematics*, **2**(3), 283–310.
- Schultz, A., and Larsen, J., 1987: On the electrical conductivity of the mid-mantle: I. calculation of equivalent scalar magnetotelluric response functions. *Geophys. J. R. Astr. Soc.*, **88**(3), 733–761.
- Schultz, A., and Larsen, J., 1990: On the electrical conductivity of the mid-mantle: II. delineation of heterogeneity by application of extremal inverse solutions. *Geophys. J Int.*, **101**(3), 565–580.
- Uyeshima, M., and Schultz, A., 2000: Geoelectromagnetic induction in a heterogeneous sphere: a new three-dimensional forward solver using a conservative staggered-grid finite difference method. *Geophys. J Int.*, **140**(3), 636–650.
- Vasseur, G., and Weidelt, P., 1977: Bimodal electromagnetic induction in non-uniform thin sheets with an application to the northern pyrenean induction anomaly. *Geophys. J. R. Astr. Soc.*, **51**(3), 669–690.
- Velimský, J., and Martinec, Z., 2005: Time-domain, spherical harmonic-finite element approach to transient three-dimensional geomagnetic induction in a spherical heterogeneous earth. *Geophys. J Int.*, **161**(1), 81–101.

- Velínský, J., Martinec, Z., and Everett, M., 2006: Electrical conductivity in the earth's mantle inferred from champ satellite measurements – 1. data processing and 1-d inversion. *Geophys. J Int.*, **166**(2), 529–542.
- Weidelt, P., 1972: The inverse problem of geomagnetic induction. *J. Geophys.*, **38**, 257–289.
- Weiss, C., 2010: Triangulated finite difference methods for global-scale electromagnetic induction simulations of whole mantle electrical heterogeneity. *Geochem. Geophys. Geosyst.*, **11**(11), Q11010.

Chapter 3

The effect of on global response function estimates of Earth's rotation through an asymmetric source field

Abstract

A method for calculating response function estimates for the global induction problem with asymmetric source fields is described and used to examine spatial bias in response function estimates for a number of cases, including uniform primary fields contaminated with asymmetric quadrupole structure and uniformly-directed primary fields with spatially variable amplitude. The resulting longitude- and local-time-dependent effect on Weidelt's c -response is analyzed for periods between 10^4 and 10^8 seconds. The biasing effects from source field geometry and from the different amplitude of Earth's response to different primary field structures are compared, and it is found that the geometric effect dominates. The method is further developed to incorporate Earth rotation, and the local-time bias in the resulting responses is calculated and compared to empirical response functions from the literature. It is found that quadrupole contamination of predominantly uniform primary fields is more likely to explain the observed bias than uniformly-directed

primary fields with longitude-weighted amplitude. The synthetic responses are compared to previously published calculations for periods of 5 and 10 days. With only minor modification, the described method can be extended to rotating-Earth models with nearly arbitrary primary field structure.

3.1 Introduction

Since 1889 ground-based observations of magnetic fields have been used to explore the 1D electrical conductivity of Earth’s mantle (Chapman, 1919), and a worldwide network of observatories was eventually built that produces data for geomagnetic depth sounding (GDS) techniques (Lahiri and Price, 1939; Banks, 1969). However the spatial distribution of observatories is sparse, with coverage especially lacking in the oceans. Beginning with Magsat in 1979–1980, and continuing with Ørsted, CHAMP, and SAC-C, high-precision magnetic satellite missions with global coverage have generated a over a decade of mostly continuous measurements, and show great promise as alternative or supplementary data sources to extend and refine these conductivity studies (e.g. Constable and Constable, 2004; Kuvshinov and Olsen, 2006), but also present special challenges. Specifically, the structure of the primary field must be accurately accounted for in the analysis, or the resulting conductivity estimates may be inaccurate.

The magnetospheric ring current and its associated magnetic field have long been known to be asymmetric (Campbell, 1997), especially during the main phase of magnetic storms (Daglis and Kozyra, 2002). Newer evidence indicates that this asymmetry is present even at longer periods (Balasis and Egbert, 2006), and global field modelers have begun to include up to degree and order 2 spherical harmonic structure in the model parameters for external fields (Olsen *et al.*, 2006, 2009). As the orbits of magnetic satellites are most easily described in the magnetospheric reference frame (*i.e.* the local-time (LT) frame), and are often either constant in LT (*e.g.* MagSat), or slowly precess through all LT’s (*e.g.* CHAMP), the asymmetry of the primary field can bias satellite studies more than those based on data from observatories that pass through all LT’s every 24 hours. Nonetheless, estimates

Table 3.1: Electrical conductivity profile of Earth model used in this study.

Region	Depth (km)	σ (S/m)
Upper mantle	0 – 400	0.01
Transition zone	400 – 800	0.1
Lower mantle	800 – 2871	1.0
Core	2871 – 6371	5×10^5

of the conductivity of Earth’s mantle based on magnetic data from observatories and satellites alike generally rely on the assumption that the primary field is well-described in geomagnetic coordinates by an external axial dipole (*i.e.* a spherical harmonic Y_l^m with degree $l = 1$ and order $m = 0$). This assumption makes it easier to estimate the internal and external parts of the field, and is justified by the fact that the asymmetric part of the primary field is believed to be much smaller in magnitude than the symmetric part (Constable, 2007).

However, response functions in the period range of 10^4 to 10^6 seconds are found to show significant bias when calculated from satellite data that have been binned by local time (Balasis *et al.*, 2004). That study, henceforth called ‘BEM’, motivates the work in this chapter. BEM showed that the observed bias can be qualitatively explained at periods of 5 and 10 days by Earth’s rotation through a primary field that includes a Y_2^1 component of 1/10 the magnitude of the dipole component, and has a maximum amplitude fixed at 8 pm. We extend the BEM analysis to eliminate certain approximations so that we can include all relevant periods, and estimate the magnitude of the Y_2^1 coefficient as a function of period assuming that all of the observed bias is a result of this type of asymmetry. For the purposes of this study, we model the Earth as a conducting sphere surrounded by perfectly insulating space. In our model, the electrical conductivity σ varies with radius only, and is described by Table 3.1.

3.2 Method

In the following analysis, we will neglect all components of Earth’s magnetic field except for the *primary* field \mathbf{B}_p generated by the magnetospheric ring current,

and the *secondary* field \mathbf{B}_s resulting from the associated induced electrical currents inside Earth. For simplicity, we will not consider Earth's core field or ionospheric fields, although these can have inductive effects. We will also neglect the crustal field. Thus we will refer to the *total* field \mathbf{B} as the sum of the primary and secondary fields:

$$\mathbf{B} = \mathbf{B}_p + \mathbf{B}_s. \quad (3.1)$$

In the insulating space surrounding Earth, an arbitrarily complex magnetic field \mathbf{B} can be represented as the negative gradient of a scalar magnetic potential Ψ . Since one of Maxwell's equations is

$$\nabla \cdot \mathbf{B} = 0, \quad (3.2)$$

we get

$$\nabla^2 \Psi = 0. \quad (3.3)$$

This is Laplace's equation. Its solution Ψ is called a *harmonic* function, and can be written as a sum of spherical harmonic terms given by

$$\Psi(r, \theta, \phi, t) = a \sum_{l=1}^{\infty} \sum_{m=-l}^l \Psi_l^m(r, \theta, \phi, t) \quad (3.4)$$

$$= a \sum_{l=1}^{\infty} \sum_{m=-l}^l \left[e_l^m(t) \left(\frac{r}{a} \right)^l + i_l^m(t) \left(\frac{a}{r} \right)^{l+1} \right] Y_l^m(\theta, \phi), \quad (3.5)$$

in the spherical coordinate system (r, θ, ϕ) , where r is distance from the origin at Earth's center, θ is geomagnetic colatitude, ϕ is geomagnetic longitude, and t is time. The time-dependent gauss coefficients $e_l^m(t)$ and $i_l^m(t)$ correspond to primary fields of external origin and secondary fields internal origin, respectively. The real parts of the spherical harmonics are defined by

$$Y_l^m = P_l^m(\cos \theta) \cos m\phi, \quad (3.6)$$

where P_l^m are associated Legendre functions. In the numerical parts of this chapter, a modified Schmidt-normalization is chosen to match that of BEM.

Along a given colatitude, Y_l^m will have zero crossings at $2m$ different longitudes. We can decompose any magnetic field derived from (3.5) into an

axisymmetric part

$$\mathbf{S} = \mathbf{S}_p + \mathbf{S}_s, \quad (3.7)$$

for which $m = 0$, and a non-axisymmetric part

$$\mathbf{N} = \mathbf{N}_p + \mathbf{N}_s, \quad (3.8)$$

for which $m \neq 0$. As a result, the primary field can now be written

$$\mathbf{B}_p = \mathbf{S}_p + \mathbf{N}_p, \quad (3.9)$$

and the secondary field is

$$\mathbf{B}_s = \mathbf{S}_s + \mathbf{N}_s, \quad (3.10)$$

For primary fields oscillating at a specific radial frequency ω , the external gauss coefficient for a given l and m is given by

$$e_l^m(t) = \hat{e}_l^m(\omega)e^{i\omega t}, \quad (3.11)$$

and will produce a secondary field described by the internal gauss coefficient

$$i_l^m(t) = \hat{i}_l^m(\omega)e^{i\omega t}, \quad (3.12)$$

for the same l and m , provided conductivity varies only with radius. The complex, frequency-dependent response function $Q_l(\omega)$ is the ratio of the Fourier amplitudes of the dipole coefficients:

$$Q_l(\omega) = \frac{\hat{i}_l^m(\omega)}{\hat{e}_l^m(\omega)}, \quad (3.13)$$

which has the same value, regardless of m . Weidelt's (1972) c -response, or *admittance*, is given by

$$c(\omega)_n = \frac{E_0(\omega)}{\partial_r E_0(\omega)}, \quad (3.14)$$

where E_0 is the amplitude of the electric field at Earth's surface, and ∂_r represents the radial derivative. Given the assumption that Earth's conductivity is radially stratified, for a given degree l this becomes (Constable, 1993)

$$c_l(\omega) = a \frac{l - (l + 1)Q_l(\omega)}{l(l + 1)(1 + Q_l(\omega))}. \quad (3.15)$$

The c -response gives information about the penetration depth of B . When it is known for all ω it can be inverted for an unique radial conductivity profile (Weidelt, 1972).

3.2.1 The Dipole Assumption

A common approach to global induction studies employs the assumption that the structures of \mathbf{B}_p and \mathbf{B}_s are accurately described by external and internal dipoles plus noise. Thus $l = 1$ and $m = 0$ in (3.5). Since

$$P_1^0(\cos \theta) = \cos \theta, \quad (3.16)$$

we get

$$\begin{pmatrix} -\cos(\theta) & 2\left(\frac{a}{r}\right)^3 \cos(\theta) \\ \sin(\theta) & \left(\frac{a}{r}\right)^3 \sin(\theta) \end{pmatrix} \begin{pmatrix} e_1^0(t) \\ i_1^0(t) \end{pmatrix} \approx \begin{pmatrix} B_r(t) \\ B_\theta(t) \end{pmatrix}. \quad (3.17)$$

Time-series of B_r and B_θ are measured by satellites and observatories and can be used to estimate the electric conductivity of Earth's mantle in the following way. First, the induction field is isolated in the data, often after subtracting some global field model $\mathbf{D}(r, \theta, \phi)$ from the measurements. Time-domain dipole coefficients $e_1^0(t)$ and $i_1^0(t)$ are estimated from vector measurements of $B_r(t)$ and $B_\theta(t)$ via (3.17), or from measurements of the scalar anomaly dD , which can be described by

$$dD = \frac{\mathbf{B} \cdot \mathbf{D}}{D}, \quad (3.18)$$

where D is the magnitude of \mathbf{D} . This equation reflects the fact that when the field model has much higher amplitude than the induction field, any component of the latter that is orthogonal to \mathbf{D} has very little impact on dD .

The dipole coefficients are transformed to the frequency domain with cross-spectral techniques, and then used to calculate estimates of $Q_1(\omega)$ and $c_1(\omega)$ from

$$Q_1(\omega) = \frac{\hat{i}_1^0(\omega)}{\hat{e}_1^0(\omega)}, \quad (3.19)$$

and

$$c_1(\omega) = a \frac{1 - 2Q_1(\omega)}{2 + 2Q_1(\omega)}, \quad (3.20)$$

where a is the radius of Earth. A radial profile of mantle conductivity can then be estimated by inverting the resulting estimate of $c_1(\omega)$.

Data from the dayside of Earth is contaminated by contributions from the Sq field (caused by solar heating of the atmosphere) and its induced counterpart.

These fields are not well-described by Y_1^0 spherical harmonics. Ground-based magnetic observatories will see the atmospheric Sq field as external and the induced response to Sq as internal, but magnetic satellites fly above the Sq source, and will see both Sq and its induced response as internal. For this reason, dayside satellite data is usually excluded from analysis.

3.2.2 Adding a Quadrupole Source

If there are non- Y_1^0 contributions to the induction field, then the estimate of $c_1(\omega)$ found using the above dipole assumption will be an inaccurate reflection of Earth's electromagnetic response because of two distinct effects. We will call the first of these *geometrical bias*, because it reflects the fact that the geometrical decomposition of the induction fields given by (3.17) is incorrect. The second effect we will call *amplitude bias*, since it reflects the fact that the amplitude and phase of the response $Q_l(\omega)$ is not equal for different l .

Since the primary field from the magnetospheric ring current is known to be stronger on the nightside of Earth than on the dayside (Campbell, 1997; Balasis *et al.*, 2004) even for long-period variations (Balasis and Egbert, 2006) it is useful to calculate the effect of non-axisymmetric fields on response functions. The simplest spherical harmonic term that qualitatively describes such an amplitude increase across Earth's diameter is Y_2^1 . In this section we explore the effect on estimates of $c_1(\omega)$ resulting from contamination of the primary field by a Y_2^1 component for a non-rotating Earth with conductivity described by Table 3.1. Although neglecting Earth's rotation makes this largely a theoretical exercise, it is nonetheless very useful one for building intuition with regard to the asymmetric global induction problem, and for motivating many of the steps that will be necessary when we add Earth rotation in Section 3.2.3. Time-varying asymmetry with rotation is a fairly complicated problem, and it is useful to approach it in stages.

We make the assumption that the primary field is described by a superposition of Y_1^0 and Y_2^1 terms that are coherent and in phase. For a given ω , the

axisymmetric part of the primary field \mathbf{S}_p is given by

$$\mathbf{S}_p(t) = \hat{e}_1^0(\omega) \left(-\cos \theta \hat{\mathbf{r}} + \sin \theta \hat{\boldsymbol{\theta}} \right) e^{i\omega t}, \quad (3.21)$$

As in Section 3.2.1, this primary field will produce an axisymmetric secondary field \mathbf{S}_s given by

$$\mathbf{S}_s(t) = \hat{i}_1^0(\omega) \left(\frac{a}{r} \right)^3 \left(2 \cos \theta \hat{\mathbf{r}} + \sin \theta \hat{\boldsymbol{\theta}} \right) e^{i\omega t}, \quad (3.22)$$

where $\hat{i}_1^0(\omega)$ is complex in order to allow for a phase difference between \mathbf{S}_p and \mathbf{S}_s .

The non-axisymmetric part of the primary field \mathbf{N}_p at the same frequency is given by the gradient of the real part of a rotated Y_2^1 term with Fourier coefficient $\hat{e}_2^1(\omega) = \beta(\omega) \hat{e}_1^0(\omega)$. Since

$$P_2^1(\cos \theta) = \frac{\sqrt{3}}{2} \sin 2\theta, \quad (3.23)$$

we get

$$\begin{aligned} \mathbf{N}_p(t) = \hat{e}_2^1(\omega) \sqrt{3} \frac{r}{a} \left(\right. & - \sin 2\theta \cos(\phi_1) \hat{\mathbf{r}} \\ & - \cos 2\theta \cos(\phi_1) \hat{\boldsymbol{\theta}} \\ & \left. + \cos \theta \sin(\phi_1) \hat{\boldsymbol{\phi}} \right) e^{i\omega t}, \end{aligned} \quad (3.24)$$

where $\phi_1 = \phi - \phi_0$, and ϕ_0 is the longitude of the peak amplitude.

The non-axisymmetric secondary fields \mathbf{N}_s generated by this primary field will have the form

$$\begin{aligned} \mathbf{N}_s(\omega) = \hat{i}_2^1(\omega) \sqrt{3} \left(\frac{a}{r} \right)^4 \left(\right. & \frac{3}{2} \sin 2\theta \cos(\phi_1) \hat{\mathbf{r}} \\ & - \cos 2\theta \cos(\phi_1) \hat{\boldsymbol{\theta}} \\ & \left. + \cos \theta \sin(\phi_1) \hat{\boldsymbol{\phi}} \right) e^{i\omega t}. \end{aligned} \quad (3.25)$$

We examine the effect of Y_2^1 contamination on estimates of $c_1(\omega)$ in a non-rotating Earth by simulating satellite magnetic field measurements and using (3.19) and (3.20) to produce response function estimates. We adopt the value $e_1^0(\omega) = 100$ nT for all ω and note that it has no imaginary component. Initially, we set $\beta(\omega) = 0.1$ for all ω as suggested by BEM, and $\phi_0 = 0^\circ$. Values of $\hat{i}_1^0(\omega)$ are computed

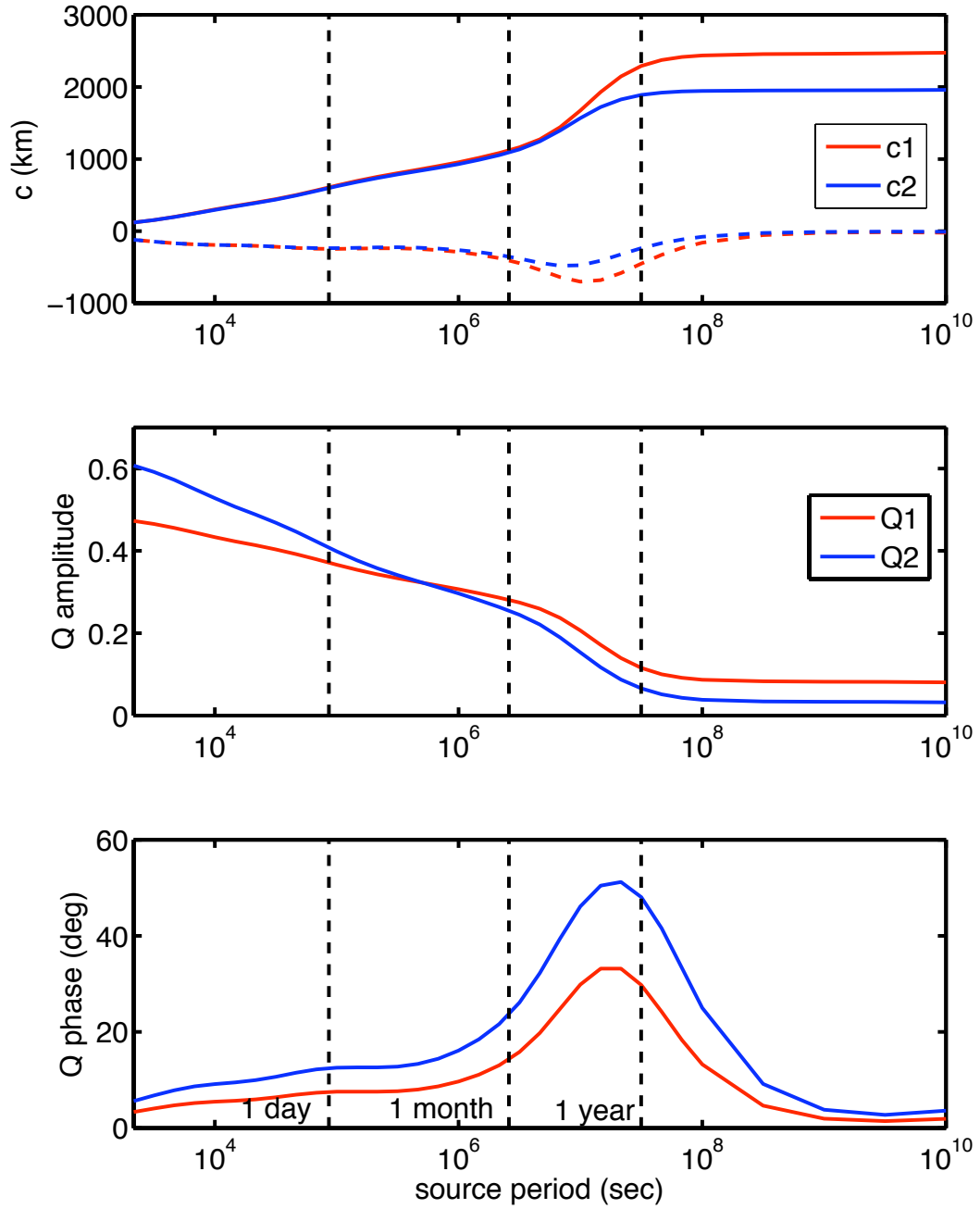


Figure 3.1: Top panel: the real (solid) and imaginary (dashed) parts parts of c_1 (red) and c_2 (blue). Middle panel: the amplitude of Q_1 (red) and Q_2 (blue). Bottom panel: the phase in degrees of Q_1 (red) and Q_2 (blue). Dashed black vertical lines indicate reference periods of 1 day, 1 month, and 1 year.

analytically for each ω (see Section 2.5), while values of $\hat{i}_2^1(\omega)$ are calculated from frequency-domain FlexPDE solutions of the fully 3D induction equations without surface conductance as described in Chapter 2.

The FlexPDE method requires the induction problem to be stated in terms of the vector potential \mathbf{A} , and requires the variables to be described in cartesian coordinates. The cartesian translation of (3.24) is

$$\mathbf{N}_p(t) = -\frac{\hat{e}_2^1(\omega)\sqrt{3}}{a} (z \hat{\mathbf{x}} + x \hat{\mathbf{z}}) e^{i\omega t}, \quad (3.26)$$

and the vector potential required to generate it is

$$\mathbf{A}(t) = \frac{\hat{e}_2^1(\omega)}{a\sqrt{3}} (xy \hat{\mathbf{x}} + (z^2 - x^2) \hat{\mathbf{y}} - yz \hat{\mathbf{z}}) e^{i\omega t}, \quad (3.27)$$

where $\hat{\mathbf{z}}$ is aligned with the geomagnetic axis, $\hat{\mathbf{x}}$ points along $\phi = 0^\circ$, and $\hat{\mathbf{y}}$ completes the right-handed triple.

Secondary fields were calculated for 30 values of ω corresponding to periods ($T = 2\pi/\omega$) between 2.5 hours and 317 years, and are interpolated as needed. A plot of $Q_1(T)$ and $Q_2(T)$ is given in Figure 3.1, where Q_2 is calculated from

$$Q_2(\omega) = \frac{\hat{i}_2^1(\omega)}{\hat{e}_2^1(\omega)}. \quad (3.28)$$

In global induction studies, periods beyond 100 days are rarely analyzed because the secular variation of Earth's core field contaminates the long-period data, but the addition of Earth rotation in Section 3.2.3 will make these long-period responses useful. Note that Earth's highly conducting core prevents the amplitude of the response from reaching zero even at very long periods.

Using these values of $Q_1(T)$ and $Q_2(T)$, we simulated the total induction field in the frequency domain for a non-rotating Earth for periods between 2.7 hours and 3 years. These fields were calculated for colatitudes $40^\circ \leq \theta \leq 140^\circ$ along 24 evenly spaced constant-longitude half-orbits at an altitude of 400 km. We used (3.17) to estimate $\hat{e}_1^0(T)$ and $\hat{i}_1^0(T)$ for each period, and used (3.19) and (3.20) to calculate the measured response of each profile separately in order to explore the effect of employing the dipole assumption on fields that were contaminated with Y_2^1 structure. The resulting profiles are shown in Figure 3.2.

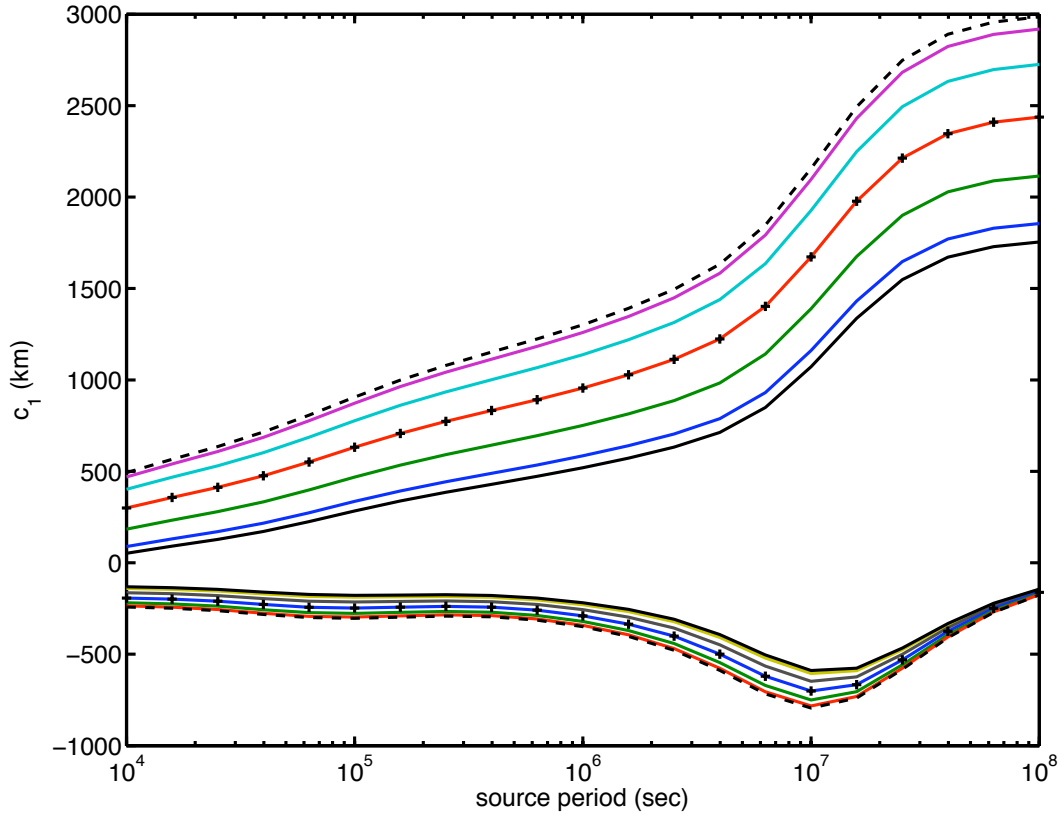


Figure 3.2: Total bias from a Y_2^1 contaminated primary field without rotation. The real (positive) and imaginary (negative) parts of $c_1(T)$ with $\beta = 0.1$ and $\phi = 0^\circ$ are shown for seven longitudes evenly spaced between 0° and 180° . The solid black curve indicates the response for $\phi = 0^\circ$, the dashed black curve indicates the response for $\phi = 180^\circ$, and the plus signs indicate the response for a pure Y_1^0 primary field.

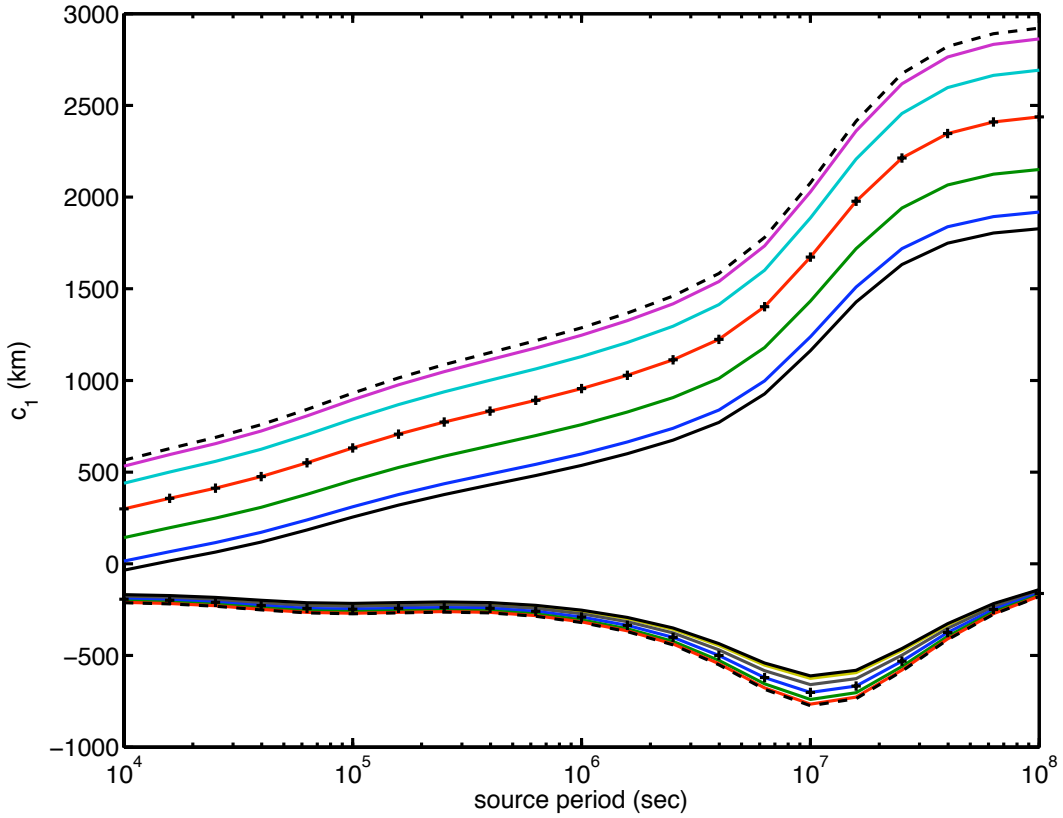


Figure 3.3: Isolation of the geometrical effect in bias from a Y_2^1 contaminated primary field in a non-rotating Earth. The real (positive) and imaginary (negative) parts of $c_1(T)$ with $\beta = 0.1$ and $\phi = 0^\circ$ are shown for seven longitudes evenly spaced between 0° and 180° . In this case, $Q_1(T)$ was used to calculate $\hat{i}_2^1(T)$. The solid black curve indicates the response for $\phi = 0^\circ$, the dashed black curve indicates the response for $\phi = 180^\circ$, and the plus signs indicate the response for a pure Y_1^0 primary field.

The azimuthal asymmetry in the measured fields from this simulation generates a considerable ϕ -dependent bias in c_1 , which is slightly larger for long periods than for shorter periods. The bias for longitude ϕ is equivalent to that for $-\phi$ because the fields in this model are an even function of longitude. The bias is much more evident in the real part of c_1 than in the imaginary part, and has opposite sign in these two components.

Similar simulations can be done to demonstrate that the bias seen in Figure 3.2 is mainly due to the inaccurate geometric decomposition that comes from the false assumption contained in (3.16). We calculate exactly the same fields and

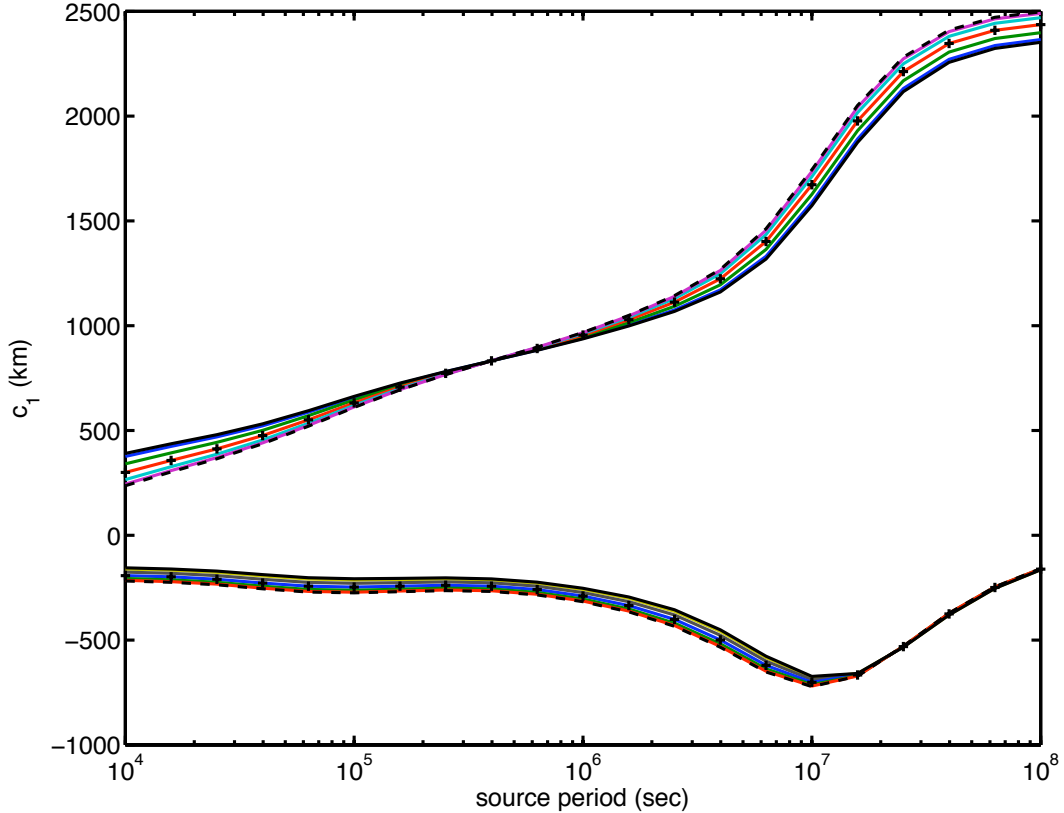


Figure 3.4: Isolation of the amplitude effect in bias from a Y_2^1 contaminated primary field in a non-rotating Earth. The real (positive) and imaginary (negative) parts of $c_1(T)$ with $\beta = 0.1$ and $\phi = 0^\circ$ are shown for seven longitudes evenly spaced between 0° and 180° . In this case, the asymmetric fields have the shape of Y_1^0 fields weighted by $\cos \phi$. The solid black curve indicates the response for $\phi = 0^\circ$, the dashed black curve indicates the response for $\phi = 180^\circ$, and the plus signs indicate the response for a pure Y_1^0 primary field.

make only the substitution

$$\hat{i}_2^1(T) = Q_1(T)e_2^1(T), \quad (3.29)$$

which generates magnetic fields that have the same geometry as before, but with secondary amplitudes that correspond to induction with dipolar primary fields. This modification eliminates amplitude bias and allows us to examine the purely geometrical effect of Y_2^1 contamination. The resulting estimates for $c_1(T)$ are shown in Figure 3.3, and demonstrate nearly the same bias seen in Figure 3.2, but with a more consistent amplitude across all periods.

Alternatively, we can study amplitude bias by using $Q_2(T)$ to calculate $\hat{i}_2^1(T)$, but giving \mathbf{N} the geometrical shape of a dipole weighted by the cosine of the longitude, or

$$\mathbf{N}'_p(t) = \hat{e}_2^1(\omega)\sqrt{3} \left(-\cos\theta \hat{\mathbf{r}} + \sin\theta \hat{\boldsymbol{\theta}} \right) \cos\phi e^{i\omega t}, \quad (3.30)$$

and

$$\mathbf{N}'_s(t) = \hat{i}_2^1(\omega)\sqrt{3} \left(\frac{a}{r} \right)^3 \left(2\cos\theta \hat{\mathbf{r}} + \sin\theta \hat{\boldsymbol{\theta}} \right) \cos\phi e^{i\omega t}, \quad (3.31)$$

where we include a factor of $\sqrt{3}$ to keep the magnitude of theta component consistent with the previous asymmetric fields. This exercise eliminates geometrical bias and isolates the bias resulting from the difference between the amplitudes of Q_1 and Q_2 . The resulting estimates for $c_1(T)$ are shown in Figure 3.4, and they show a much smaller bias than what is seen in Figures 3.2 and 3.3, demonstrating that the geometrical effect of Y_2^1 contamination is the dominant factor in the bias seen in Figure 3.2. The shorter period bias in the real part of c_1 has opposite sign from that at long periods. Thus the amplitude bias slightly counteracts the geometrical bias at short periods and reinforces it at long periods.

It should be noted that the $\cos\phi$ -weighted Y_1^0 primary field described in (3.30) will not actually create the similarly weighted Y_1^0 secondary field described in (3.31) in a real system. The plot shown in Figure 3.4 is intended only to demonstrate the dominance of geometrical bias as compared to amplitude bias in a radially conductive system with Y_2^1 contamination.

We used FlexPDE to calculate the secondary fields that are actually produced when our Earth model is excited with the field described by (3.30). This primary field, which is described very simply in the cartesian frame as

$$\mathbf{N}'_p(t) = -\frac{\hat{e}_2^1(\omega)\sqrt{3}x}{a} \hat{\mathbf{z}}e^{i\omega t}, \quad (3.32)$$

with vector potential

$$\mathbf{A}(t) = -\frac{\hat{e}_2^1(\omega)\sqrt{3}x^2}{2a} \hat{\mathbf{z}}e^{i\omega t}, \quad (3.33)$$

and is identical in the z -component to a Y_2^1 primary field, but lacks a cross polar x -component seen in (3.26). In this respect, the field given in (3.30) can be considered to be a simpler field than that given in (3.24), while still generating the desired

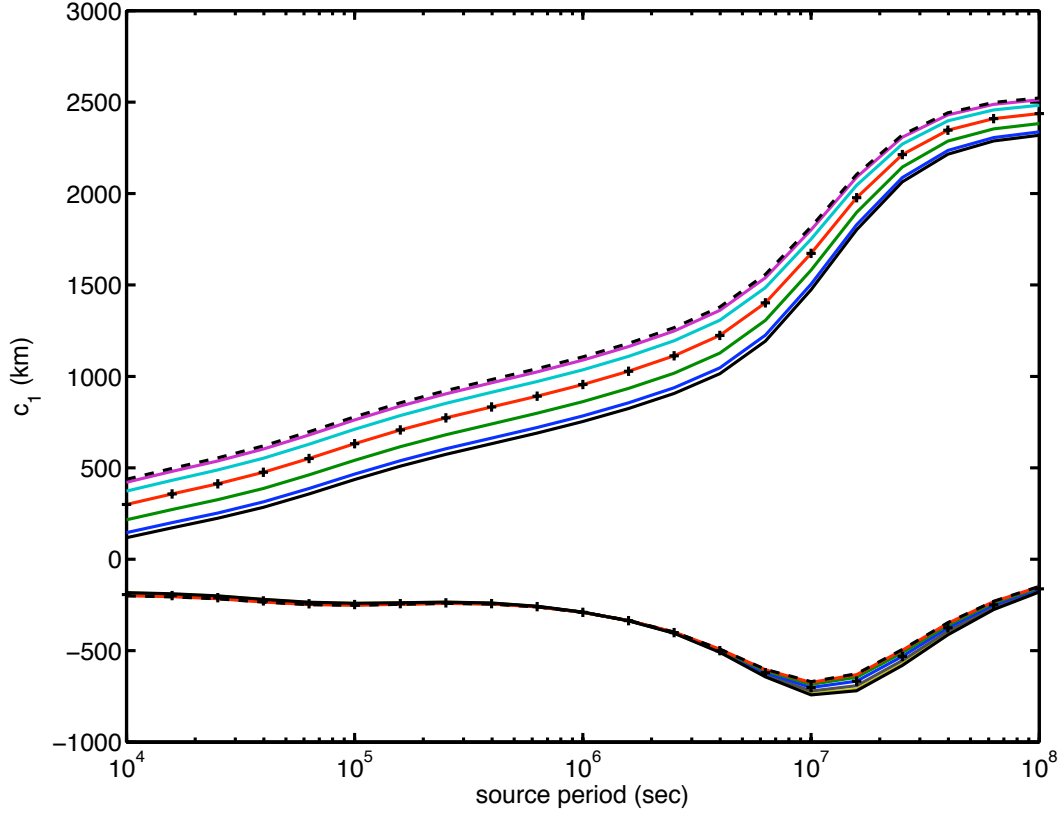


Figure 3.5: Total bias from a $\cos \phi$ -weighted Y_1^0 primary field in a non-rotating Earth. The real (positive) and imaginary (negative) parts of $c_1(T)$ with $\beta = 0.1$ and $\phi = 0^\circ$ are shown for seven longitudes evenly spaced between 0° and 180° . In this case, the asymmetric primary fields have the shape of Y_1^0 fields weighted by $\cos \phi$, while the asymmetric secondary fields have the internal Y_2^1 geometry that would actually result from this type of excitation. The solid black curve indicates the response for $\phi = 0^\circ$, the dashed black curve indicates the response for $\phi = 180^\circ$, and the plus signs indicate the response for a pure Y_1^0 primary field.

increase in nightside amplitude. Thus it is a reasonable primary field with which to explore the effect of asymmetry on response functions.

The calculations show that the secondary field resulting from N'_p is very well described by an internal Y_2^1 as in (3.25) with coefficient $\hat{d}_2^1(\omega)$, and that for any given ω

$$\hat{d}_2^1(\omega) \approx 0.429 \hat{i}_2^1(\omega). \quad (3.34)$$

Total induction fields were calculated for this model and c_1 estimates were produced in the same manner as those in Figures 3.2 – 3.4. These estimates are shown in Figure 3.5, and show a similar bias to that of true Y_2^1 contamination, but with much smaller amplitude and a slight decrease in bias at long periods. The bias in the imaginary part of c_1 is almost vanishing for most periods.

3.2.3 Adding Rotation

In this section, we extend the preceding discussion to include Earth's rotation through the time-varying magnetospheric primary field that includes Y_1^0 and Y_2^1 components. Allowing for Earth rotation complicates the exploration of bias in response functions because the primary field is most easily described in the stationary magnetospheric reference frame (r, θ, ϕ) , while induction occurs in the rotating frame of Earth (r', θ', ϕ') , where

$$r' = r, \quad (3.35)$$

$$\theta' = \theta, \quad (3.36)$$

$$\phi' = \phi - \omega_r t, \quad (3.37)$$

and ω_r is the radial frequency corresponding to a rotational period of 24 hours. For simplicity, we ignore the distinction between the geomagnetic and geographic reference frames, and assume that $\phi' = 0$ is positioned at local midnight at time $t = 0$.

The time-variation of the primary field as seen at a particular location on Earth's surface results from a combination of the field's true time-variation at radial frequency ω as seen in the stationary magnetospheric frame, and its spatial

variation as Earth rotates through it. Since rotation has no effect on axisymmetric fields, we limit our discussion to the asymmetric parts of the field. In the magnetospheric frame, N_p is the same as in (3.24), with potential Ψ_{N_p} that can be written

$$\Psi_{N_p}(t) = \hat{e}_2^1(\omega)K(r, \theta) \cos \phi_1 \cos(\omega t), \quad (3.38)$$

where

$$K(r, \theta) = \frac{r^2 \sqrt{3}}{2a} \sin 2\theta. \quad (3.39)$$

In the rotating Earth frame this potential is described by

$$\Psi'_{N_p}(t) = \hat{e}_2^1(\omega)K(r, \theta) \cos(\phi'_1 + \omega_r t) \cos(\omega t), \quad (3.40)$$

or, equivalently,

$$\Psi'_{N_p}(t) = \frac{1}{2} \hat{e}_2^1(\omega)K(r, \theta) \left[\cos(\phi'_1 + (\omega_r + \omega)t) + \cos(\phi'_1 + (\omega_r - \omega)t) \right]. \quad (3.41)$$

For insight into (3.41), it is useful to examine the potential seen on Earth as it rotates at arbitrary radial frequency Ω_r through a static external quadrupole of unit magnitude. This is given by

$$\Psi(t) = K(r, \theta) \cos(\phi'_1 + \Omega_r t). \quad (3.42)$$

Comparison of (3.41) and (3.42) indicates that the former describes a superposition of two external static quadrupoles rotating at effective radial frequencies

$$\omega^+ = \omega_r + \omega, \quad (3.43)$$

and

$$\omega^- = \omega_r - \omega, \quad (3.44)$$

with corresponding periods

$$T^+ = 2\pi/\omega^+ \quad (3.45)$$

and

$$T^- = 2\pi/\omega^-. \quad (3.46)$$

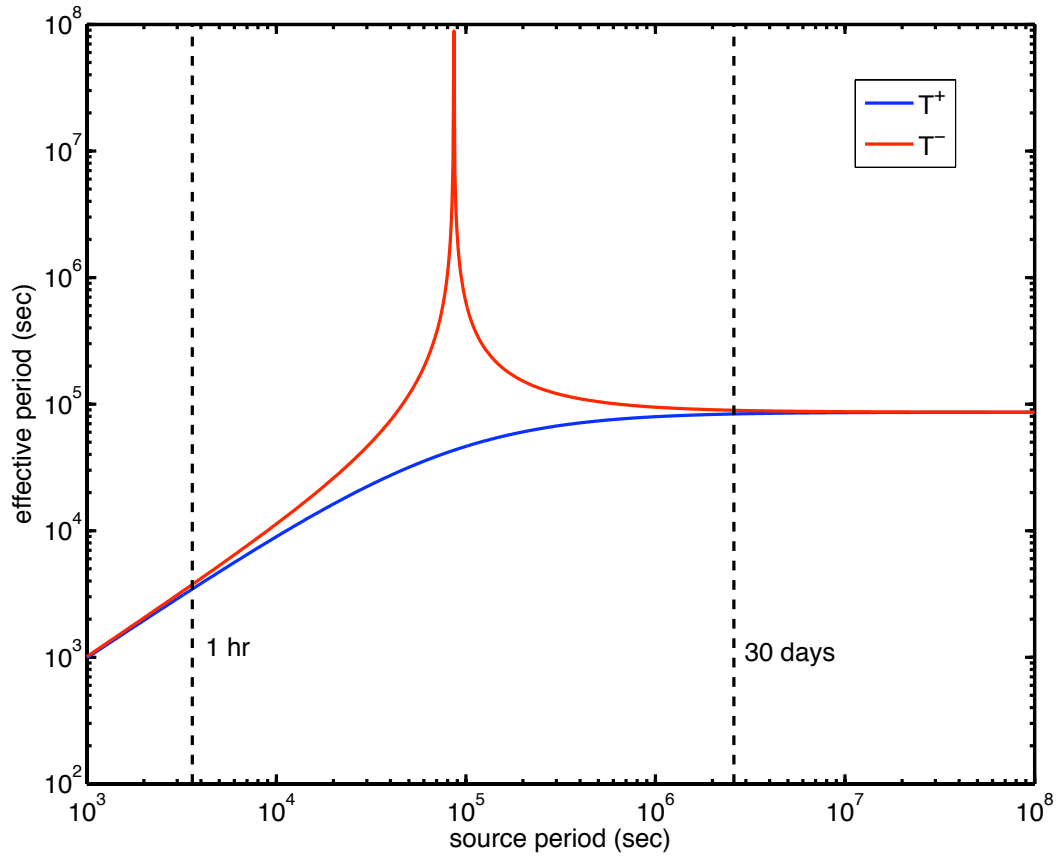


Figure 3.6: The absolute values of the effective oscillation periods seen in the rotating Earth frame plotted against the source oscillation period T seen in the magnetospheric frame. The blue curve is T^+ and the red curve is T^- . The latter is negative to the left of the vertical pole at $T = 1$ day and positive to the right. T^+ is positive everywhere.

A plot of these effective periods against source period T is shown in Figure 3.6, and shows that for source periods less than ~ 1 hour

$$T^+ \approx T^- \approx T. \quad (3.47)$$

These periods are shorter than the Nyquist period for satellite data, which is 90–120 minutes, so are not usually analyzed for studies using a single satellite. For source periods longer than ~ 30 days

$$T^+ \approx T^- \approx 1 \text{ day}. \quad (3.48)$$

This fact was exploited by BEM in their analysis, and was used at periods of 5 and 10 days to generate estimates of β and ϕ_0 .

Another feature of Figure 3.6 is the vertical pole in T^- at a source period of 1 day where ω approaches ω_r . The effect of this pole will be discussed shortly. For periods shorter than 1 day, T^- is negative, which indicates that the associated static quadrupole rotates in reverse.

The rotating, non-oscillatory quadrupole potential given in (3.42) can be written as a superposition of two time-varying, non-rotating potentials:

$$\Psi(t) = K(r, \theta) \left[\cos \phi'_1 \cos(\Omega_r t) + \sin \phi'_1 \sin(\Omega_r t) \right]. \quad (3.49)$$

Since a non-rotating, external Y_2^1 primary field will induce a non-rotating, internal Y_2^1 secondary field, (3.49) tells us that the secondary field produced by a non-oscillatory, rotating external quadrupole will be a non-oscillatory, rotating internal quadrupole. The temporal phase shift corresponding to the complex $\hat{i}_2^1(\Omega_r)$ will manifest as a constant rotational offset of the secondary field with respect to the primary field by a longitude of

$$\varphi(\Omega_r) = \arctan \left(\frac{\Im\{\hat{i}_2^1(\Omega_r)\}}{\Re\{\hat{i}_2^1(\Omega_r)\}} \right), \quad (3.50)$$

which corresponds to the amount of rotation that occurs during the time interval associated with the temporal phase.

Thus a primary field that is the superposition of two non-oscillatory, rotating external quadrupoles as described by (3.41) will produce two secondary

non-oscillatory, rotating internal quadrupoles described by

$$\Psi'_{Ns}(t) = \frac{1}{2}G(r, \theta) \left[\left| \hat{i}_2^1(\omega^+) \right| \cos(\phi'_1 + \omega^+ t - \varphi^+) \right. \\ \left. + \left| \hat{i}_2^1(\omega^-) \right| \cos(\phi'_1 + \omega^- t - \varphi^-) \right], \quad (3.51)$$

where

$$G(r, \theta) = \frac{a^4 \sqrt{3}}{2r^3} \sin 2\theta. \quad (3.52)$$

The rotational phase shifts $\varphi^+ = \varphi(\omega^+)$ and $\varphi^- = \varphi(\omega^-)$ will in general not be equal to each other, as they will each reflect Earth's response at different frequencies. At periods shorter than 1 day, φ^- must have reversed sign to correctly reflect the reversed rotational direction associated with negative ω^- .

Earth rotation has little effect on observatory response functions, since these are calculated in the rotating frame. The amplitude and phase of the measured secondary field appropriately reflects the effective frequency of the measured primary field, even though this frequency is not equal to the source frequency. At any single longitude, the rotational phase shift described above will be seen as the appropriate temporal phase shift of the secondary field relative to the primary field. Thus the rotation signal manifests as deviations in measurements of $e_1^0(t)$ and $i_1^0(t)$ that result from the response and geometrical biases discussed in Section 3.2.2. The bias in the estimate of Q_1 that results from these deviations will have opposite signs on opposite sides of Earth, so it will tend to cancel itself in long time-series. This is confirmed by time-domain FlexPDE simulations of observatory measurements in a rotating Earth with Y_2^1 contamination that show no longitude-dependent bias.

The effect of rotation on satellite response functions can be drastic. These are calculated for locations that are nearly stationary in the magnetospheric frame, with a primary quadrupole potential for a given frequency described by (3.38), which can be usefully rewritten

$$\Psi_{Np}(t) = \frac{1}{2} \hat{e}_2^1(\omega) K(r, \theta) [\cos(\phi_1 + \omega t) + \cos(\phi_1 - \omega t)]. \quad (3.53)$$

Equation (3.53) reflects the fact that an oscillating stationary quadrupole can be thought of as the sum of two static quadrupoles, each with half the original

amplitude, rotating in opposite directions. After being transformed into the magnetospheric frame by (3.37), the secondary potential from (3.51) will be

$$\Psi_{Ns}(t) = \frac{1}{2}G(r, \theta) \left[\left| \hat{i}_2^1(\omega^+) \right| \cos(\phi_1 + \omega t - \varphi^+) \right. \\ \left. + \left| \hat{i}_2^1(\omega^-) \right| \cos(\phi_1 - \omega t - \varphi^-) \right]. \quad (3.54)$$

Thus the secondary fields will also be described by static quadrupoles rotating in opposite directions with rotational frequency ω , but will have response characteristics appropriate to ω^+ and ω^- . As in the rotating frame, when the + and - parts are considered separately and the Earth is viewed as a whole, phase of \hat{i}_2^1 will manifest in the stationary frame as a longitude offset between the secondary and primary rotating quadrupoles. At a single local time, this will appear as a temporal phase shift.

Global induction is rarely studied at periods less than a few hours (because of near-surface inhomogeneity and the complexity of the source fields in the ionosphere) or greater than 100 days (because of contamination by the secular variation of the main field). It is nonetheless instructive to consider three limiting cases: very long periods, very short periods, and periods near one day.

At very long periods where (3.48) applies, we can make the approximation that the amplitudes and phases of both parts of the secondary field are approximately equal. The secondary quadrupoles will combine to manifest as a single, non-rotating quadrupole that oscillates at frequency ω , but has an amplitude corresponding to effective frequencies ω^+ and ω^- . This mismatch can bias c_1 estimates considerably since secondary field amplitudes generally increase with frequency, as seen in the middle panel of Figure 3.1. This will make the responses unexpectedly large at these long periods. The secondary quadrupole will be rotated by a longitude of φ^+ with respect to the primary quadrupole. Perhaps counterintuitively, there will be no temporal phase shift between the two.

At very short periods (3.47) applies. As in the long-period case, the secondary field will appear as an oscillating, non-rotating quadrupole, but unlike the long-period case, the rotational phase shifts of the + and - parts will have equal magnitude and opposite sign, so the secondary quadrupole will have a temporal

phase shift relative to the primary field, but will have no rotational offset. Because of (3.47), both the response characteristics of the secondary field will be appropriate to the frequency of the source field. Thus the very short-period case is indistinguishable from that of Y_2^1 contamination in a non-rotating Earth. This reflects the fact that each complete rotation of the Earth will contain dozens of short-period oscillations, so the Earth can be considered to be effectively stationary during each of them.

At periods near 1 day, ω^+ corresponds to periods near 12 hours, while ω^- corresponds to a vertical asymptote where the absolute value of T^- rapidly approaches infinity from both directions, as seen in Figure 3.6. Although the effective period changes very rapidly in this region, the amplitude and rotational phase become nearly constant at long periods, so the vertical pole in T^- has very little effect other than the change in sign of rotational phase mentioned above.

We perform frequency-domain satellite measurements of a rotating Earth with Y_2^1 contamination by calculating the primary and secondary Y_1^0 fields and the primary Y_2^1 fields as above. The secondary Y_2^1 fields are derived from (3.55), given in the frequency-domain by

$$\begin{aligned} \Psi_{Ns}(\omega) = \frac{1}{2}G(r, \theta) & \left[(1 - i) \left| \hat{i}_2^1(\omega^+) \right| \cos(\phi_1 - \varphi^+) \right] e^{i\omega t} \\ & + (1 + i) \left| \hat{i}_2^1(\omega^-) \right| \cos(\phi_1 - \varphi^-) e^{i\omega t} \end{aligned} \quad (3.55)$$

where the imaginary parts are rotated by $\pm 90^\circ$ to correctly produce the rotation of static quadrupoles described above. The coefficients \hat{i}_2^1 are calculated in the same way as in Section 3.2.2. For $T^- > 10^{10}$ seconds near source periods of one day, the approximation $\hat{i}_2^1(T^-) = \hat{i}_2^1(10^{10} \text{ sec})$ is used. Otherwise, no long- or short-period approximations are required.

BEM calculated the LT bias in c_1 estimates at periods of 5 and 10 days in a manner very similar to the one we used in Section 3.2.2, but using simulated scalar anomalies instead of simulated vector measurements. The BEM authors generated scalar anomalies via (3.18) using a \mathbf{B} reflected both Y_1^0 and Y_2^1 terms, and then used those anomalies to estimate dipole coefficients with the same equation after replacing \mathbf{B} with one that only accounted for Y_1^0 structure.

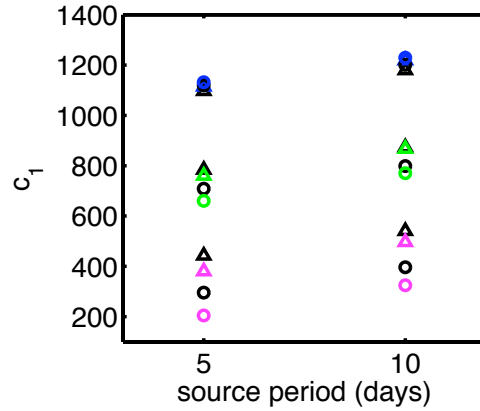


Figure 3.7: Synthetic estimates of the real part of c_1 for a Y_2^1 contaminated primary field in a rotating Earth, for $\beta = 0.1$ and $\phi_0 = -60^\circ$ (triangles), and for $\beta = 0.125$ and $\phi_0 = -65^\circ$ (circles). BEM estimates for 10 pm (blue), 2 am (green), and 6 am (pink), are compared to estimates from this work (black).

We reproduce BEM’s results, which are displayed with ours in Figure 3.7 for $\beta = 0.1$, and $\phi_0 = -60^\circ$, and for $\beta = 0.125$, and $\phi_0 = -67.5^\circ$. To most closely match BEM, we used the scalar anomaly method, modeling the Earth’s main field as in internal dipole with a $30 \mu\text{T}$ coefficient, and extending our range of colatitudes to match theirs: $25^\circ \leq \theta \leq 155^\circ$. The estimates match qualitatively, with maximum disagreement of less than 100 km (for biases of roughly 600 km) that can be accounted for by different conductivity profiles used in the estimates of Q_1 and Q_2 . Note that BEM do not supply values for the imaginary parts of c_1 in the $\beta = 0.1$ case, and their estimates of this value for the $\beta = 0.125$ case are nearly identical to each other. For this reason, we only include the real parts of all estimates in the figure.

BEM used the long-period approximation (3.48) for their calculations. While our method does not rely on this approximation, we used it to produce a second set of estimates in the interest of quantifying the approximation’s effect. The estimates made with and without the approximation were nearly identical, with an RMS misfit of about 2 km and a maximum misfit of 10 km, demonstrating the applicability of this approximation at periods of 5 and 10 days.

We used our method to calculate LT-dependent c_1 estimates at periods be-

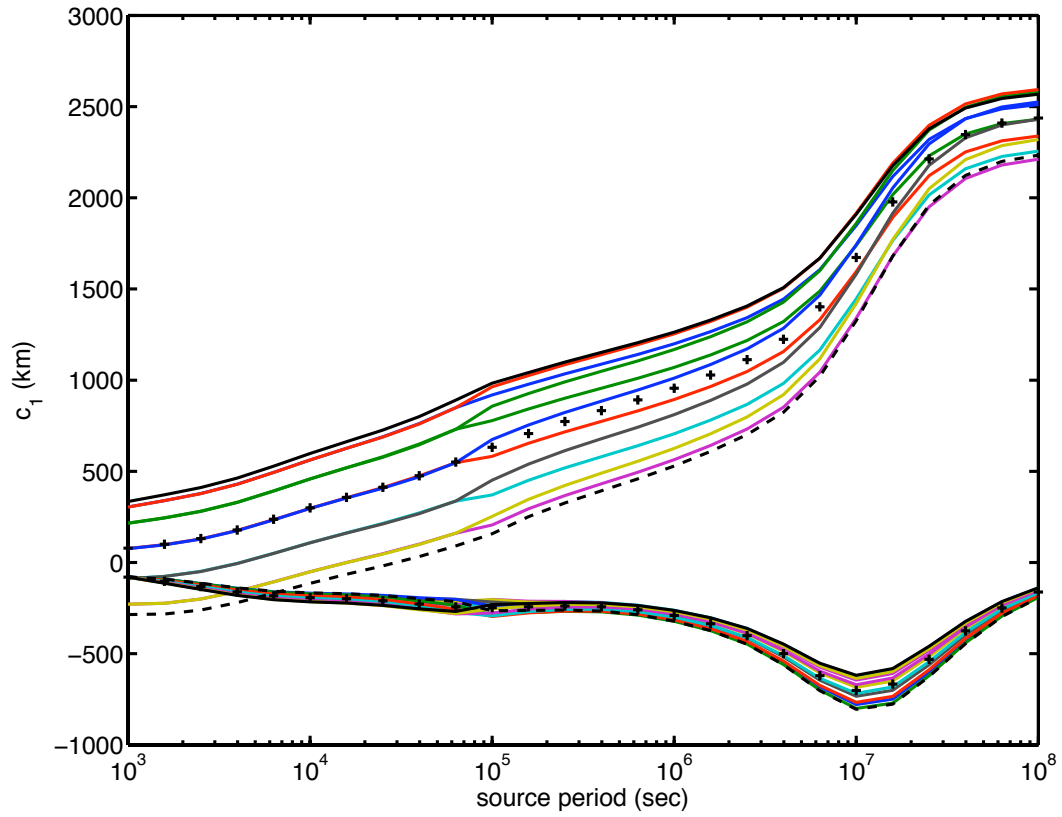


Figure 3.8: Bias from a Y_2^1 contaminated primary field in a rotating Earth using the scalar decomposition method. The real (positive) and imaginary (negative) parts of $c_1(T)$ with $\beta = 0.1$ and $\phi = 0^\circ$ are shown for 12 longitudes evenly spaced around the globe. The solid black curve indicates the response for $\phi_1 = 0^\circ$, the dashed black curve indicates the response for $\phi_1 = 180^\circ$, and the plus signs indicate the response for a pure Y_1^0 primary field.

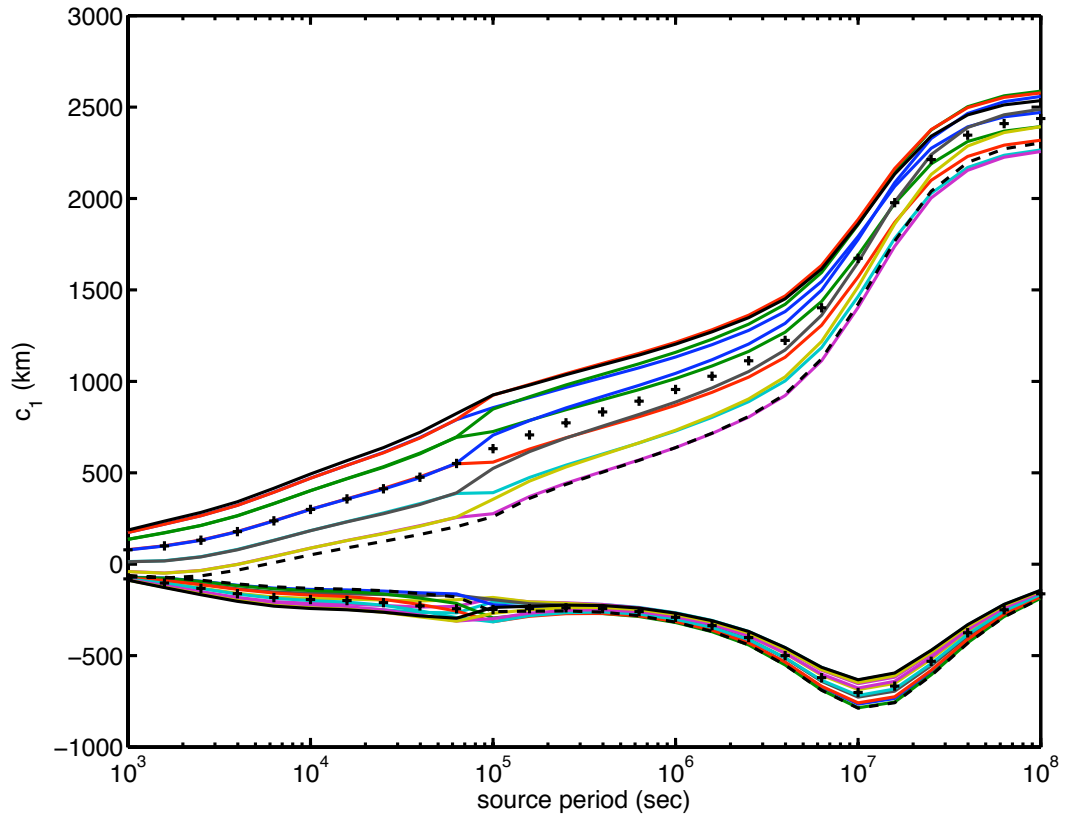


Figure 3.9: Bias from a Y_2^1 contaminated primary field in a rotating Earth using the vector decomposition method. The real (positive) and imaginary (negative) parts of $c_1(T)$ with $\beta = 0.1$ and $\phi = 0^\circ$ are shown for 12 longitudes evenly spaced around the globe. The solid black curve indicates the response for $\phi_1 = 0^\circ$, the dashed black curve indicates the response for $\phi_1 = 180^\circ$, and the plus signs indicate the response for a pure Y_1^0 primary field.

tween 10^4 and 10^8 seconds for a rotating Earth model with Y_2^1 contamination. For these calculations we used $\beta = 0.1$ and $\phi_0 = -60^\circ$ for all periods. Figure 3.8 shows results that were calculated using the scalar anomaly method, and colatitude range $25^\circ \leq \theta \leq 155^\circ$, and Figure 3.9 shows results that were calculated using the vector measurement method and colatitude range $40^\circ \leq \theta \leq 140^\circ$.

In general, the vector method can be used with a more restricted range of colatitudes centered on the geomagnetic equator, while the scalar method requires longer satellite tracks that extend closer to the poles, where there is more difference in orientation between the internal and external dipole fields. Measurements from scalar satellite magnetometers are thought to be more accurate than vector measurements, which rely on star cameras for orientation. This increased accuracy may be counteracted by the fact that many main field models do a poor job of fully accounting for auroral currents, which can be significant at higher latitudes.

Synthetic tests of Y_1^0 induction fields with and without gaussian noise show that both scalar and vector methods work quite well for pure dipoles, but Figures 3.8 and 3.9 demonstrate that the c_1 bias is much greater when the scalar anomaly method is used in the presence of Y_2^1 contamination. This argues against the use of the scalar method in traditional satellite induction studies, but opens the possibility of gaining information about the structure of the field from comparisons between response functions calculated from the two methods.

Both figures show a LT bias in the responses that is fairly consistent over the full range of periods, with a slight increase in the bias of the real part of c_1 in the middle of the spectrum, and a slight decrease in the bias of the imaginary part in the same place. The real and imaginary parts both kink slightly at periods of one day because of the change in sign of the rotational phase. The direction of this kink has opposite sign on opposite sides of Earth. It is notable that the bias has reversed sign compared to the non-rotating models. The rotating models have the maximum positive bias in the real part of c_1 at $\phi_1 = 0^\circ$ and the maximum negative bias at $\phi_1 = 180^\circ$. In the non-rotating models, these are reversed, with the maximum positive bias at $\phi_1 = 180^\circ$ and maximum negative bias at $\phi_1 = 0^\circ$.

We performed similar simulations with a rotating version of the $\cos\phi$ -

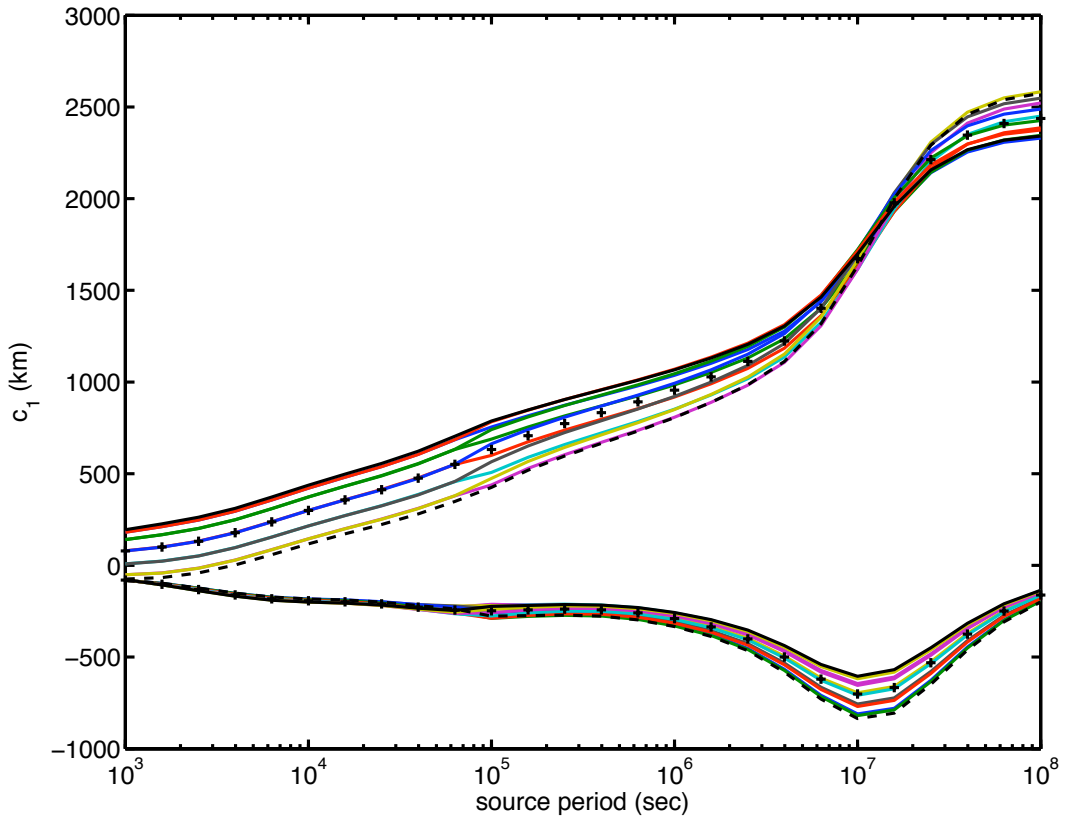


Figure 3.10: Bias from a $\cos \phi_1$ -weighted Y_1^0 primary field in a rotating Earth using the vector decomposition method. The real (positive) and imaginary (negative) parts of $c_1(T)$ with $\beta = 0.1$ and $\phi = 0^\circ$ are shown for 12 longitudes evenly spaced around the globe. The solid black curve indicates the response for $\phi = \phi_0$, the dashed black curve indicates the response for $\phi = \phi_0 + 180^\circ$, and the plus signs indicate the response for a pure Y_1^0 primary field.

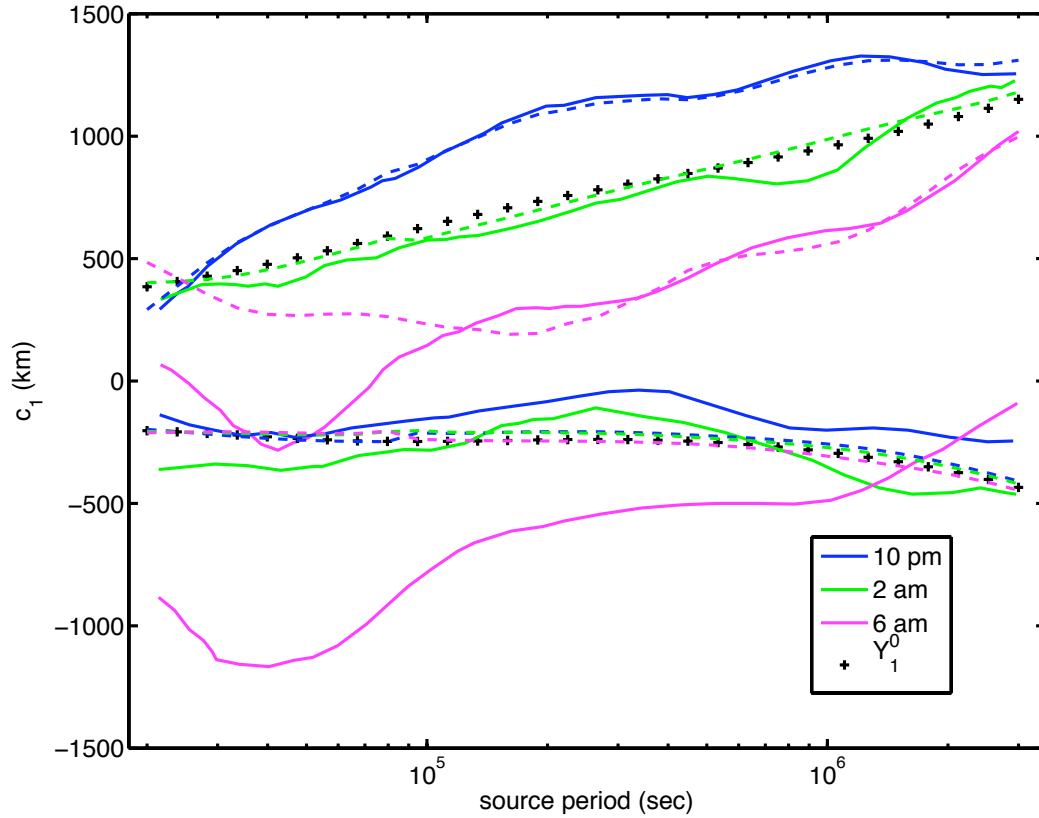


Figure 3.11: Recreation of Balasis bias for a Y_2^1 contaminated primary field in a rotating Earth. The real (positive) and imaginary (negative) parts of $c_1(T)$ with $\beta = 0.1$ and $\phi = 0^\circ$ are shown for local time subsets of 10 pm (blue), 2 am (green), and 6 am (pink). The solid curves indicate the empirical bias found by BEM. The dashed curves indicate the synthetic bias produced by our method. The plus signs indicate the response for a pure Y_1^0 primary field.

weighted Y_1^0 primary field given in (3.30) and its associated induced rotating Y_2^1 secondary field. Response functions were calculated from these simulations, using the vector method, $\beta = 0.1$, $\phi_0 = -60^\circ$, and $40^\circ \leq \theta \leq 140^\circ$. These are shown in Figure 3.10, and when compared to the fully Y_2^1 models, show a similar reduction in bias to that found in Section 3.2.2. The bias in the real part of the response switches sign at long period in this case, a fact that remains true when scalar decomposition is used..

We estimate the period-dependent values of β and ϕ_0 necessary to recreate the BEM bias in c_1 using the scalar method and the assumption that this bias is entirely caused by coherent Y_2^1 contamination in the primary and secondary fields.

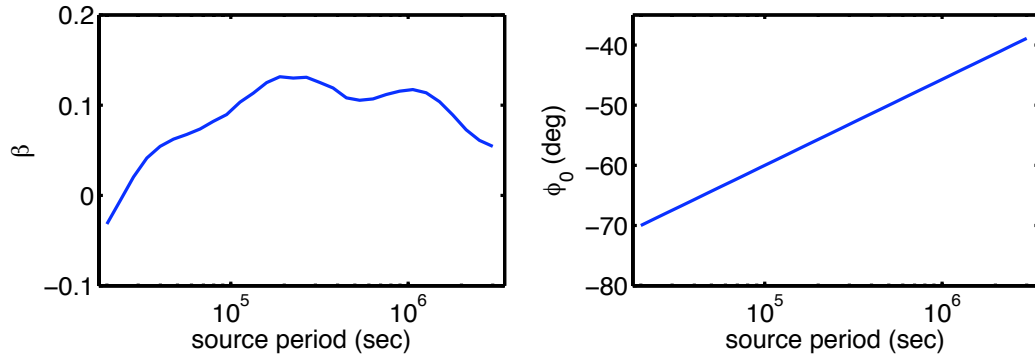


Figure 3.12: Values of $\beta(\omega)$ and $\phi_0(\omega)$ used to create Figure 3.11.

To approximate the amplitude of the bias we assume that β is a linear function of the BEM bias for the 10 pm LT subset. To approximate the asymmetry of the bias between the 10 pm and 6 am LT curves, we assume that ϕ_0 is simply a linear function of logperiod. We use a perturbational approach to match the bias in the real part of c_1 in the period range $2 \times 10^4 \leq T \leq 3 \times 10^6$ seconds. The short-period range for BEM's 6 am LT result was not considered in the fit, since BEM attributed its structure to low signal strength in the dawn LT sector. The resulting fit is shown in Figure 3.11, and the $\beta(T)$ and $\phi_0(T)$ estimates used to produce it are shown in Figure 3.12. The fit to the bias in the real part is very good, excluding the short-period dawn sector. The maximum value of β is ~ 0.13 at periods just over 1 day. This corresponds to a fairly large difference of ~ 45 nT in B_θ on opposite sides of Earth when we assume that $\hat{e}_1^0 = 100$ nT. The fit to the imaginary part of c_1 is not as good, with the modeled bias being very small compared to the BEM bias, even when the dawn sector result is excluded. Using our technique to fit the bias in the imaginary part would result in overly large biases in the real part since the imaginary bias from our method is always very small compared to the real bias. Some other effect must be invoked to explain this discrepancy. Possibilities include lack of coherence between the symmetric and asymmetric fields and other spherical harmonic terms, although these were not explored in this study.

We applied the same technique to estimate $\beta(T)$ and $\phi_0(T)$ under the as-

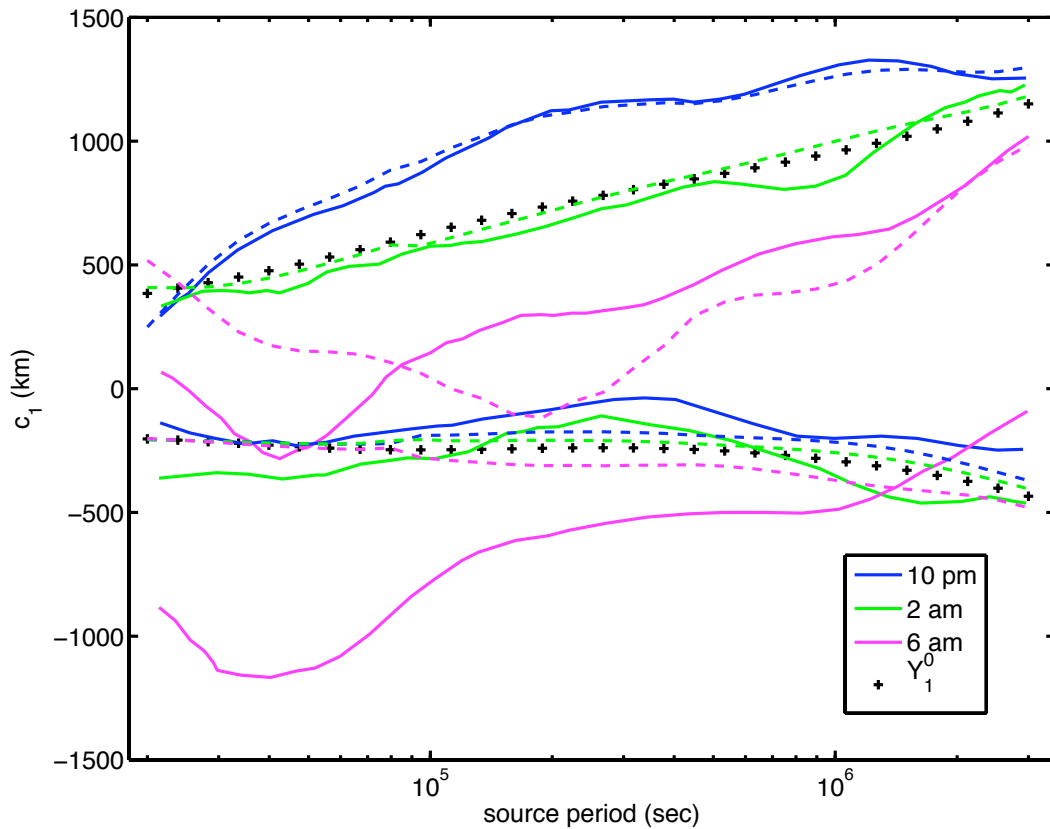


Figure 3.13: Recreation of Balasis bias with a $\cos \phi_1$ -weighted Y_1^0 primary field and the resulting Y_2^1 contamination in the secondary field. The real (positive) and imaginary (negative) parts of $c_1(T)$ for local time subsets of 10 pm (blue), 2 am (green), and 6 am (pink). The solid curves indicate the empirical bias found by BEM. The dashed curves indicate the synthetic bias produced by our method. The plus signs indicate the response for a pure Y_1^0 field.

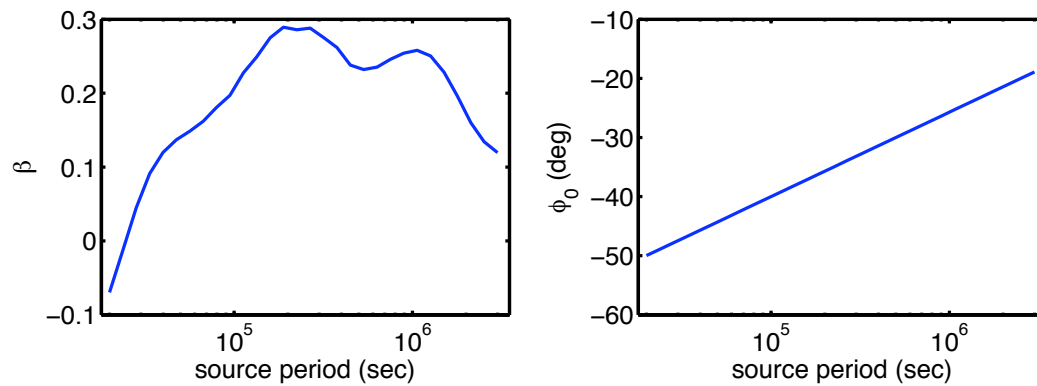


Figure 3.14: Values of $\beta(\omega)$ and $\phi_0(\omega)$ used to create Figure 3.13.

sumption that the bias is caused by coherent $\cos \phi_1$ -weighted Y_1^0 contamination of the primary field and the resulting Y_2^1 contamination of the secondary field. The fit is shown in Figure 3.13, and the $\beta(T)$ and $\phi_0(T)$ estimates used to produce it are shown in Figure 3.14. In this case, the fit to the real part of c_1 is not as good as in the previous case, since it is difficult to fit all three LT subsets simultaneously. We choose to fit the 10 pm and 2 am sectors at the expense of the 6 am sector, in consideration of BEM's attribution of lower accuracy in the dawn sector. The maximum value of β for this case is ~ 0.3 at periods just over 1 day. This corresponds to difference of ~ 100 nT in B_θ on opposite sides of Earth when we assume that $\hat{e}_1^0 = 100$ nT, which is unlikely to be realistic. The modeled bias in the imaginary parts of c_1 is increased when compared to the previous case, but does not reflect the structure of the empirical responses.

3.3 Conclusions

We find that it is possible to recreate the LT bias in empirical c_1 responses found by BEM with the inclusion of time-varying Y_2^1 contamination in the primary and secondary fields in the period range 10^4 – 10^6 seconds. We note that the amount of asymmetry in equatorial field strength that is required to account for the BEM bias reaches nearly 50% at some periods, a fact which contradicts the findings of many previous researchers, who found that the ring current could be adequately modeled at most time scales as a Y_1^0 spherical harmonic (e.g. Banks, 1969; Schultz and Larsen, 1987; Martinec and Velimský, 2009). We attribute most of the bias in these c_1 estimates to the geometry of the Y_2^1 fields, which is shown to have a much larger effect than the difference between Q_2 and Q_1 .

We find it unlikely that the BEM bias is caused by contamination of primary field with the simpler form described by a $\cos \phi_1$ -weighting of a Y_1^0 external field since the resulting modeled bias is a poor fit to the empirical bias, and the required amount of asymmetry in equatorial field strength would exceed 100% at some periods. The reduced effectiveness of this type of field in creating bias in response functions is consistent with the fact that the external field geometry is very similar

to that of a uniform field, and the fact that its Q -value is much lower than Q_2 for any given source period.

This study does not rule out other causes of the BEM bias, including higher degree and order spherical harmonic structure in the primary fields, but argues that a greater understanding of the structure of the primary field will be necessary for accurate interpretation of satellite data. It is hoped that multi-satellite missions such as SWARM will help in this regard. If such structure is found, this study provides a method by which to estimate the effect of Earth rotation on satellite c_1 responses without the approximations required by BEM's analysis. The effect of Earth rotation on any spherical harmonic structure of order $m = 1$ can be estimated with very little modification to this method, and the extension to $m > 1$ should be straightforward.

We also conclude that the presence of non- Y_1^0 structure in the fields makes the use of scalar anomalies of questionable value for satellite induction studies. The bias in response functions calculated from scalar satellite data is drastically increased compared to those estimated from vector data. Although it may be possible to draw conclusions about the structure of the fields from the differences in these estimates, we have not done so in this study.

3.4 Acknowledgments

This work was supported by NASA Headquarters under the NASA Earth and Space Science Fellowship Program - Grant NNX07AQ94H. The author would also like to thank Cathy Constable for guidance and collaboration on this work, and Bob Parker and Steven Constable for useful discussions.

References

- Balasis, G., and Egbert, G., 2006: Empirical orthogonal function analysis of magnetic observatory data: Further evidence for non-axisymmetric magnetospheric sources for satellite induction studies. *Geophys. Res. Lett.*, **33**(11), 11311.
- Balasis, G., Egbert, G., and Maus, S., 2004: Local time effects in satellite estimates of electromagnetic induction transfer functions. *Geophys. Res. Lett.*, **31**, 16610.
- Banks, R., 1969: Geomagnetic variations and the electrical conductivity of the upper mantle. *Geophys. J. R. Astron. Soc.*, **17**(5), 457–487.
- Campbell, W., 1997: *Introduction to geomagnetic fields*. Cambridge Univ Pr.
- Chapman, S., 1919: The solar and lunar diurnal variations of terrestrial magnetism. *Phil. Trans. R. Soc. Lond., A*, **218**, 1–118.
- Constable, S., 1993: Constraints on mantle electrical conductivity from field and laboratory measurements. *J. Geomagn. Geoelectr.*, **45**(9), 7070–728.
- Constable, S., 2007: Geomagnetism. In *Treatise on Geophysics*, editor G. Schubert, 237–276. Elsevier.
- Constable, S., and Constable, C., 2004: Observing geomagnetic induction in magnetic satellite measurements and associated implications for mantle conductivity. *Geochemistry Geophysics Geosystems*, **5**(1), Q01006.
- Daglis, I., and Kozyra, J., 2002: Outstanding issues of ring current dynamics. *J. Atmos. Sol. Terr. Phys.*, **64**(2), 253–264.
- Kuvshinov, A., and Olsen, N., 2006: A global model of mantle conductivity derived from 5 years of champ, ørsted, and sac-c magnetic data. *Geophys. Res. Lett.*, **33**(18), 18301.
- Lahiri, B., and Price, A., 1939: Electromagnetic induction in non-uniform conductors, and the determination of the conductivity of the earth from terrestrial magnetic variations. *Phil. Trans. R. Soc. Lond., A*, **237**(784), 509–540.

- Martinec, Z., and Velínský, J., 2009: The adjoint sensitivity method of global electromagnetic induction for champ magnetic data. *Geophys. J Int.*, **179**(3), 1372–1396.
- Olsen, N., Lühr, H., Sabaka, T., Manda, M., Rother, M., Tøffner-Clausen, L., and Choi, S., 2006: Chaos model of the earth's magnetic field derived from champ, ørsted, and sac-c magnetic satellite data. *Geophys. J Int.*, **166**(1), 67–75.
- Olsen, N., Manda, M., Sabaka, T., and Tøffner-Clausen, L., 2009: Chaos-2 - a geomagnetic field model derived from one decade of continuous satellite data. *Geophys. J Int.*, **179**(3), 1477–1487.
- Schultz, A., and Larsen, J., 1987: On the electrical conductivity of the mid-mantle: I. calculation of equivalent scalar magnetotelluric response functions. *Geophys. J. R. Astr. Soc.*, **88**(3), 733–761.
- Weidelt, P., 1972: The inverse problem of geomagnetic induction. *J. Geophys.*, **38**, 257–289.

Chapter 4

FlexPDE Simulations For Comparison Of Global Induction Codes

Abstract We present FlexPDE solutions to simulations of global electromagnetic induction in four models of spherical conductors with uniform primary fields. The models presented include radially conductive concentric spheres with different surface conductances in (1) Northern and Southern hemispheres, and (2) Eastern and Western hemispheres, (3) eccentrically nested spheres of different conductivity, and (4) radially conductive concentric spheres with Earth-like surface conductance map. The results for the first two models are compared with those of two other researchers, and the results of the others are compared with analytic solutions for identical or illustratively similar problems. The FlexPDE results show good agreement with the other solutions, with some differences near coastlines.

4.1 Introduction

The authors of several codes designed to simulate global geomagnetic induction have agreed to collaborate on a project comparing simulation results for six different spherical induction models. The goal of this project is to determine the relative strengths and weaknesses of these codes with respect to accuracy, run-

time, and applicability to specific problem types. In this paper, I present results for four of the proposed models as calculated by FlexPDE finite-element modeling software.

Each model consists of a conductive sphere with radius 6371 km surrounded by infinitely large and perfectly insulating vacuum (approximated in the FlexPDE solutions by an insulating sphere extending to 10 times the radius of the conducting sphere), and is excited by a Y_1^0 external field at periods of 6 hours, 1 day, 4 days, and 16 days. All simulations are calculated in the geomagnetic (GM) coordinate system. The external field is aligned parallel to the GM pole (which coincides with the cartesian z -axis in FlexPDE model space), and has an external dipole coefficient of 100 nT, meaning that the field at the northern GM pole has only a radial component with a value of -100 nT. All FlexPDE calculations are performed in the frequency domain, using the technique described in Chapter 2, except as noted. The finite-element mesh is composed of straight line segments, measurement points at the conductor/vacuum interface (CVI) may fall slightly to one side or the other of this surface. Since some of the models include an infinitely thin surface conductance map which can produce a field discontinuity in conjunction with a boundary condition at the CVI, this can result in large discontinuities in field profiles measured directly on the CVI. For this reason, all of the FlexPDE solutions in this chapter are given at an altitude of 100 m in order to avoid these discontinuities. The FlexPDE solutions are provided with no smoothing or additional processing.

To date, the other participants in this project who have produced solutions to some of the models are Alexei Kuvshinov, using the integral equation method (Kuvshinov *et al.*, 2002a), and Jakub Velimský, using time-domain spectral methods (Velimský and Martinec, 2005), both of whom have provided solutions to Models 1 and 2. For details about these methods see Chapter 1. Thus far, only the FlexPDE solutions have been generated for Models 3 and 6, while Models 4 and 5 have not yet been specified in enough detail for solutions to be calculated. Other potential participants in this project include Chet Weiss – using triangular finite differences (Weiss, 2010), Mark Everett – using hand-coded FEM (Everett

Table 4.1: Electrical conductivities used in Models 1 and 2.

Depth (km)	σ (S/m)
0–100	0.0001
100–400	0.01
400–650	0.1
650–6371	2

Table 4.2: Surface conductance used in Model 1.

Hemisphere	Colatitude($^{\circ}$)	Longitude ($^{\circ}$)	τ (S)
North	0–90	0–360	20,000
South	90–180	0–360	20

and Schultz, 1996), and Makoto Uyeshima – using staggered grids (Uyeshima and Schultz, 2000).

4.2 Model 1: North/South Hemispheres

In this model, the conductivity, σ , is radially varying, with values as described in Table 4.1. These values are not exactly Earthlike, but are known to adequately reproduce Earth’s response to Dst and Sq fields (Kuvshinov *et al.*, 1999). One of the most obvious deviations from realistic Earth values is the absence in the model of a highly conductive (roughly 5×10^5 S/m (Jeanloz, 1990)) core. At 2 S/m, the innermost layer is conductive enough that, at the periods of investigation, the magnetic field is negligible at the depth of the core, and its absence does not affect the result of the calculation.

In addition, an infinitely thin spherical shell describing the surface conductance τ is present at the CVI. The conductances are separately constant, but differ by 3 orders of magnitude between the northern and southern hemispheres, as described in Table 4.2. The shell boundary is like a coastline, but the ocean conductance is much larger than the average value of Earth’s oceans in order to provide a larger ocean/continent contrast with which to test the codes.

In this model, the pathways of electric current are everywhere purely az-

imuthal, and never encounter gradients or discontinuities in σ or τ . Thus this problem is a limited 3D problem, as described in Chapter 2, and is amenable to solution in a 2D model space. Nonetheless, all results presented for this model refer to solutions calculated in a full 3D model space, under the assumption that both the electric scalar potential V , and the z -component of the magnetic vector potential A_z are both identically zero.

The fact that the current pathways are azimuthal and homogeneously conductive also implies that it is not necessary to solve for the scalar current function ψ , the purpose of which is to determine the direction and magnitude of the surface current \mathbf{j} at the CVI under the assumption that \mathbf{j} is divergenceless and the surface layer is electrically isolated from the underlying mantle. These qualities apply intrinsically to any current caused by purely azimuthal electric field following homogeneous pathways, including those at the CVI. Thus \mathbf{j} can be calculated directly from the total scalar potential \mathbf{A} via Ohm's law:

$$\mathbf{j} = \tau \mathbf{E}, \quad (4.1)$$

which reduces in this case to

$$\mathbf{j} = -i\omega \mathbf{A}. \quad (4.2)$$

The resulting discontinuity in B_θ is imposed in the simulations by enforcing the following boundary condition at the CVI:

$$\partial_r \mathbf{A}^+ - \partial_r \mathbf{A}^- = i\omega \mu_0 \tau \mathbf{A}. \quad (4.3)$$

This technique has the effect of achieving higher accuracy with shorter runtimes than we would get by including ψ as a solution variable.

The FlexPDE solutions of the total magnetic field as a function of colatitude are shown in Figure 4.1, along with the Kuvshinov and Velimský solutions. The radial and polar components of the induction field \mathbf{B} are shown for all periods as functions of colatitude. (The azimuthal component is identically zero in Model 1.) All of the solutions show good agreement, with the Kuvshinov and FlexPDE solutions being nearly identical. The Velimský solution shows a very small amount of both systematic bias and anomalous short wavelength structure compared to

Table 4.3: Runtimes for Model 1.

Period	Runtime (minutes)
16 days	36
4 days	33
1 day	55
6 hours	105

the other two. Both of these effects are likely caused by the representation of the solution in terms of a truncated series of spherical harmonics. It should also be noted that the Velimský solutions have been smoothed in post-processing.

Runtimes for the FlexPDE solution are given in Table 4.3. These runtimes are highly dependent on the hardware employed, and on user-controlled specifications in the problem script, including but not limited to: requested error tolerance, initial mesh density, number of simultaneous processor threads, the number of conjugate gradient iterations performed before AMR is applied, and whether the mesh is reused from one period to the next or constructed from scratch each time. All of the FlexPDE solutions presented here are calculated with 4 simultaneous CPU threads at an error tolerance of .001, which roughly corresponds to an absolute accuracy of about 1 nT (see Section 2.2.2 for details). The computation mesh is passed from one period to the next and the periods are run in order from long to short, meaning the initial mesh construction is included in the runtimes for the periods of 16 days.

4.3 Model 2: East/West Hemispheres

The radially varying conductivity in Model 2 is identical to that in Model 1, as given in Table 4.1. The surface conductance in Model 2 is very similar to that in Model 1, except that the conductance layer is separated into Eastern and Western hemispheres, instead of Northern and Southern hemispheres. This is described quantitatively in Table 4.4.

This is a fully 3D model (as described in Chapter 2), where neither the volume current nor the surface current is expected to be purely azimuthal. Thus

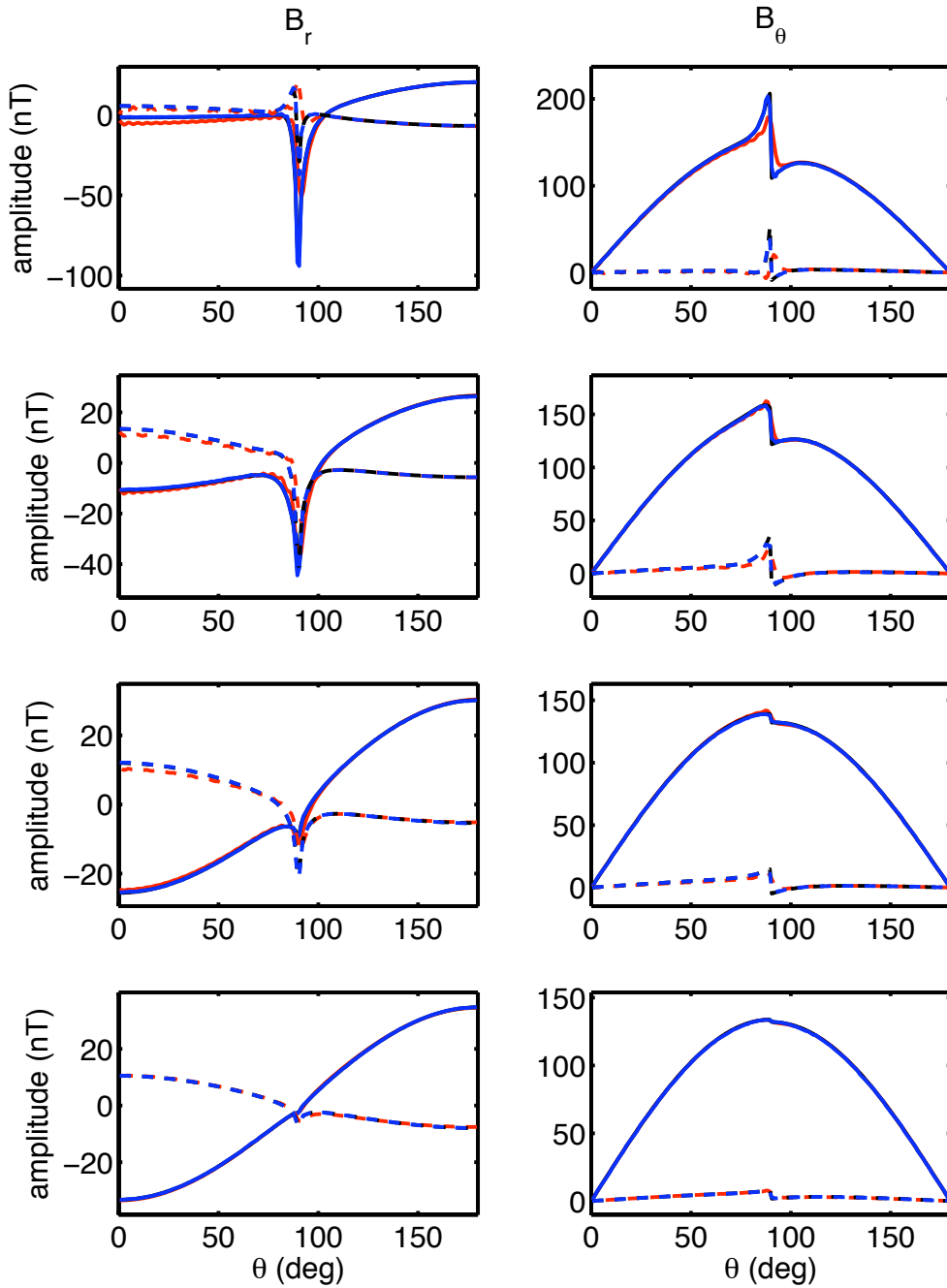


Figure 4.1: Meridional profiles of B_r (left column) and B_θ (right column) for Model 1 as calculated by the author with FlexPDE (blue), by Kuvshinov with integral equations (black), and by Velimsky with time-domain spectral methods (red) for each period considered. The solid curves are the real part and the dashed curves indicate the imaginary part. Plots are shown for periods of 6 hours (first row), 1 day (second row), 4 days (third row), and 16 days (fourth row).

Table 4.4: Surface conductance used in Model 2.

Hemisphere	Colatitude(°)	Longitude (°)	τ (S)
East	0–180	-90–90	20
West	0–180	90–270	20,000

Table 4.5: Runtimes for Model 2.

Period	Runtime (hours)
16 days	10.5
4 days	11
1 day	30
6 hours	86

we must find solutions for five complex variables: three components of the magnetic vector potential \mathbf{A} , the electric scalar potential V , and the current function ψ . This is more than double the number of variables compared to Model 1, which increases runtimes considerably. These runtimes are given in Table 4.5.

Meridional profiles of the FlexPDE solutions are shown in Figures 4.2 – 4.16, alongside the integral equation solutions and the time-domain spectral solutions. Unlike those for Model 1, the solutions for Model 2 are dependent on longitude, thus they are shown as meridional profiles for four different longitudes (one apiece near the center of each hemisphere, and one apiece near each coastline) in Figures 4.2 – 4.13, and as azimuthal profiles at a single colatitude in Figures 4.14 – 4.16.

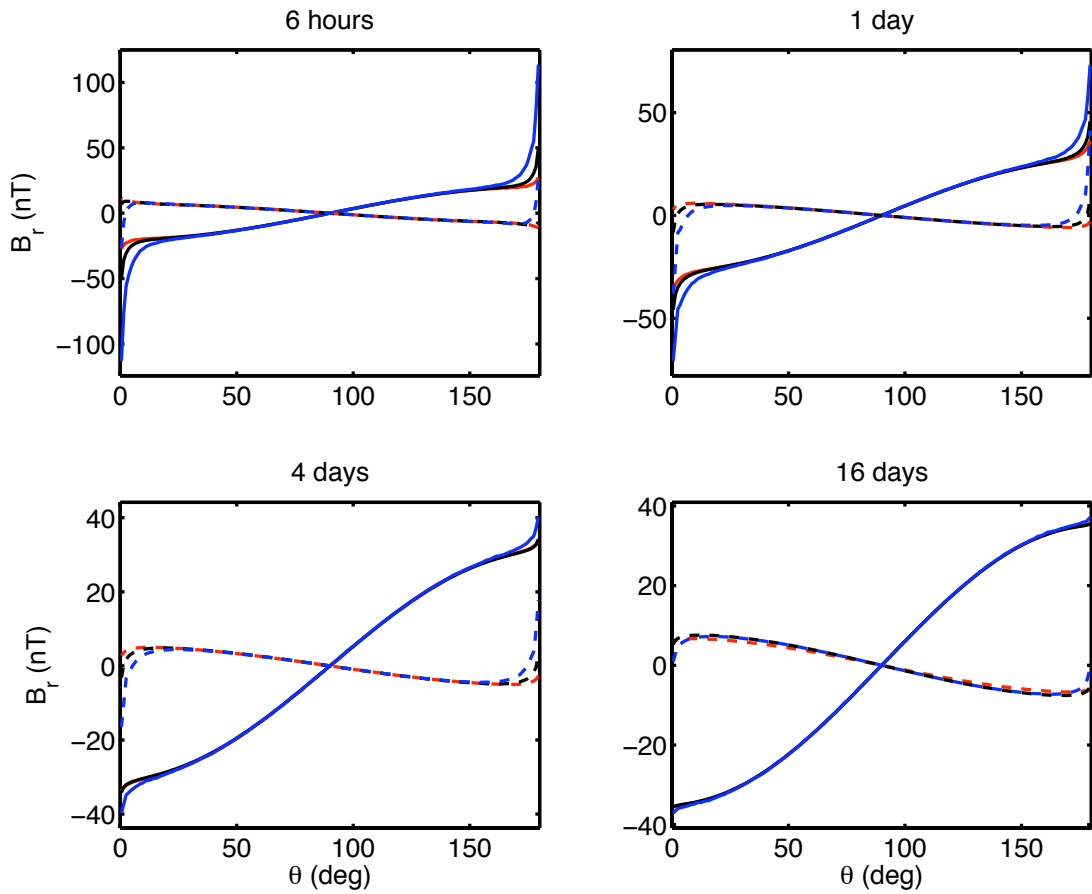


Figure 4.2: Meridional profiles of the real (solid) and imaginary (dashed) parts of B_r for longitude $\phi = 0.5^\circ$ in Model 2 for periods of 6 hours, 1 day, 4 days, and 16 days as calculated by the author with FlexPDE (blue), by Kuvshinov with integral equations (black), and by Velímský with time-domain spectral methods (red).

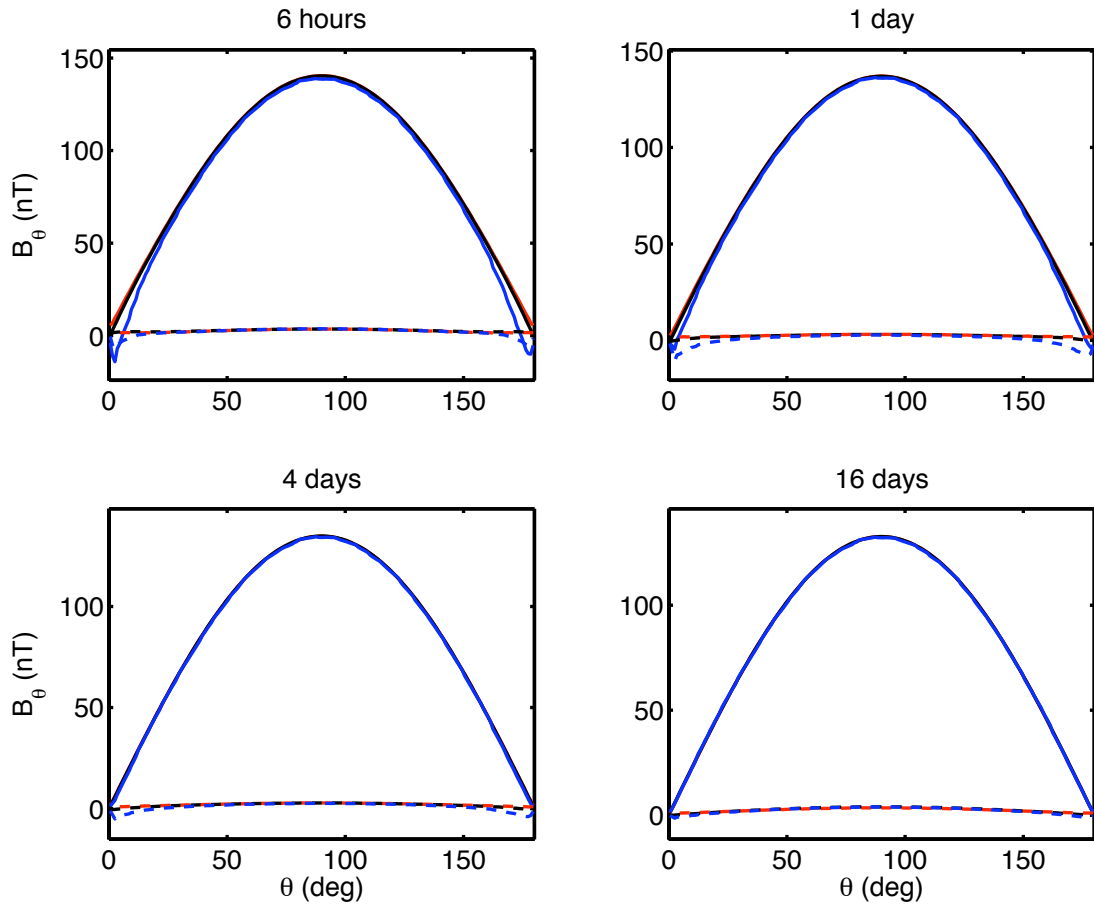


Figure 4.3: Meridional profiles of the real (solid) and imaginary (dashed) parts of B_θ for longitude $\phi = 0.5^\circ$ in Model 2 for periods of 6 hours, 1 day, 4 days, and 16 days as calculated by the author with FlexPDE (blue), by Kuvshinov with integral equations (black), and by Velímský with time-domain spectral methods (red).

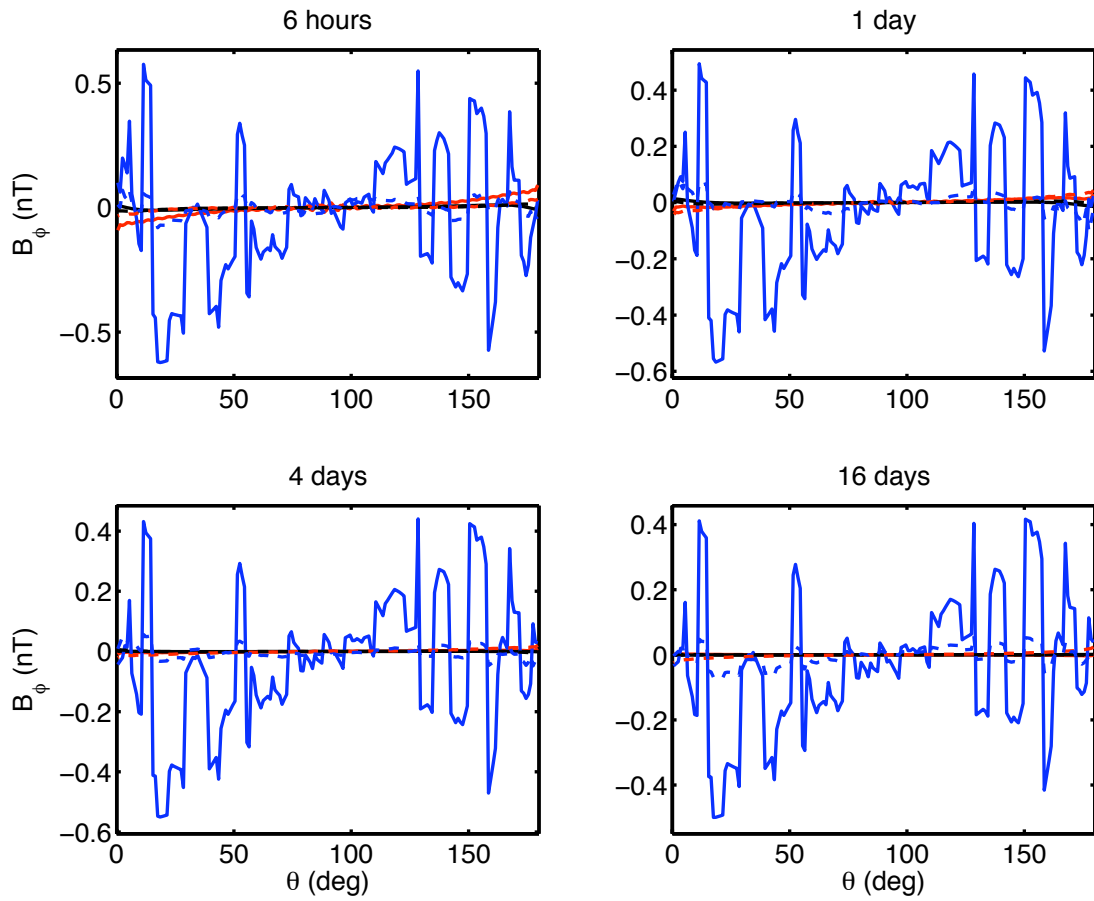


Figure 4.4: Meridional profiles of the real (solid) and imaginary (dashed) parts of B_ϕ for longitude $\phi = 0.5^\circ$ in Model 2 for periods of 6 hours, 1 day, 4 days, and 16 days as calculated by the author with FlexPDE (blue), by Kuvshinov with integral equations (black), and by Velímský with time-domain spectral methods (red).

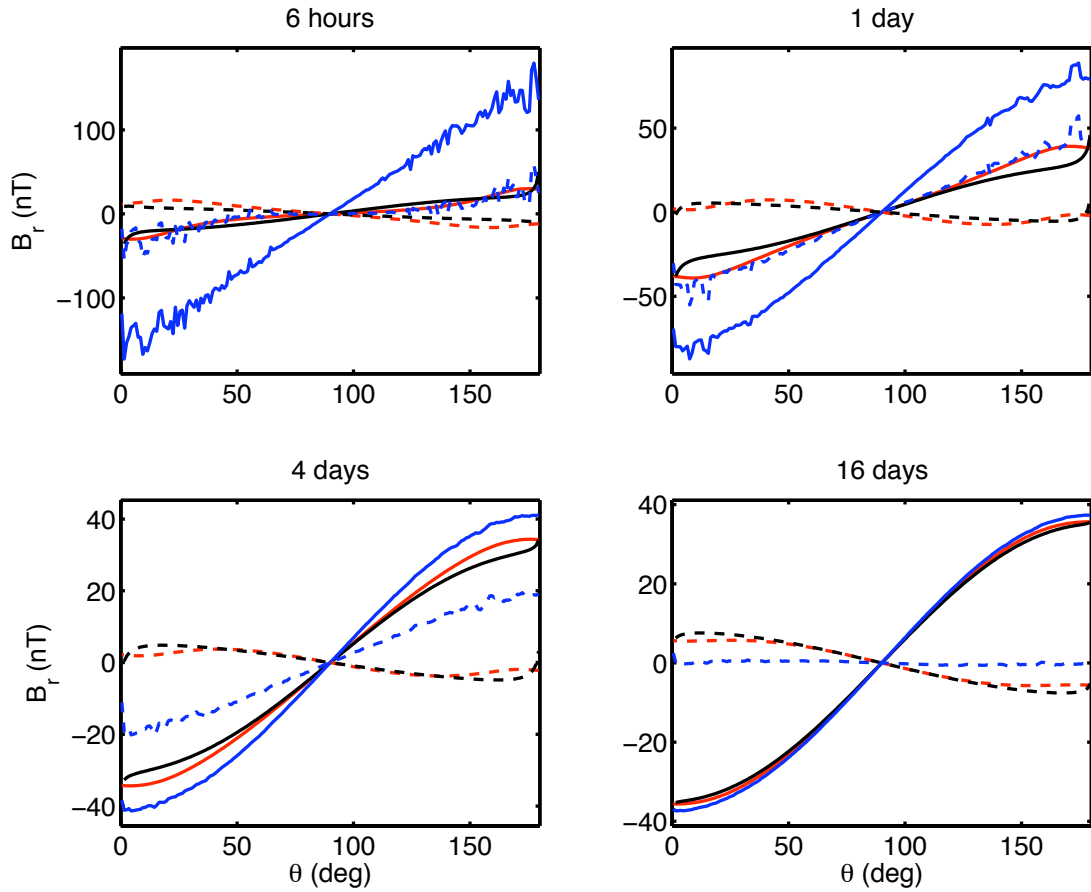


Figure 4.5: Meridional profiles of the real (solid) and imaginary (dashed) parts of B_r for longitude $\phi = 90.5^\circ$ in Model 2 for periods of 6 hours, 1 day, 4 days, and 16 days as calculated by the author with FlexPDE (blue), by Kuvshinov with integral equations (black), and by Velímský with time-domain spectral methods (red).

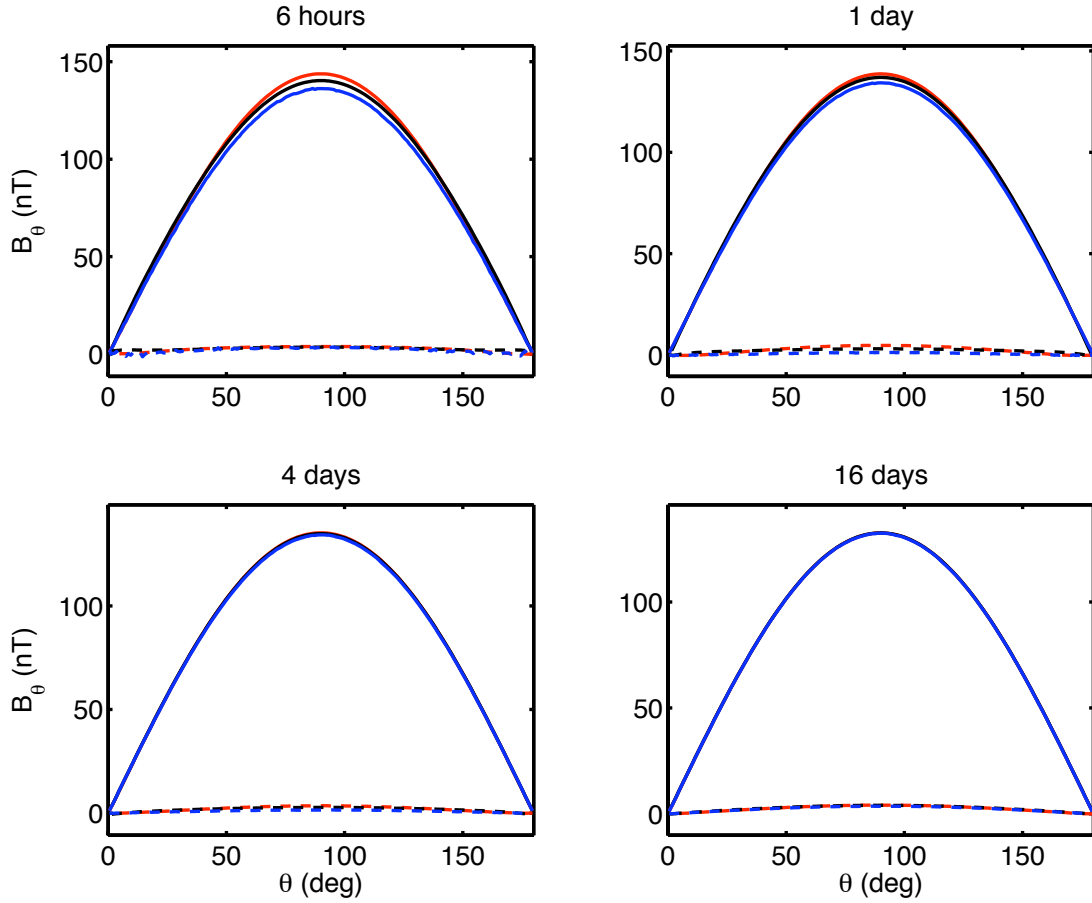


Figure 4.6: Meridional profiles of the real (solid) and imaginary (dashed) parts of B_θ for longitude $\phi = 90.5^\circ$ in Model 2 for periods of 6 hours, 1 day, 4 days, and 16 days as calculated by the author with FlexPDE (blue), by Kuvshinov with integral equations (black), and by Velímský with time-domain spectral methods (red).

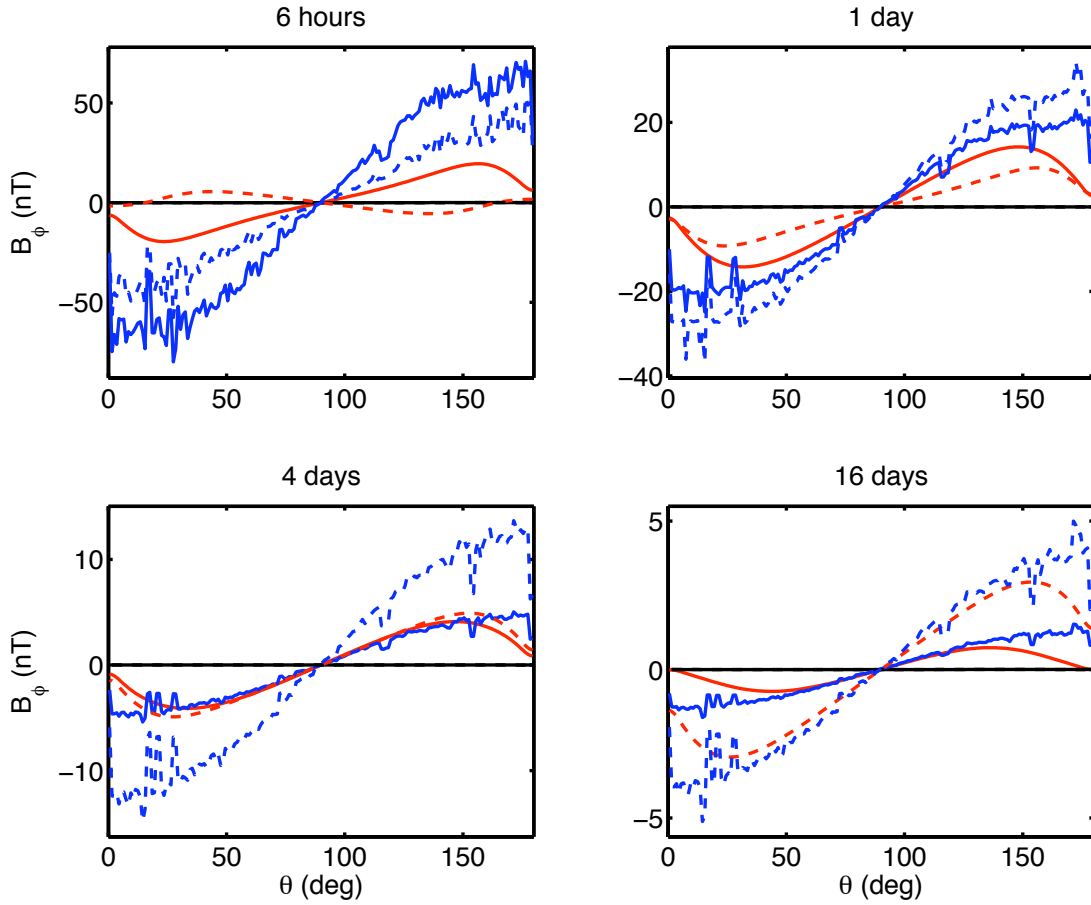


Figure 4.7: Meridional profiles of the real (solid) and imaginary (dashed) parts of B_ϕ for longitude $\phi = 90.5^\circ$ in Model 2 for periods of 6 hours, 1 day, 4 days, and 16 days as calculated by the author with FlexPDE (blue), by Kuvshinov with integral equations (black), and by Velímský with time-domain spectral methods (red).

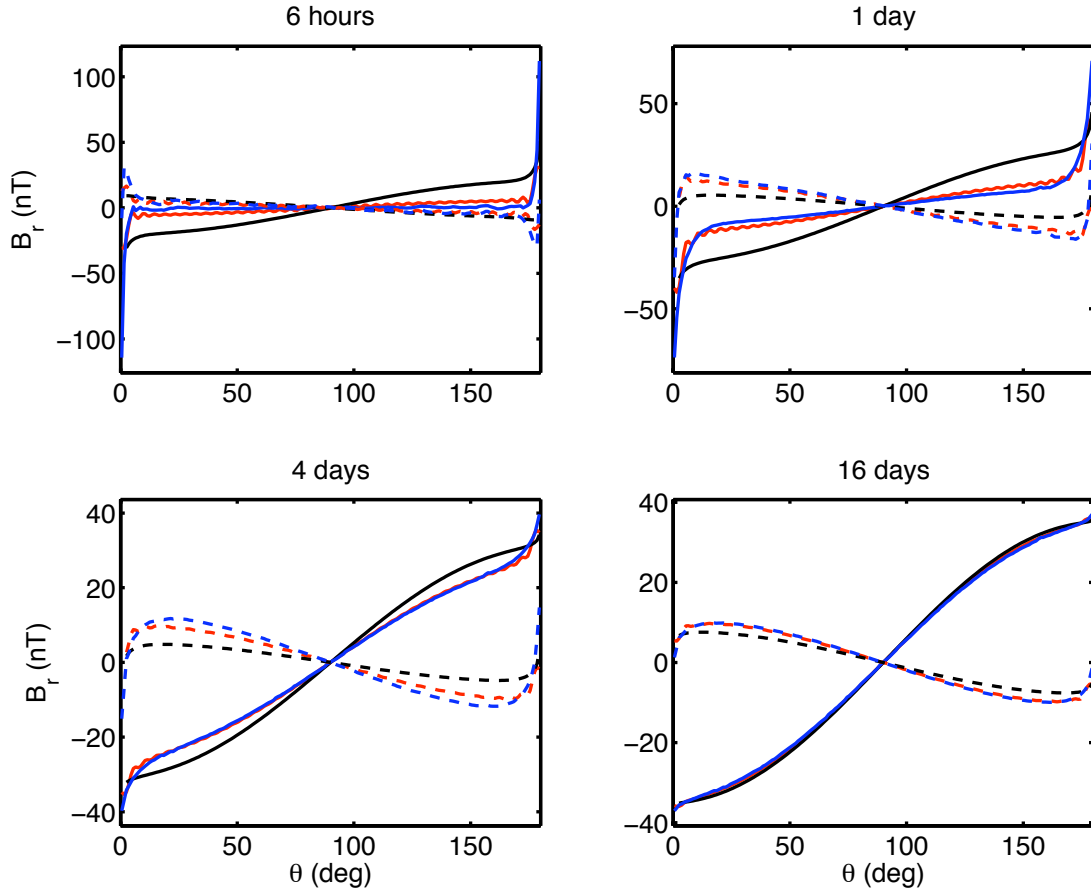


Figure 4.8: Meridional profiles of the real (solid) and imaginary (dashed) parts of B_r for longitude $\phi = 180.5^\circ$ in Model 2 for periods of 6 hours, 1 day, 4 days, and 16 days as calculated by the author with FlexPDE (blue), by Kuvshinov with integral equations (black), and by Velimský with time-domain spectral methods (red).

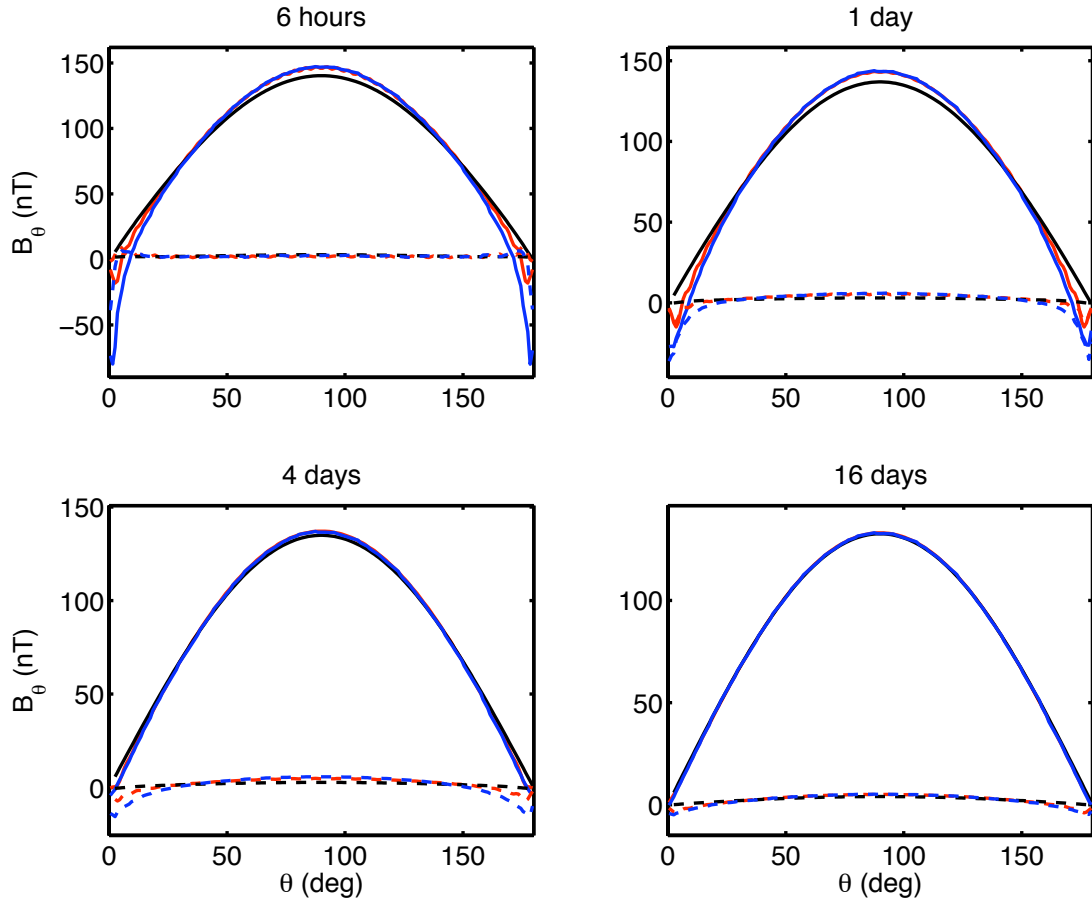


Figure 4.9: Meridional profiles of the real (solid) and imaginary (dashed) parts of B_θ for longitude $\phi = 180.5^\circ$ in Model 2 for periods of 6 hours, 1 day, 4 days, and 16 days as calculated by the author with FlexPDE (blue), by Kuvshinov with integral equations (black), and by Velímský with time-domain spectral methods (red).

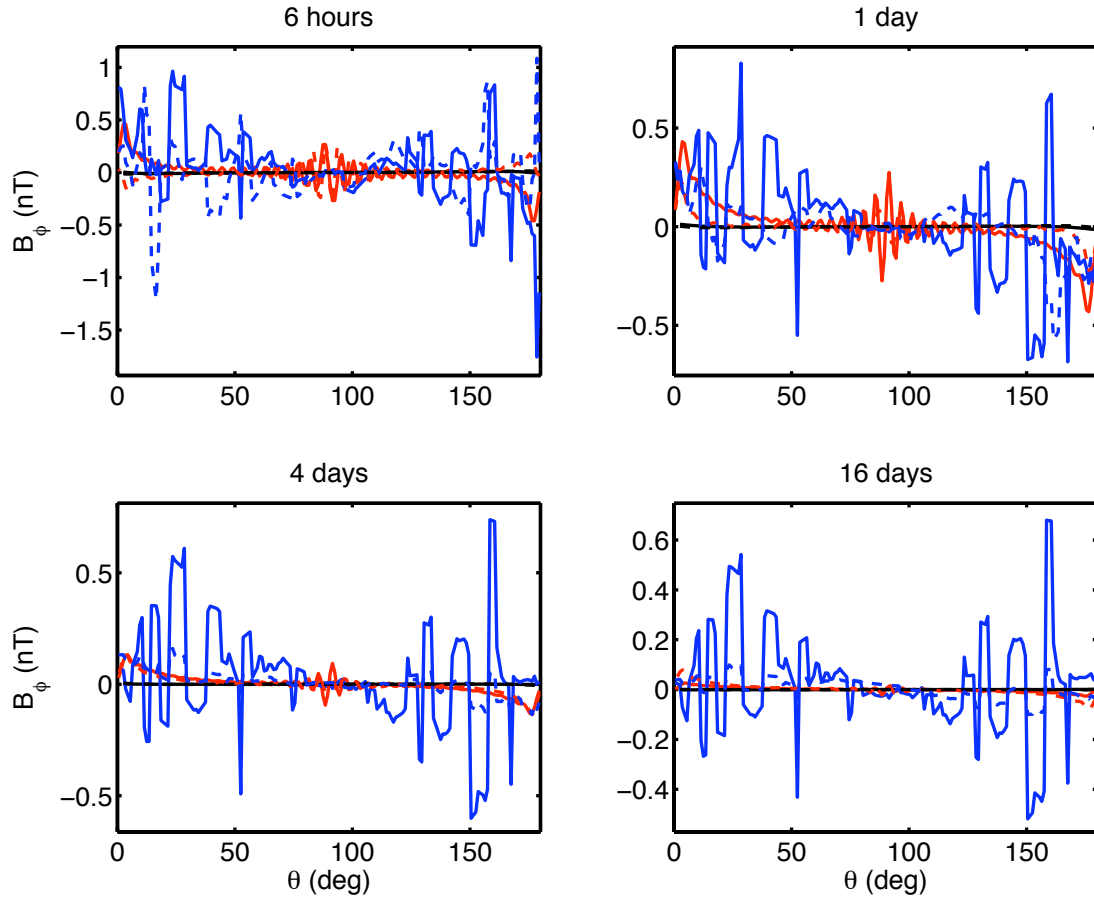


Figure 4.10: Meridional profiles of the real (solid) and imaginary (dashed) parts of B_ϕ for longitude $\phi = 180.5^\circ$ in Model 2 for periods of 6 hours, 1 day, 4 days, and 16 days as calculated by the author with FlexPDE (blue), by Kuvshinov with integral equations (black), and by Velímský with time-domain spectral methods (red).

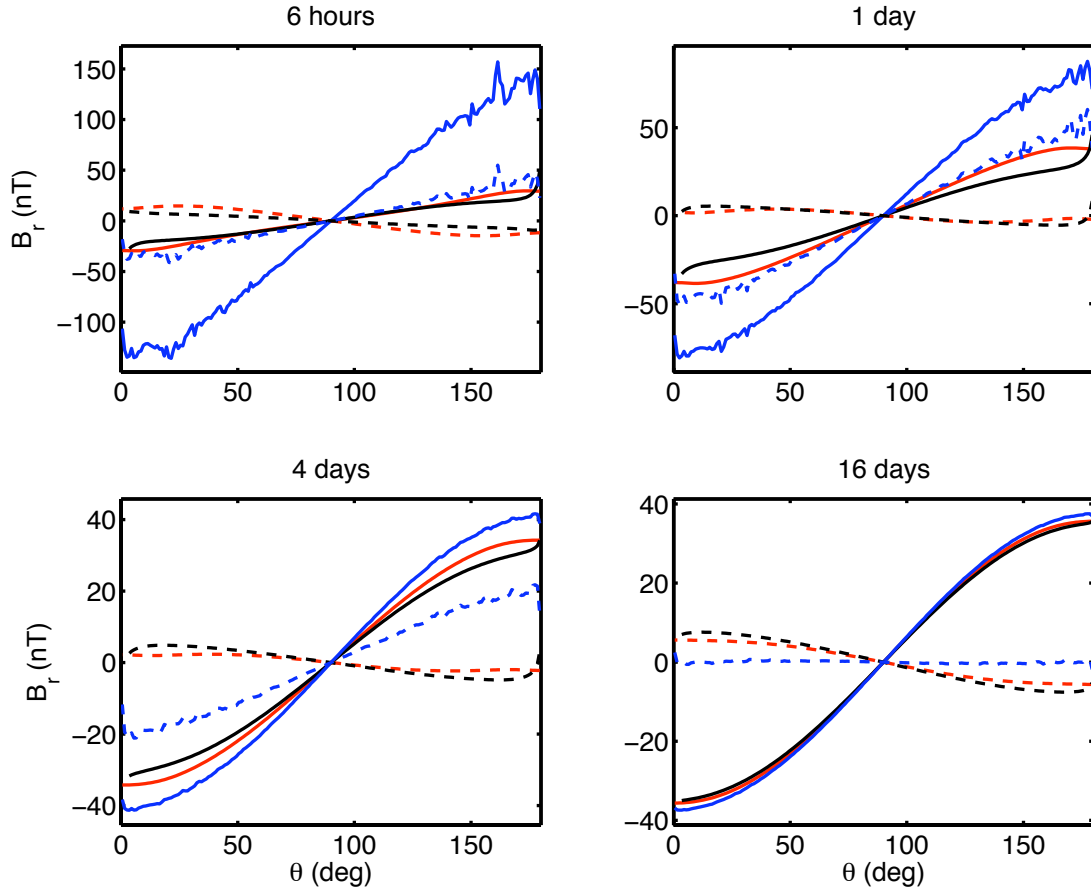


Figure 4.11: Meridional profiles of the real (solid) and imaginary (dashed) parts of B_r for longitude $\phi = 270.5^\circ$ in Model 2 for periods of 6 hours, 1 day, 4 days, and 16 days as calculated by the author with FlexPDE (blue), by Kuvshinov with integral equations (black), and by Velímský with time-domain spectral methods (red).

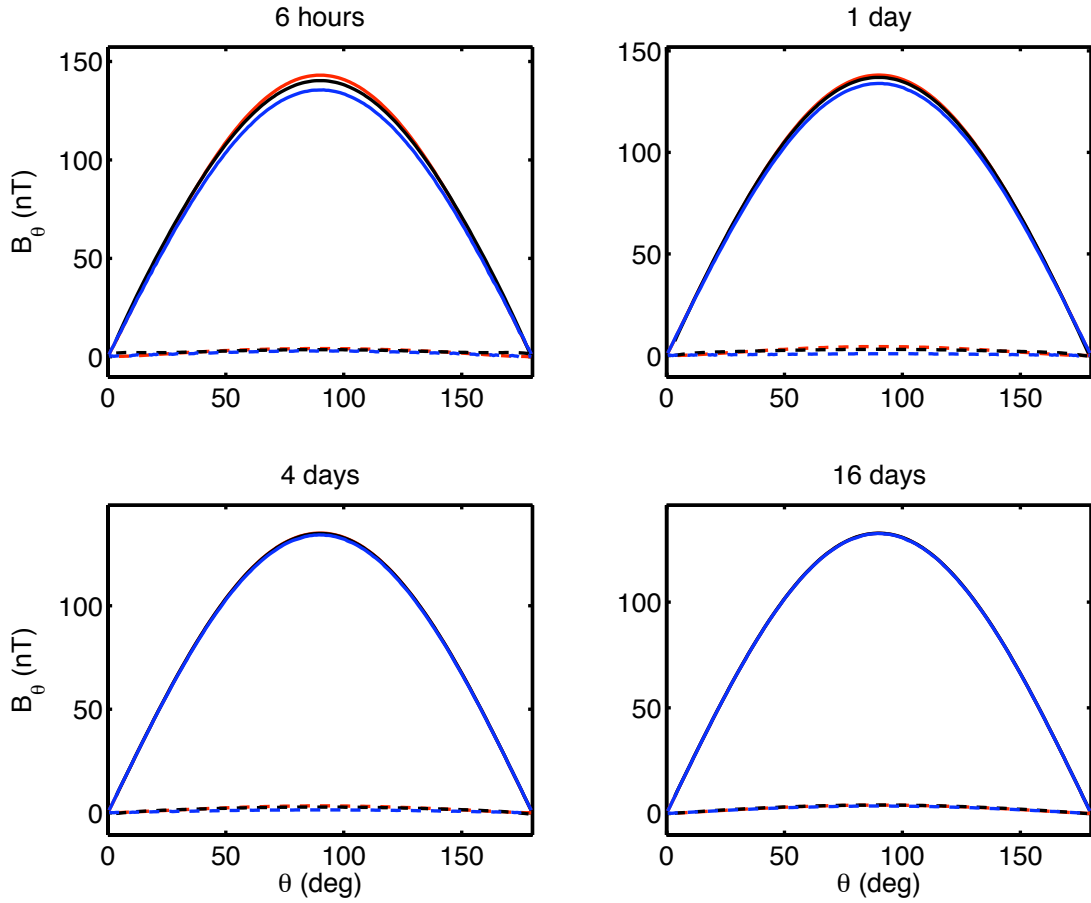


Figure 4.12: Meridional profiles of the real (solid) and imaginary (dashed) parts of B_θ for longitude $\phi = 270.5^\circ$ in Model 2 for periods of 6 hours, 1 day, 4 days, and 16 days as calculated by the author with FlexPDE (blue), by Kuvshinov with integral equations (black), and by Velímský with time-domain spectral methods (red).

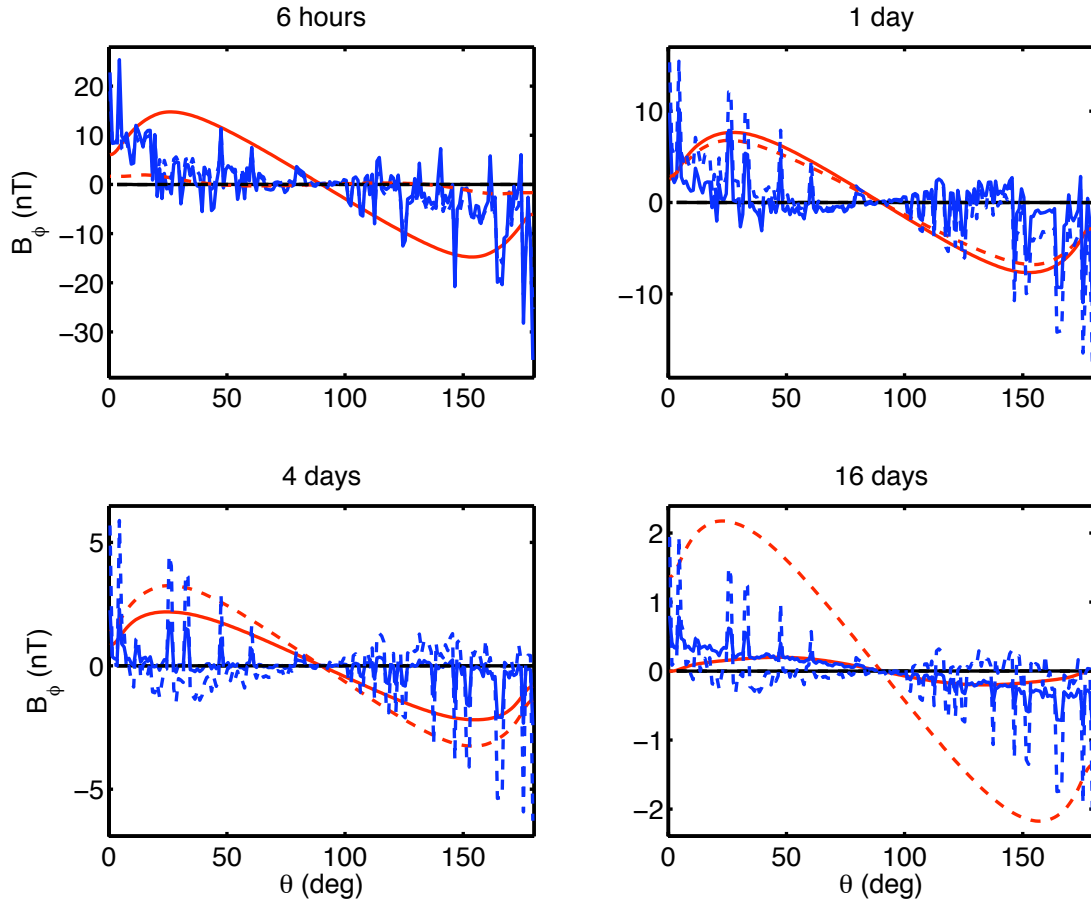


Figure 4.13: Meridional profiles of the real (solid) and imaginary (dashed) parts of B_ϕ for longitude $\phi = 270.5^\circ$ in Model 2 for periods of 6 hours, 1 day, 4 days, and 16 days as calculated by the author with FlexPDE (blue), by Kuvshinov with integral equations (black), and by Velímský with time-domain spectral methods (red).

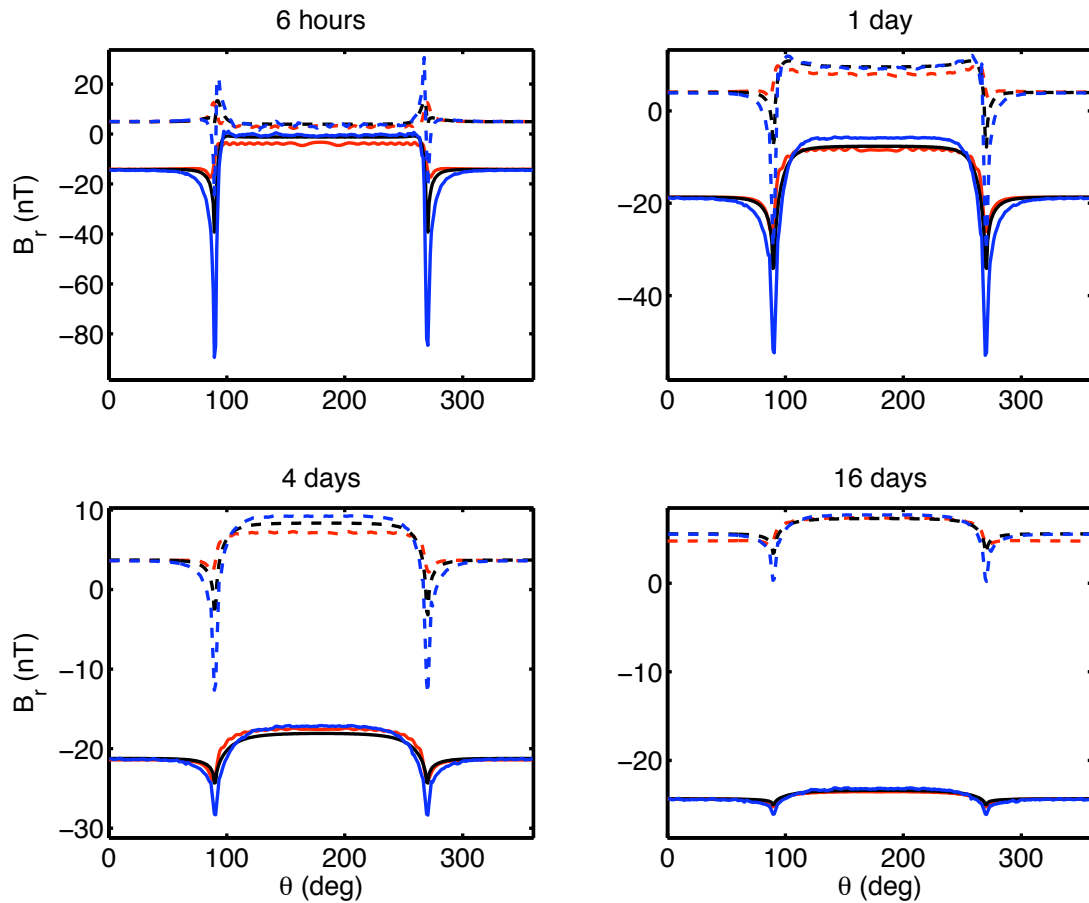


Figure 4.14: Azimuthal profiles of the real (solid) and imaginary (dashed) parts of B_r for longitude $\theta = 45.5^\circ$ in Model 2 for periods of 6 hours, 1 day, 4 days, and 16 days as calculated by the author with FlexPDE (blue), by Kuvshinov with integral equations (black), and by Velímský with time-domain spectral methods (red).

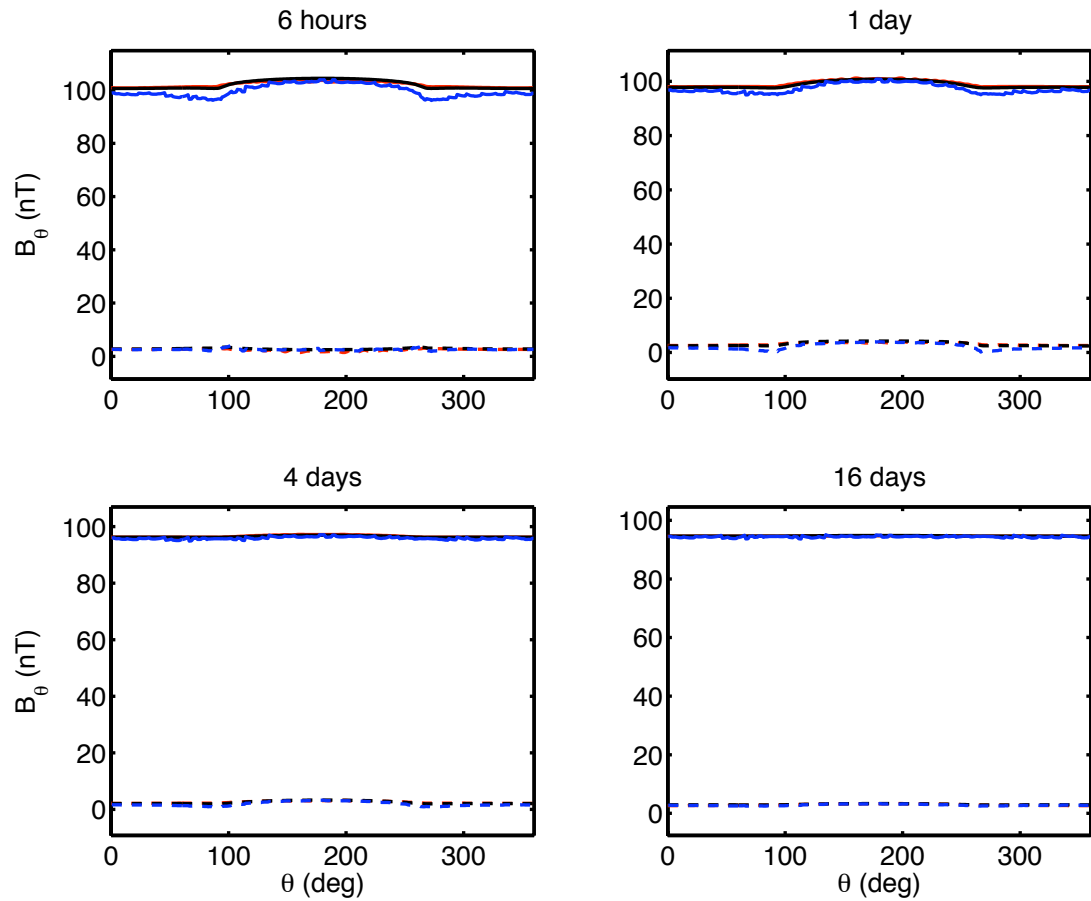


Figure 4.15: Meridional profiles of the real (solid) and imaginary (dashed) parts of B_θ for longitude $\theta = 45.5^\circ$ in Model 2 for periods of 6 hours, 1 day, 4 days, and 16 days as calculated by the author with FlexPDE (blue), by Kuvshinov with integral equations (black), and by Velímský with time-domain spectral methods (red).

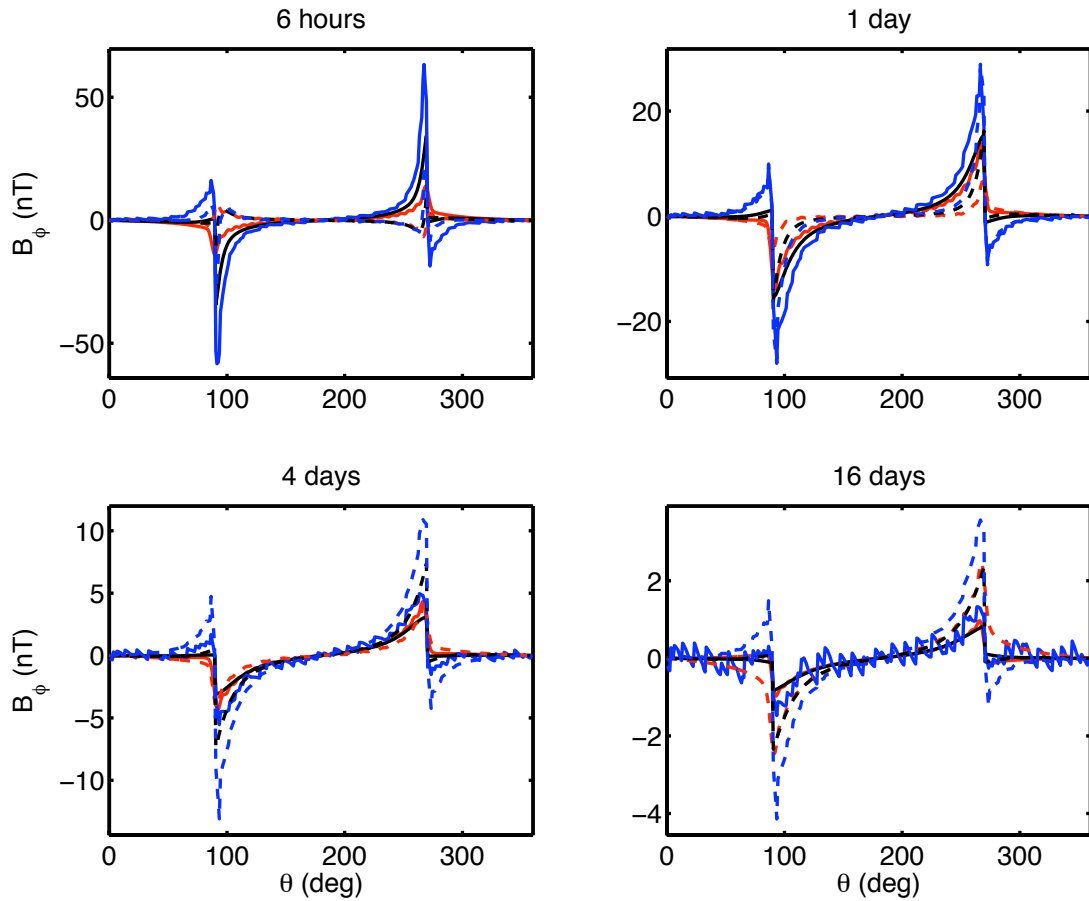


Figure 4.16: Meridional profiles of the real (solid) and imaginary (dashed) parts of B_ϕ for longitude $\theta = 45.5^\circ$ in Model 2 for periods of 6 hours, 1 day, 4 days, and 16 days as calculated by the author with FlexPDE (blue), by Kuvshinov with integral equations (black), and by Velímský with time-domain spectral methods (red).

The FlexPDE solutions exhibit both systematic bias and short-wavelength variation with respect to the other two solutions. Both of these types of disagreement decrease with distance from the coastlines and with increased period, but for different reasons in each case. The short-wavelength variations are simply noise in the solutions, and are an artifact of the calculation technique, which iterates until the estimated error in the solution falls below a certain threshold. This noise can be reduced by decreasing the error tolerance and/or increasing the mesh density, both of which lead to increased runtimes. At longer periods, the inductive signal penetrates deeper into the mantle, and the fields at the surface are more reflective of the azimuthally symmetric structure of the mantle, while shorter periods focus the induced current at shallower depths and allow the discontinuities of the surface conductance to play a greater role in the solutions. Short-wavelength structure in the fields is most evident at the coastlines, which means the noise in the solutions will be more evident there. The component with the greatest noise is B_ϕ , for which the mid-hemisphere solutions have the lowest signal-to-noise ratio simply because the value of the component is very close to zero there. These errors are large compared to the signal itself, but remain well below 1 nT in magnitude. The noise in the coastal estimates of B_ϕ are much larger however and reflect the fact that B_ϕ appears to be the most difficult component for FlexPDE to resolve accurately. The integral equation method and the time-domain spectral method are less susceptible to this type of noise: the former because it only calculates the field at Earth's surface instead of everywhere within the model, which provides a more focused use of computational resources, and the latter because it solves for individual spherical harmonics, which are smooth functions to begin with, and then adds additional smoothing in post-processing.

The systematic differences among the three solutions are most evident in the meridional profiles of B_ϕ , all of which vary significantly, especially near the coastlines (including near the poles). These differences likely reflect the slight variations in the physics being modeled by each method. Specifically, the integral equation technique assumes an infinitely thin surface conductance that has electrical interaction with the underlying mantle (or *bimodal* induction), which allows

for vertical leakage currents between the surface layer and mantle. The FlexPDE method also assumes an infinitely thin surface layer, but does not allow electrical contact with the mantle. This means all surface currents are purely toroidal, and leakage currents are not allowed. The difference between these two methods is most evident near meridional conductance contrasts, where the FlexPDE method will preferentially divert more of the azimuthal current to the north or south (generating the locally increased amplitudes seen in the azimuthal profiles of Figures 4.14–4.16, and the systematic biases in B_r and B_ϕ in the coastal meridional profiles of Figures 4.5, 4.7, 4.11, and 4.13), while bimodal methods will allow some of that current to plunge beneath the surface into the mantle and continue traveling azimuthally. The effect of this difference in our results is more pronounced at shorter periods, as expected (Kuvshinov *et al.*, 1999).

The spectral method of Velínský takes yet another approach and gives the surface layer a finite thickness (10 km in this case) in the computation mesh. This variation arguably produces the most realistic representation of induction in the true Earth, having a surface layer with both finite spatial extent and galvanic contact with the mantle, but this realism is offset by the description of the solution as a truncated and arbitrarily smoothed set of spherical harmonics. The differences among the methods are least important far from the conductivity contrasts, where the fields calculated by all methods closely match those associated with fully 1D conductivities matching the local depth profiles.

4.4 Model 3: Eccentrically Nested Spheres

In this model, the conductor is modeled as a set of two nested conductive spheres. The outer sphere has conductivity $\sigma = 0.01$ S/m, and radius 6371 km. The inner sphere, with $\sigma = 1.0$ S/m and radius 3500 km, is not concentric with the outer sphere. Instead, its center is located at a radius $r = 2500$ km, colatitude $\theta = 40^\circ$, and longitude $\phi = 35^\circ$, in a coordinate system with its origin at the center of the outer sphere.

To date, none of the other participants in the global comparison project

Table 4.6: Runtimes for Model 3.

Period	Runtime (hours)
16 days	3
4 days	3.5
1 day	26
6 hours	76

have provided solutions for this model. However a semi-analytic solution (Martinec, 1998) has been calculated (Velìmský, personal correspondence) with which to compare the FlexPDE solutions. Martinec’s solution is calculated in terms of a series of spherical harmonics, truncated at order 18 for the longer two periods and at order 12 for the shorter two periods. Increasing the number of terms in the series causes the solutions for the two shorter periods to become unstable and produce volatile results, so the series is truncated to prevent this at the cost of reduced spatial resolution.

Model 3 represents a fully 3D problem, but has no surface conductance. Thus FlexPDE must find solutions for four complex variables: V , and the three components of \mathbf{A} . Since there are more variables than in Model 1, but fewer than in Model 2, it is not surprising that the runtimes for Model 3, given in Table 4.6, fall between those of the previous two models.

The FlexPDE solutions are compared to the semi-analytic solutions in Figures 4.17 – 4.34. They are shown for all periods of investigation along meridional profiles at $\phi = 0^\circ$ (Figures 4.17 – 4.19), 90° (Figures 4.20 – 4.22), 180° (Figures 4.23 – 4.25), and 270° (Figures 4.26 – 4.28), and along azimuthal profiles at $\theta = 45^\circ$ (Figures 4.29 – 4.31) and 135° (Figures 4.32 – 4.34). The solutions compare very well to the semi-analytic solutions, with the largest deviations again being found in B_ϕ at the shorter periods. Once again, this component is itself very small, and the noise in the solutions may appear large in comparison, although in most cases this noise is less than 1 nT in amplitude. It is also notable that the semi-analytic solution for this component at 6-hour period is curiously oscillatory, and is likely to be inaccurate itself. More information about this will likely become available when other researchers present results for this model.

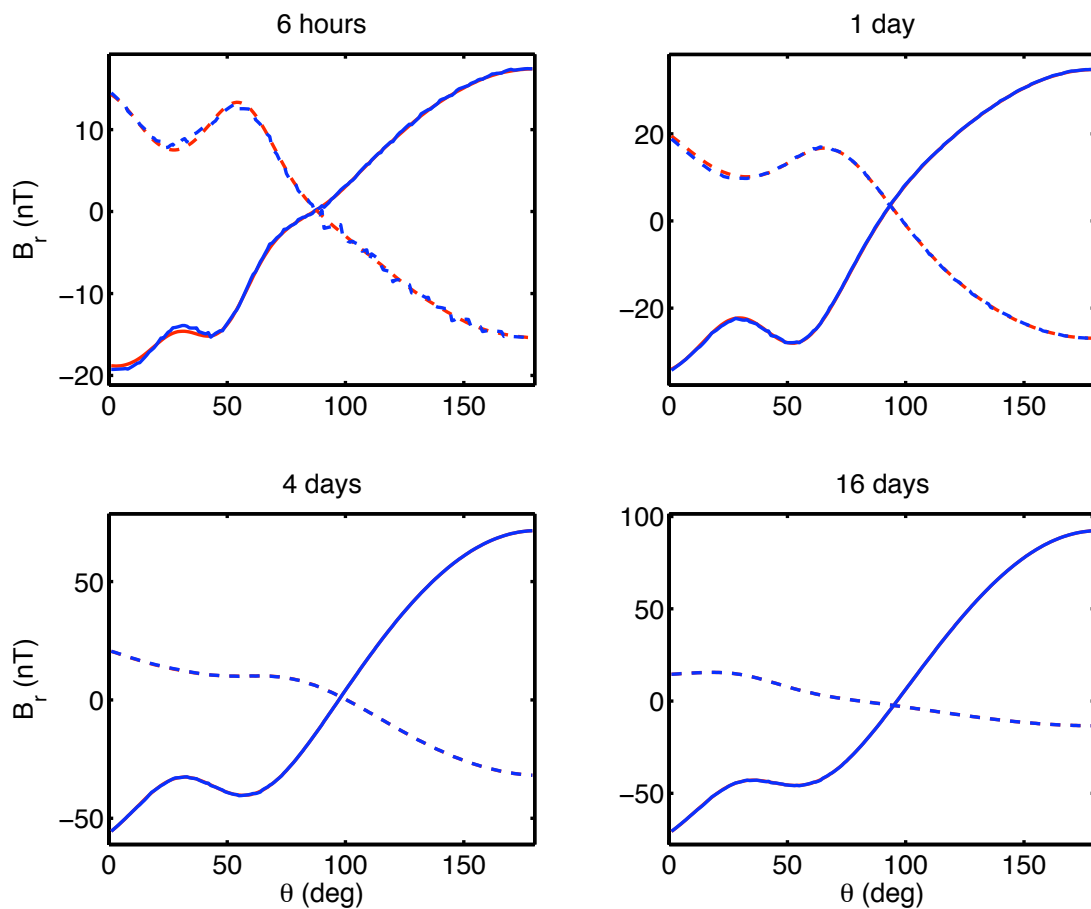


Figure 4.17: Meridional profiles of the real (solid) and imaginary (dashed) parts of B_r for longitude $\phi = 0^\circ$ in Model 3 for periods of 6 hours, 1 day, 4 days, and 16 days as calculated by the author with FlexPDE (blue). The semi-analytic solution is shown in red.

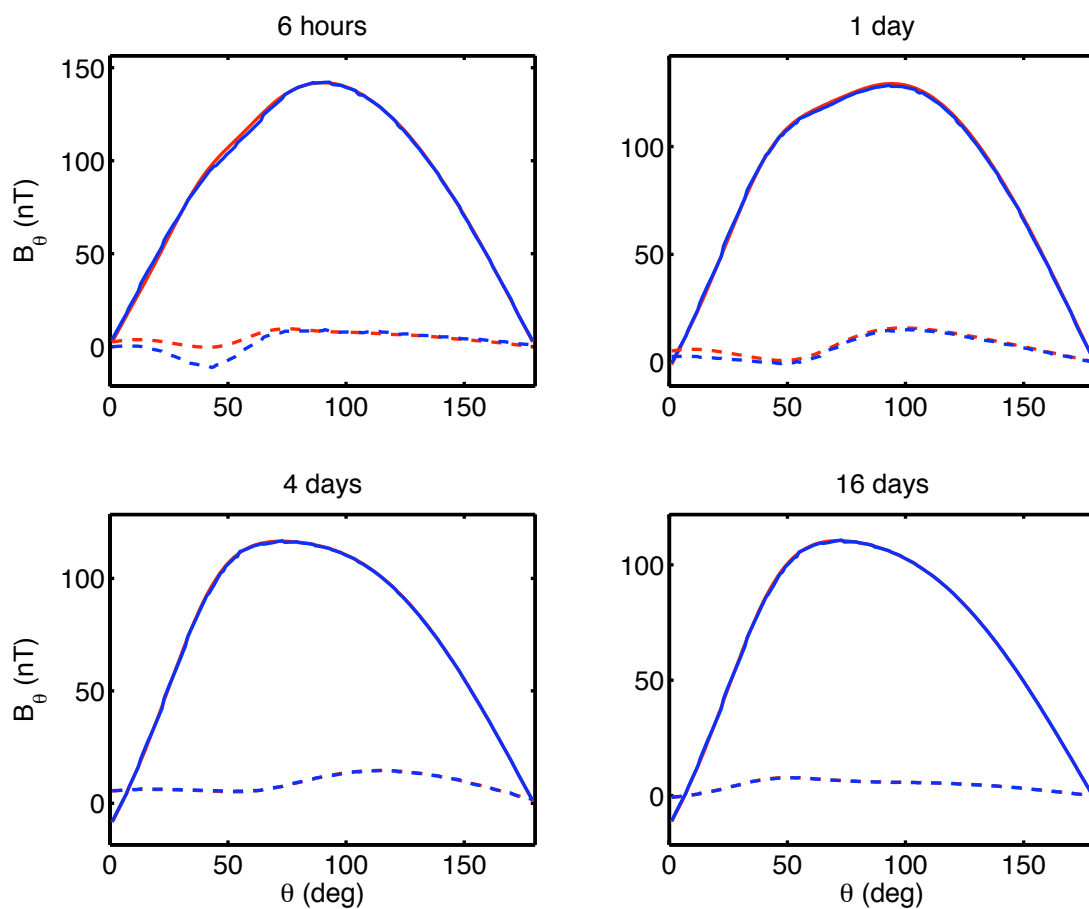


Figure 4.18: Meridional profiles of the real (solid) and imaginary (dashed) parts of B_θ for longitude $\phi = 0^\circ$ in Model 3 for periods of 6 hours, 1 day, 4 days, and 16 days as calculated by the author with FlexPDE (blue). The semi-analytic solution is shown in red.

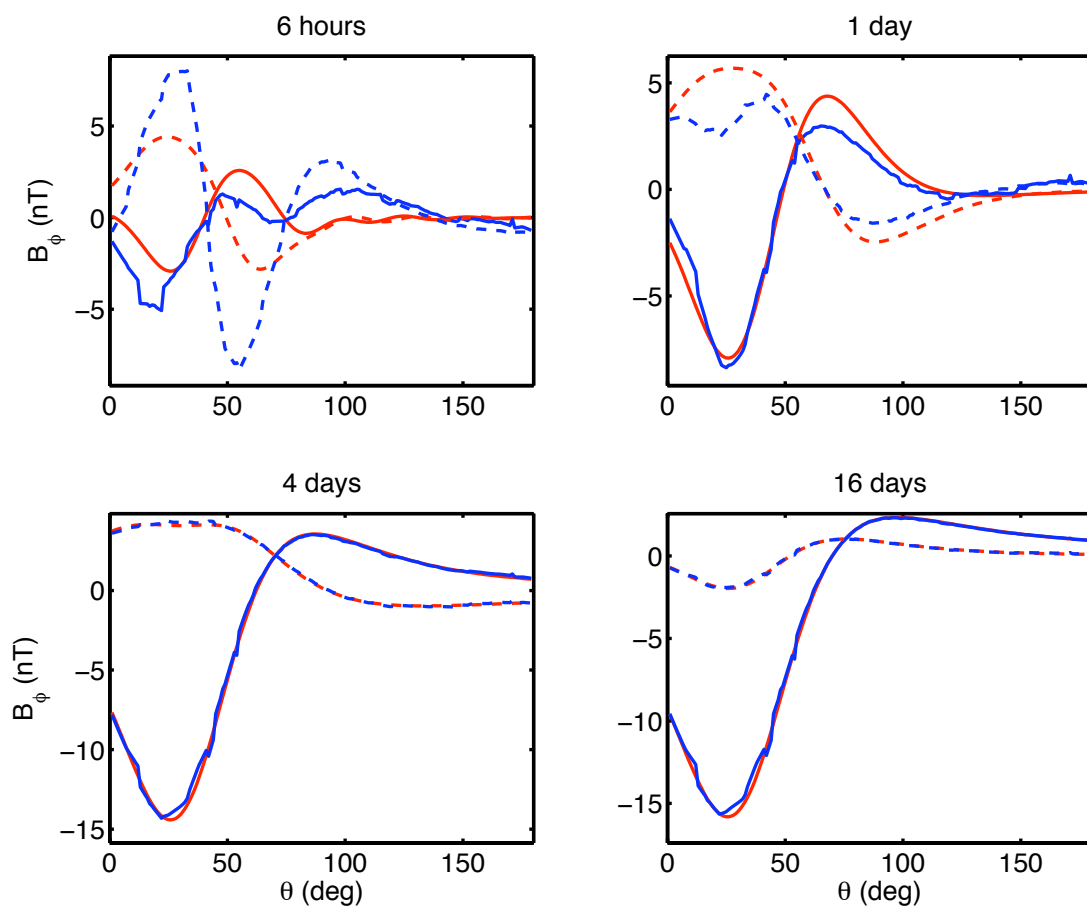


Figure 4.19: Meridional profiles of the real (solid) and imaginary (dashed) parts of B_ϕ for longitude $\phi = 0^\circ$ in Model 3 for periods of 6 hours, 1 day, 4 days, and 16 days as calculated by the author with FlexPDE (blue). The semi-analytic solution is shown in red.

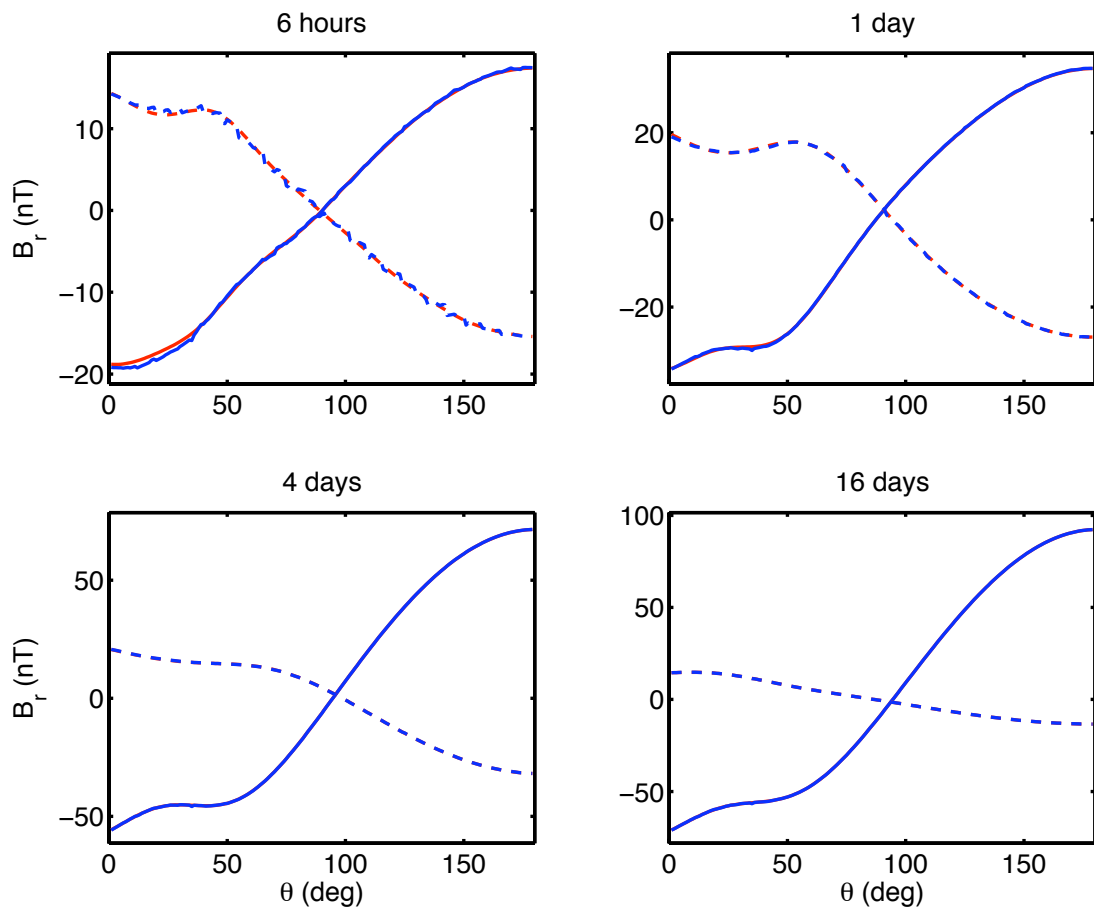


Figure 4.20: Meridional profiles of the real (solid) and imaginary (dashed) parts of B_r for longitude $\phi = 90^\circ$ in Model 3 for periods of 6 hours, 1 day, 4 days, and 16 days as calculated by the author with FlexPDE (blue). The semi-analytic solution is shown in red.

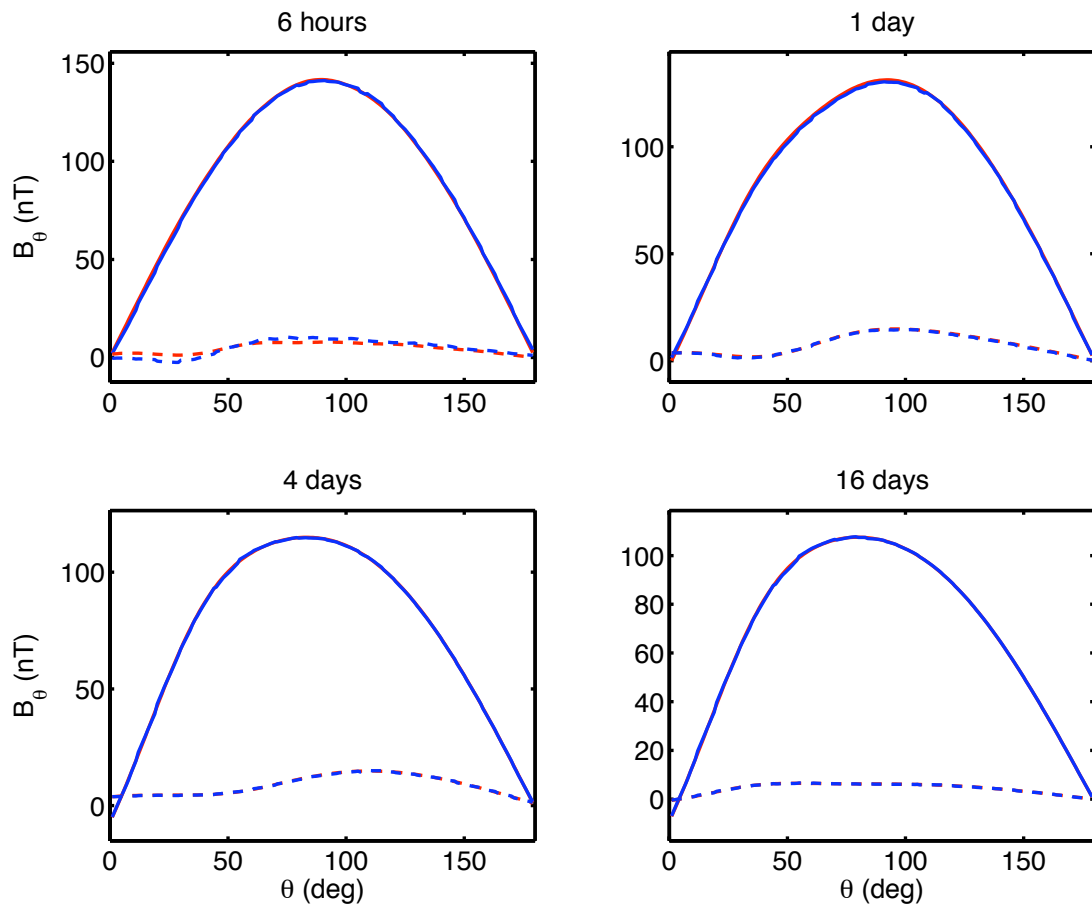


Figure 4.21: Meridional profiles of the real (solid) and imaginary (dashed) parts of B_θ for longitude $\phi = 90^\circ$ in Model 3 for periods of 6 hours, 1 day, 4 days, and 16 days as calculated by the author with FlexPDE (blue). The semi-analytic solution is shown in red.

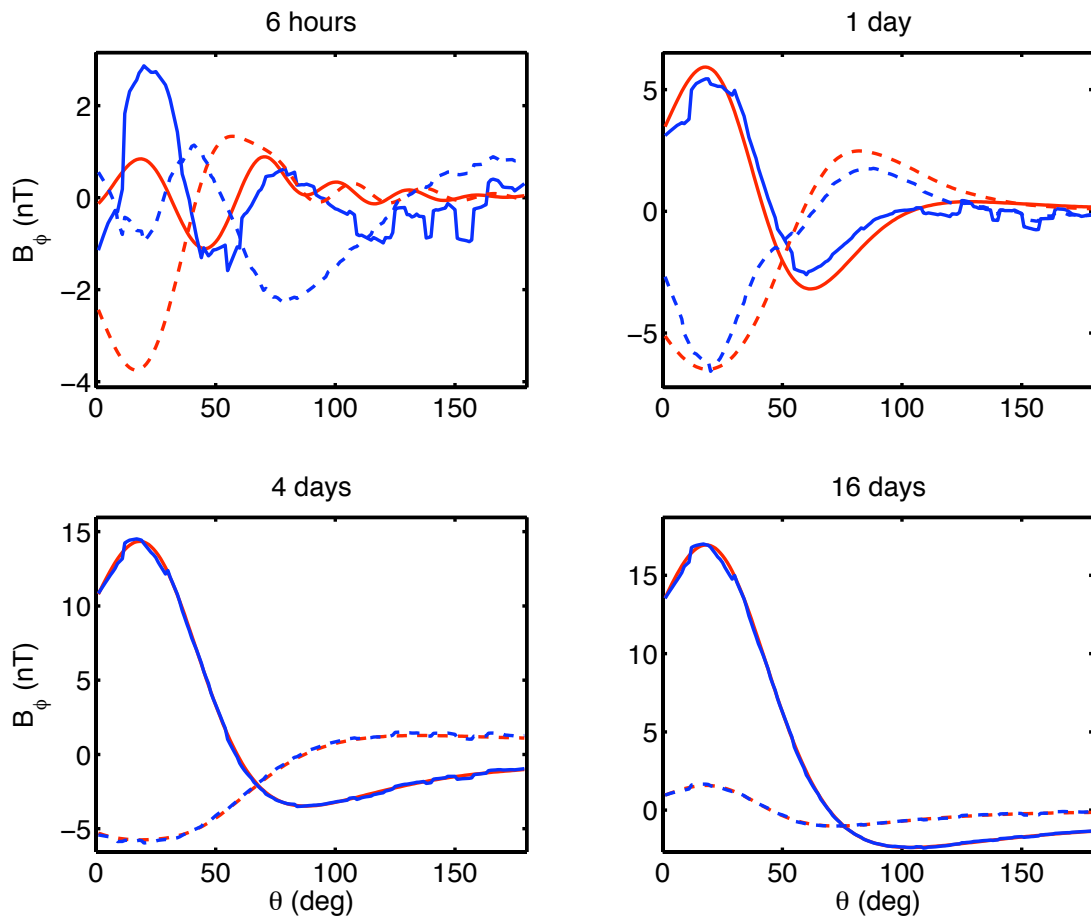


Figure 4.22: Meridional profiles of the real (solid) and imaginary (dashed) parts of B_ϕ for longitude $\phi = 90^\circ$ in Model 3 for periods of 6 hours, 1 day, 4 days, and 16 days as calculated by the author with FlexPDE (blue). The semi-analytic solution is shown in red.

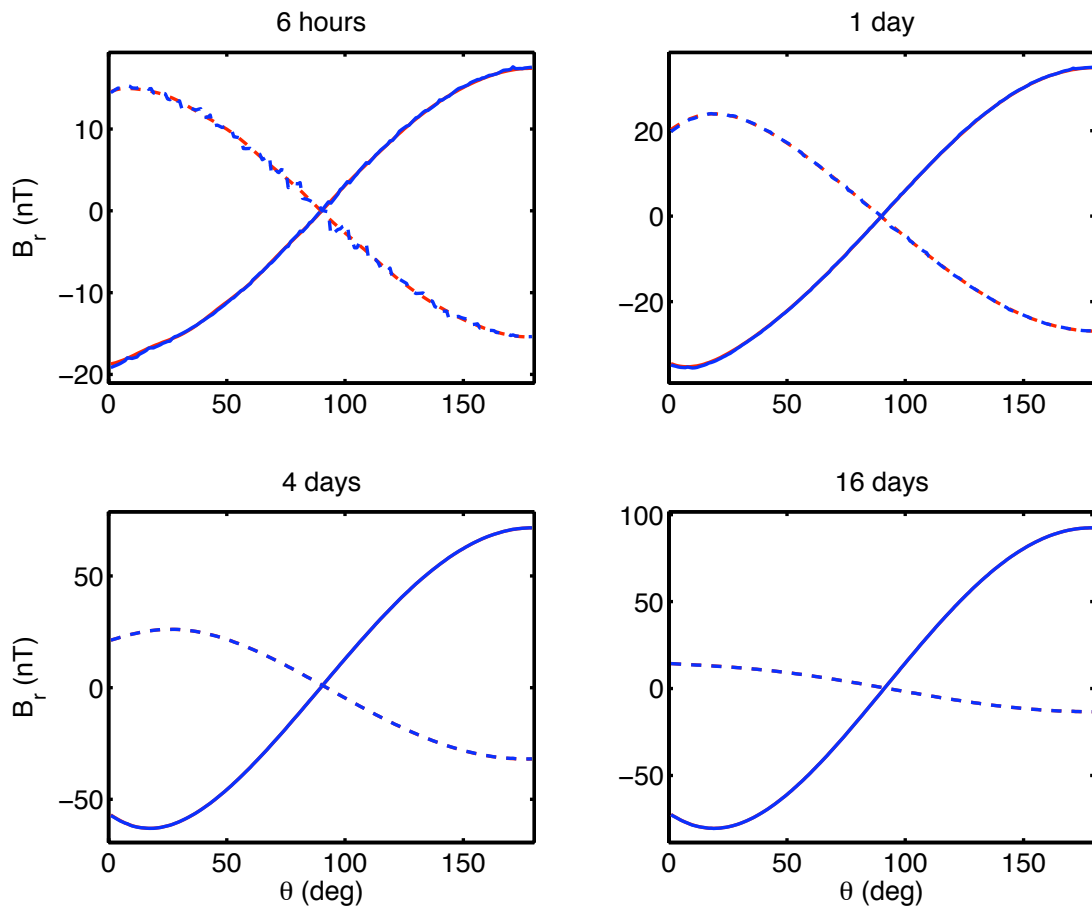


Figure 4.23: Meridional profiles of the real (solid) and imaginary (dashed) parts of B_r for longitude $\phi = 180^\circ$ in Model 3 for periods of 6 hours, 1 day, 4 days, and 16 days as calculated by the author with FlexPDE (blue). The semi-analytic solution is shown in red.

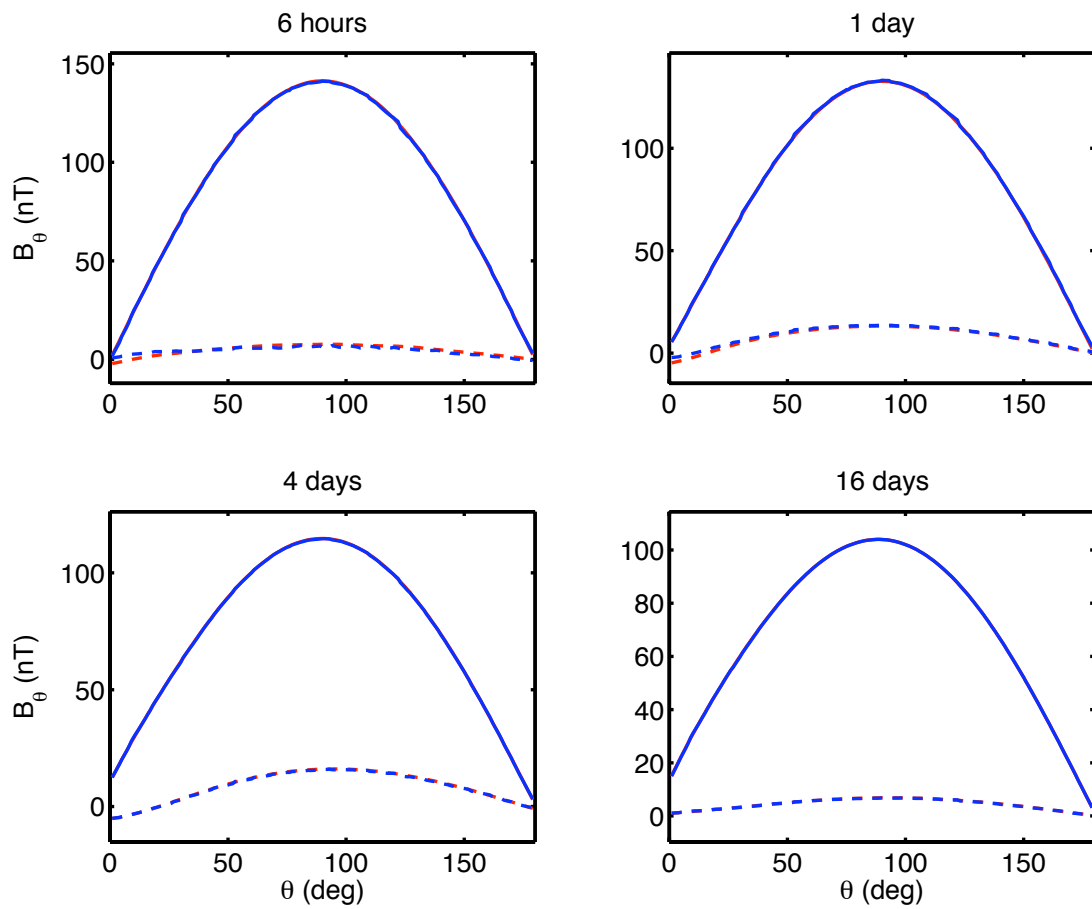


Figure 4.24: Meridional profiles of the real (solid) and imaginary (dashed) parts of B_θ for longitude $\phi = 180^\circ$ in Model 3 for periods of 6 hours, 1 day, 4 days, and 16 days as calculated by the author with FlexPDE (blue). The semi-analytic solution is shown in red.

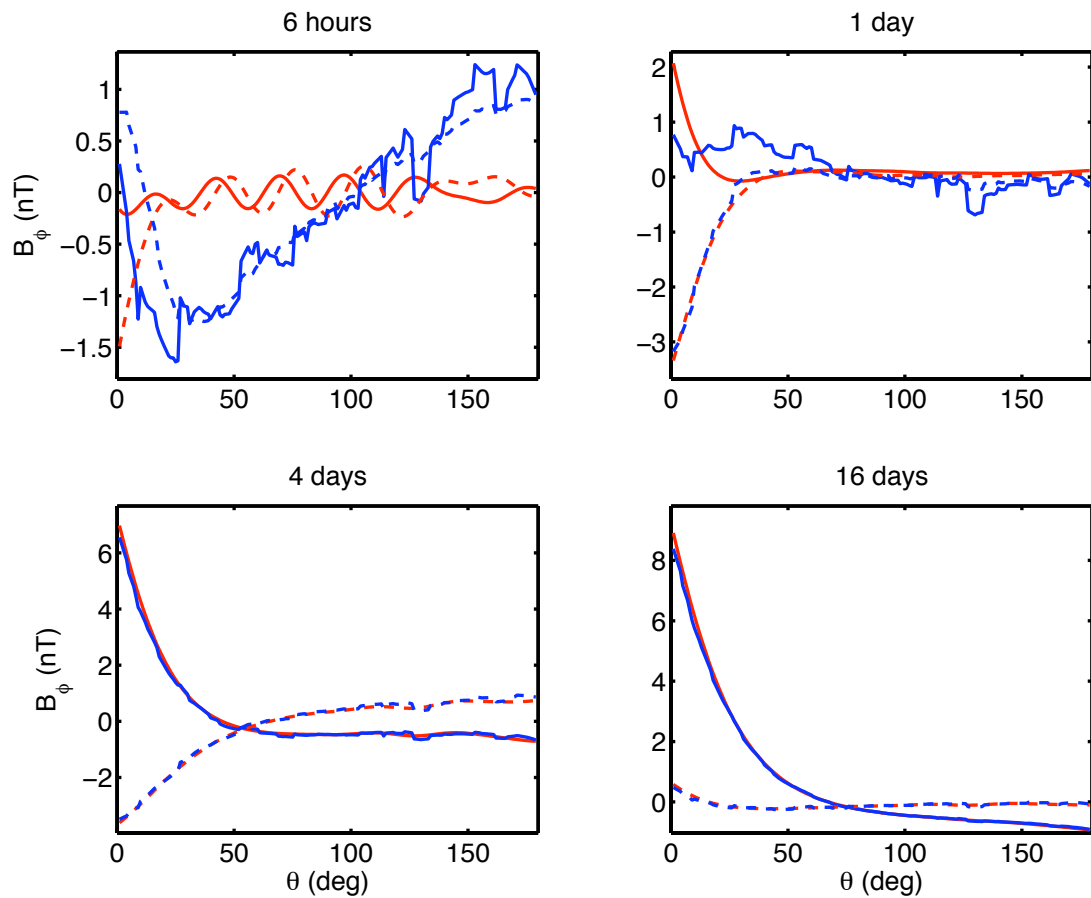


Figure 4.25: Meridional profiles of the real (solid) and imaginary (dashed) parts of B_ϕ for longitude $\phi = 180^\circ$ in Model 3 for periods of 6 hours, 1 day, 4 days, and 16 days as calculated by the author with FlexPDE (blue). The semi-analytic solution is shown in red.

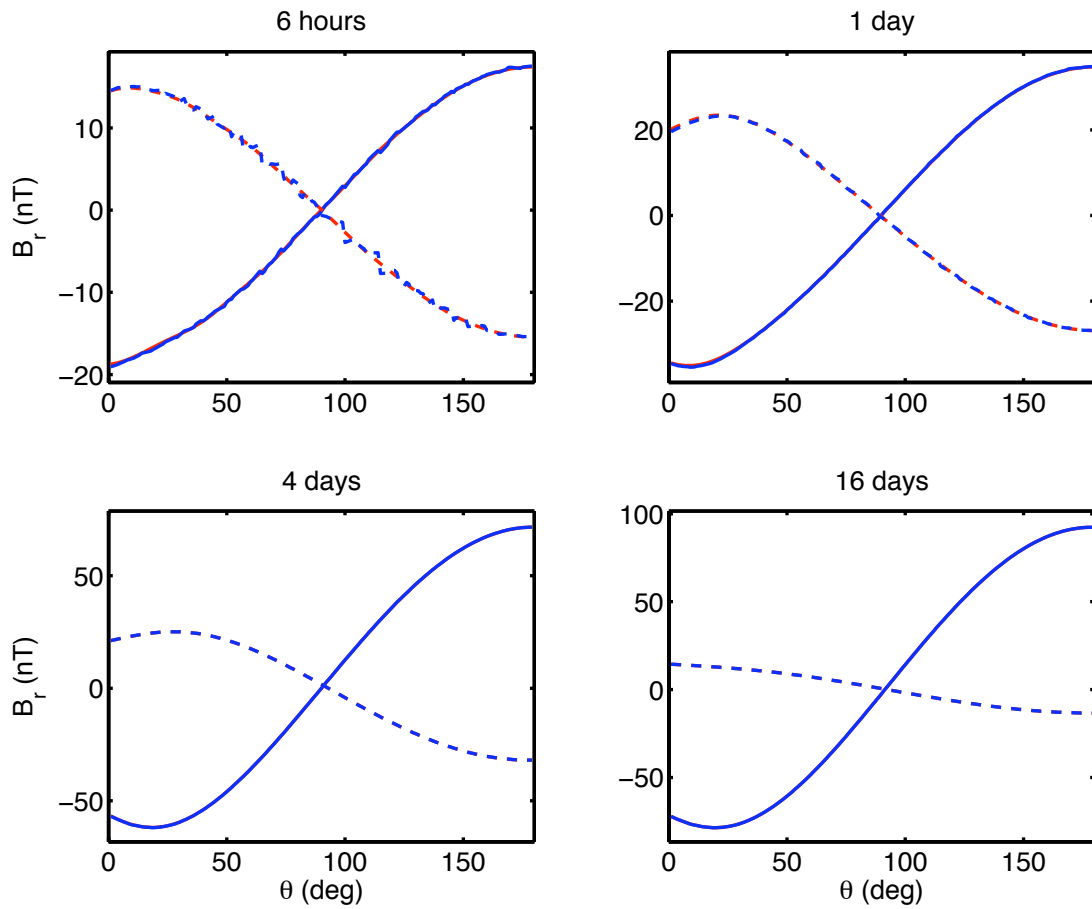


Figure 4.26: Meridional profiles of the real (solid) and imaginary (dashed) parts of B_r for longitude $\phi = 270^\circ$ in Model 3 for periods of 6 hours, 1 day, 4 days, and 16 days as calculated by the author with FlexPDE (blue). The semi-analytic solution is shown in red.

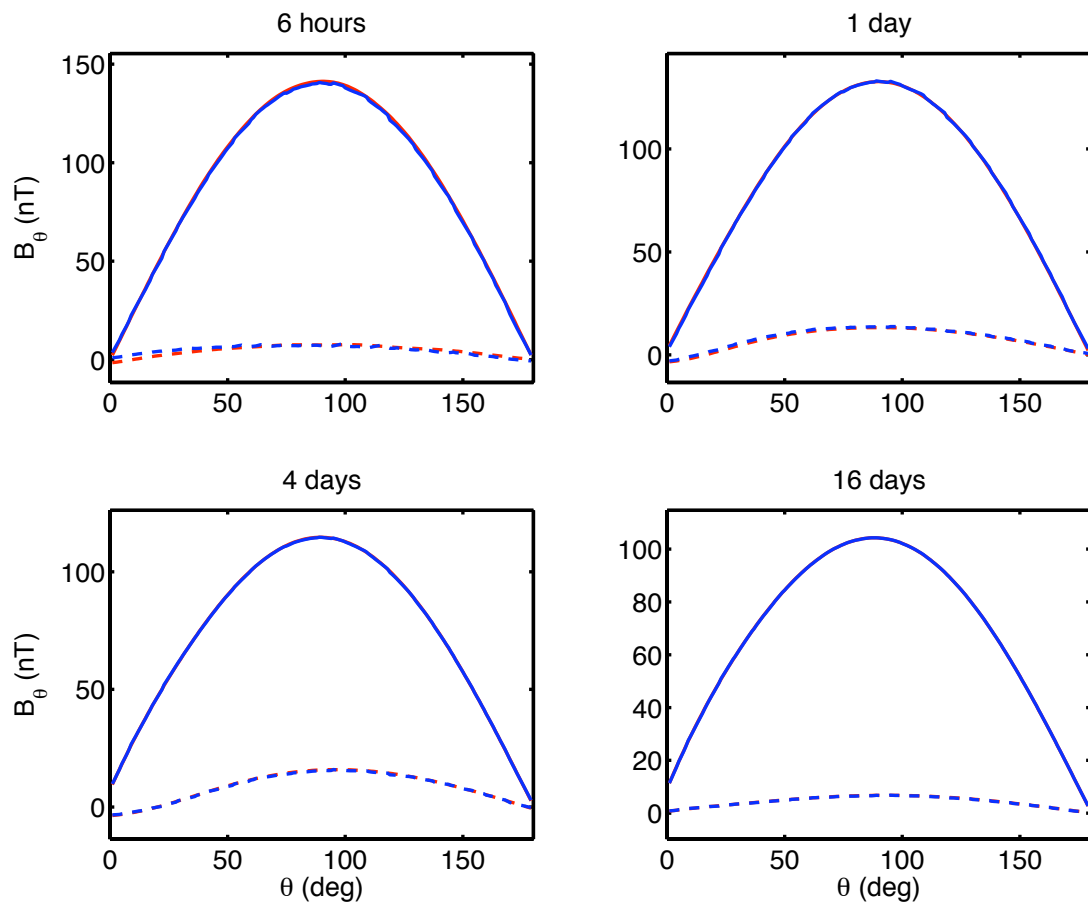


Figure 4.27: Meridional profiles of the real (solid) and imaginary (dashed) parts of B_θ for longitude $\phi = 270^\circ$ in Model 3 for periods of 6 hours, 1 day, 4 days, and 16 days as calculated by the author with FlexPDE (blue). The semi-analytic solution is shown in red.

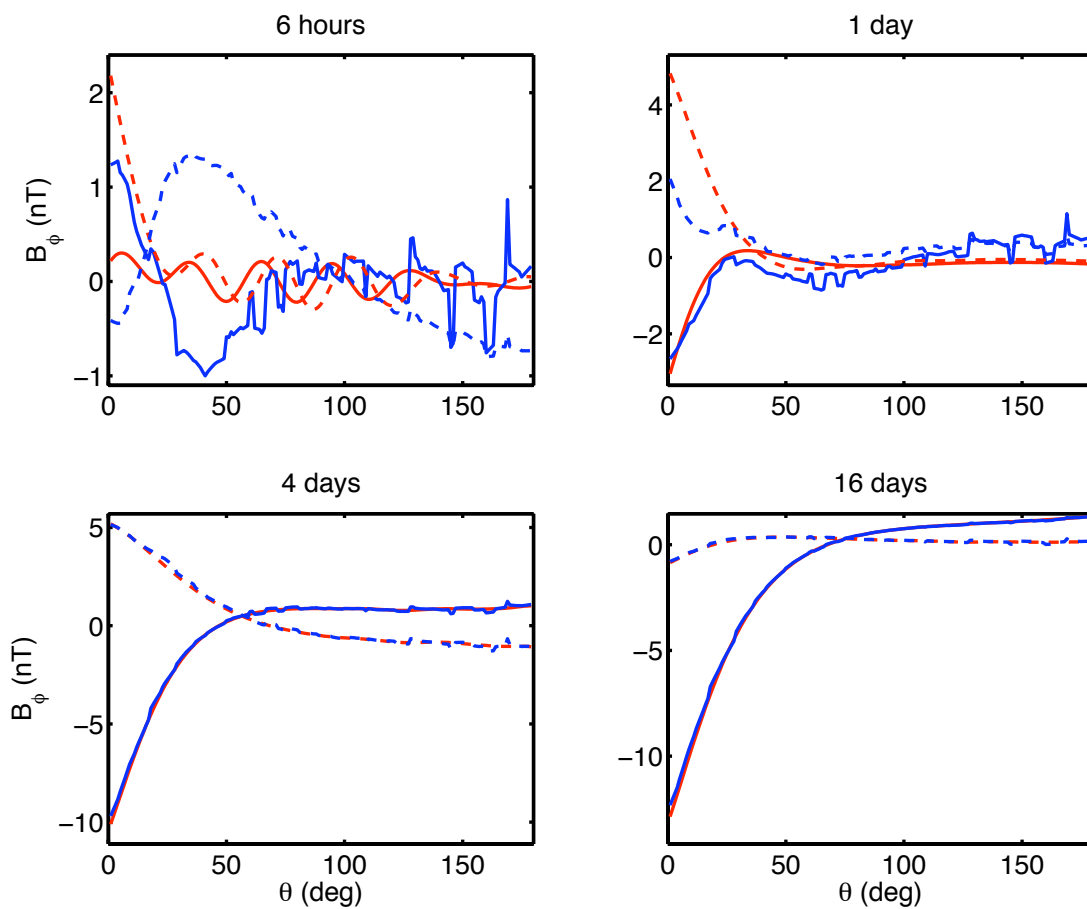


Figure 4.28: Meridional profiles of the real (solid) and imaginary (dashed) parts of B_ϕ for longitude $\phi = 270^\circ$ in Model 3 for periods of 6 hours, 1 day, 4 days, and 16 days as calculated by the author with FlexPDE (blue). The semi-analytic solution is shown in red.

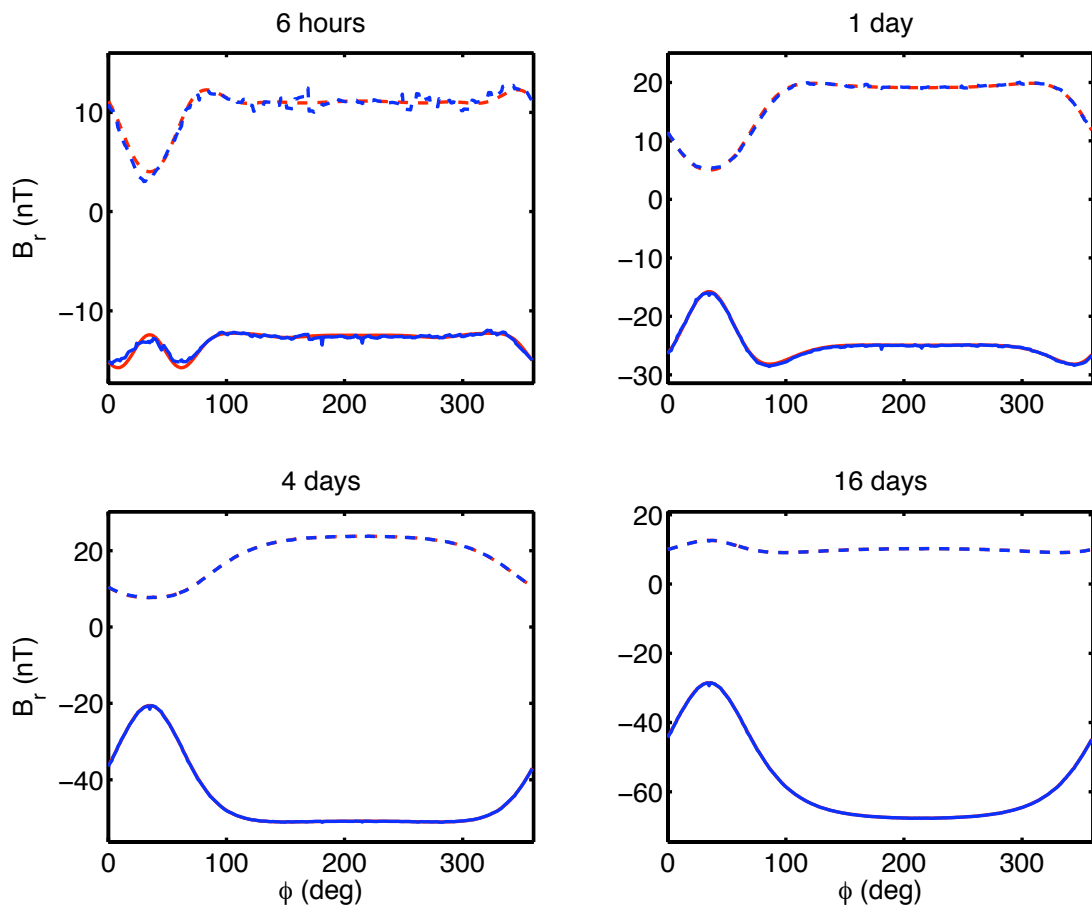


Figure 4.29: Azimuthal profiles of the real (solid) and imaginary (dashed) parts of B_r for longitude $\theta = 45^\circ$ in Model 3 for periods of 6 hours, 1 day, 4 days, and 16 days as calculated by the author with FlexPDE (blue). The semi-analytic solution is shown in red.

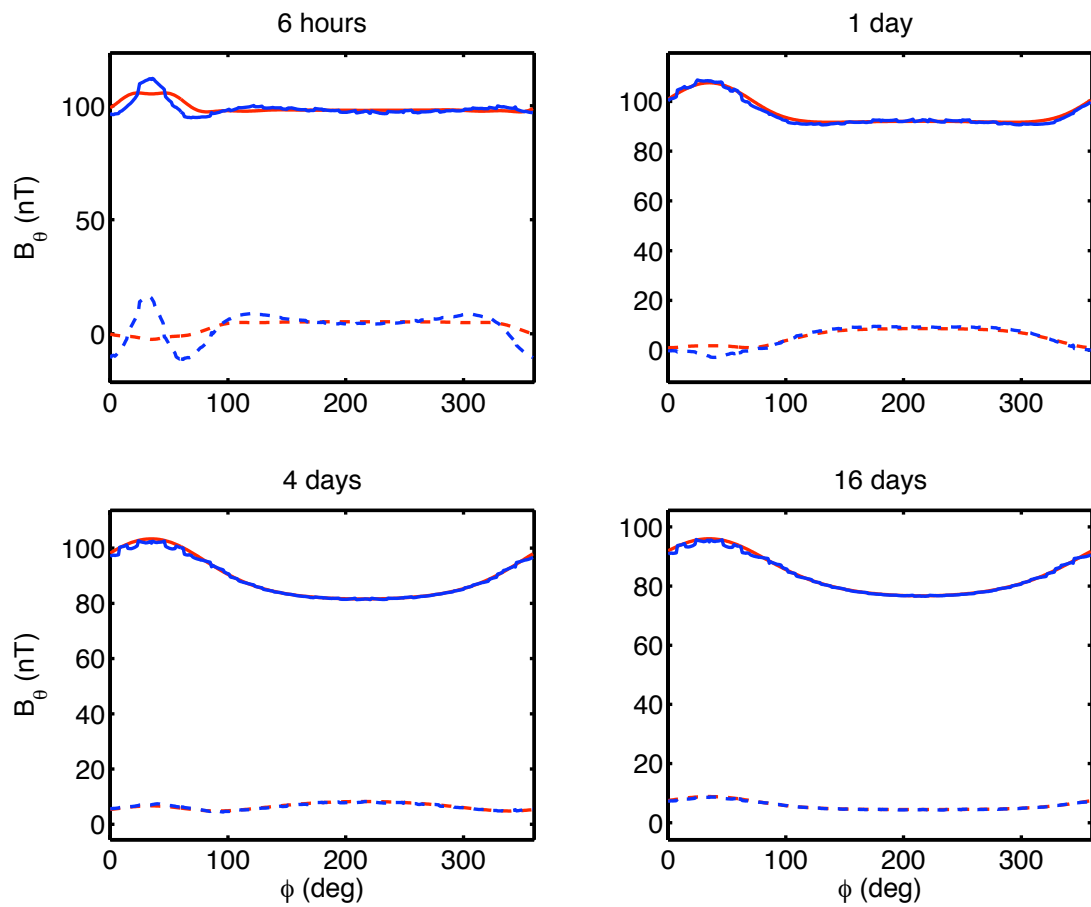


Figure 4.30: Meridional profiles of the real (solid) and imaginary (dashed) parts of B_θ for longitude $\theta = 45^\circ$ in Model 3 for periods of 6 hours, 1 day, 4 days, and 16 days as calculated by the author with FlexPDE (blue). The semi-analytic solution is shown in red.

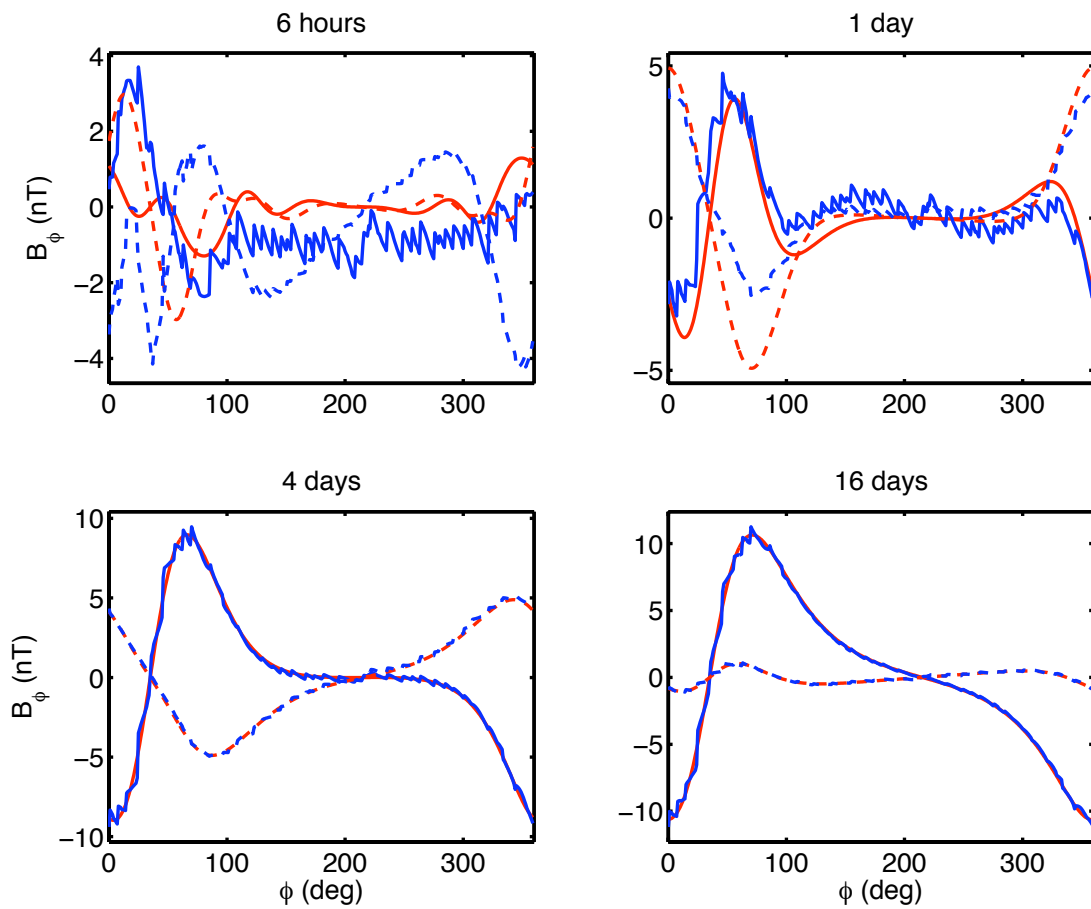


Figure 4.31: Meridional profiles of the real (solid) and imaginary (dashed) parts of B_ϕ for longitude $\theta = 45^\circ$ in Model 3 for periods of 6 hours, 1 day, 4 days, and 16 days as calculated by the author with FlexPDE (blue). The semi-analytic solution is shown in red.

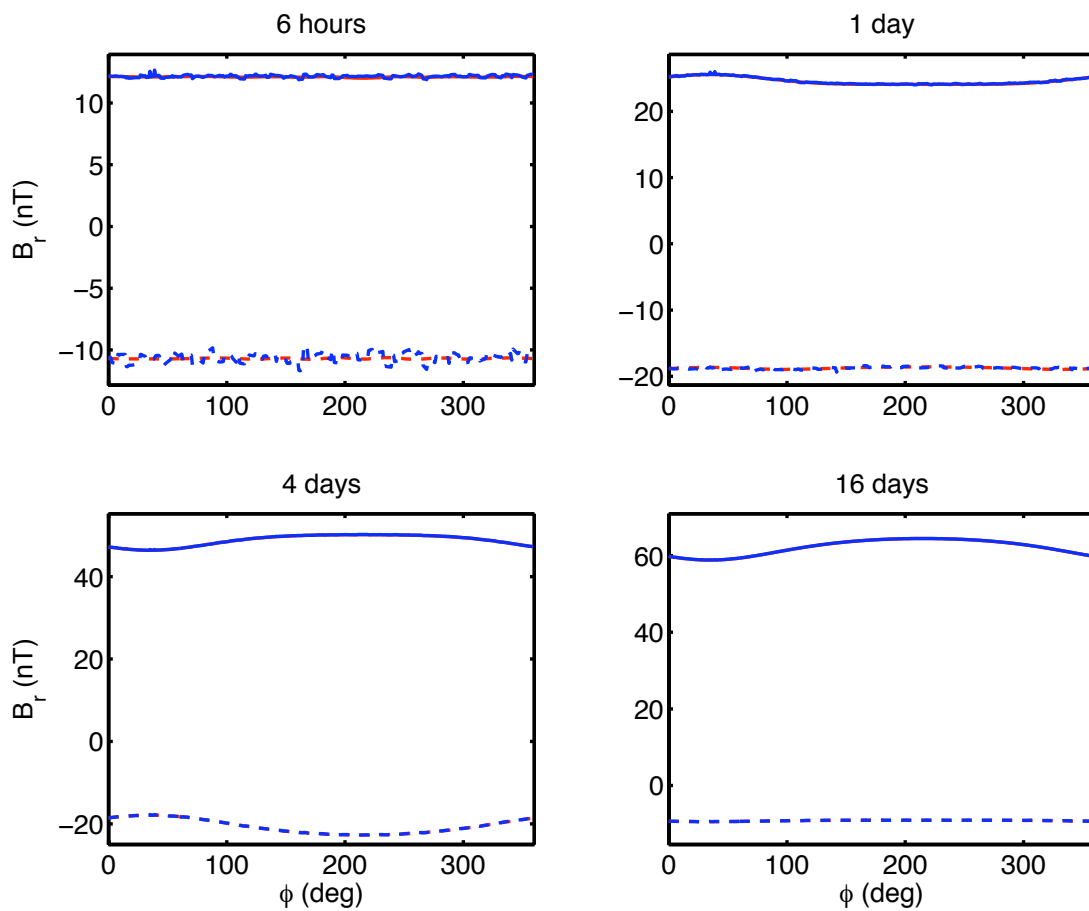


Figure 4.32: Azimuthal profiles of the real (solid) and imaginary (dashed) parts of B_r for longitude $\theta = 135^\circ$ in Model 3 for periods of 6 hours, 1 day, 4 days, and 16 days as calculated by the author with FlexPDE (blue). The semi-analytic solution is shown in red.

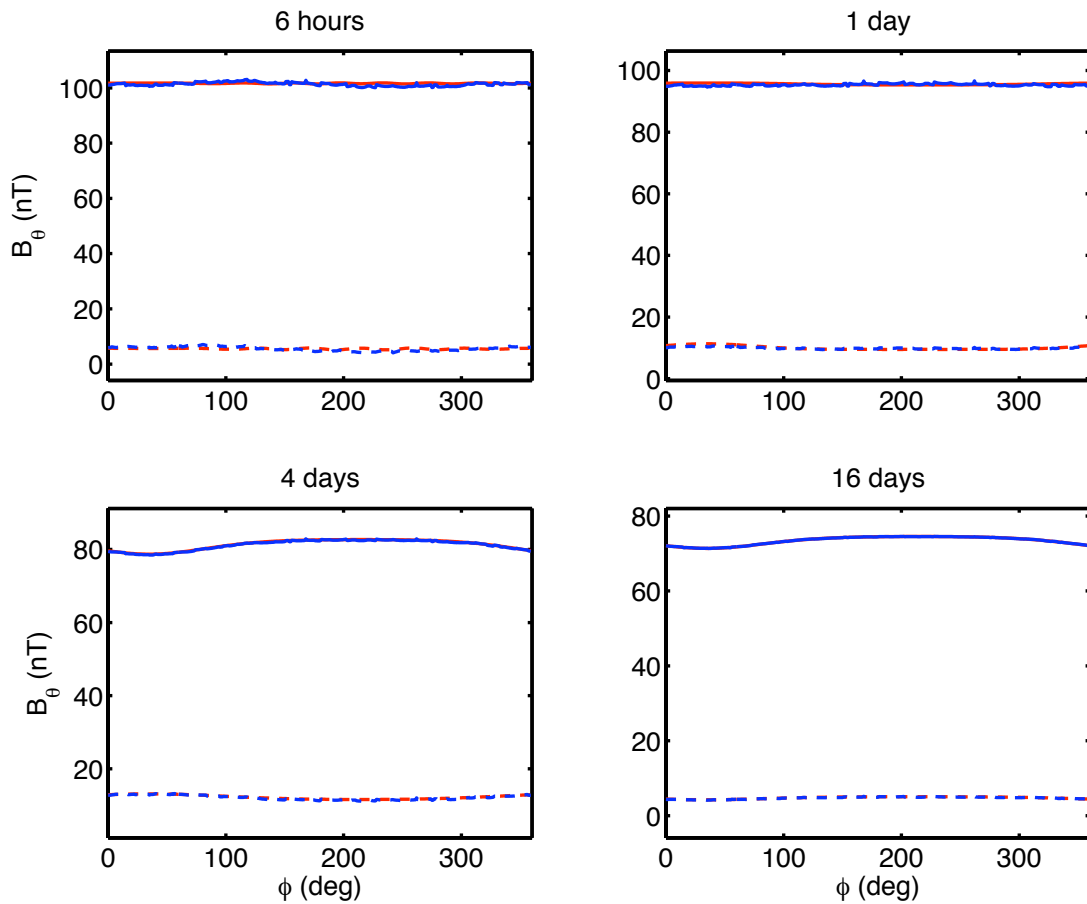


Figure 4.33: Meridional profiles of the real (solid) and imaginary (dashed) parts of B_θ for longitude $\theta = 135^\circ$ in Model 3 for periods of 6 hours, 1 day, 4 days, and 16 days as calculated by the author with FlexPDE (blue). The semi-analytic solution is shown in red.

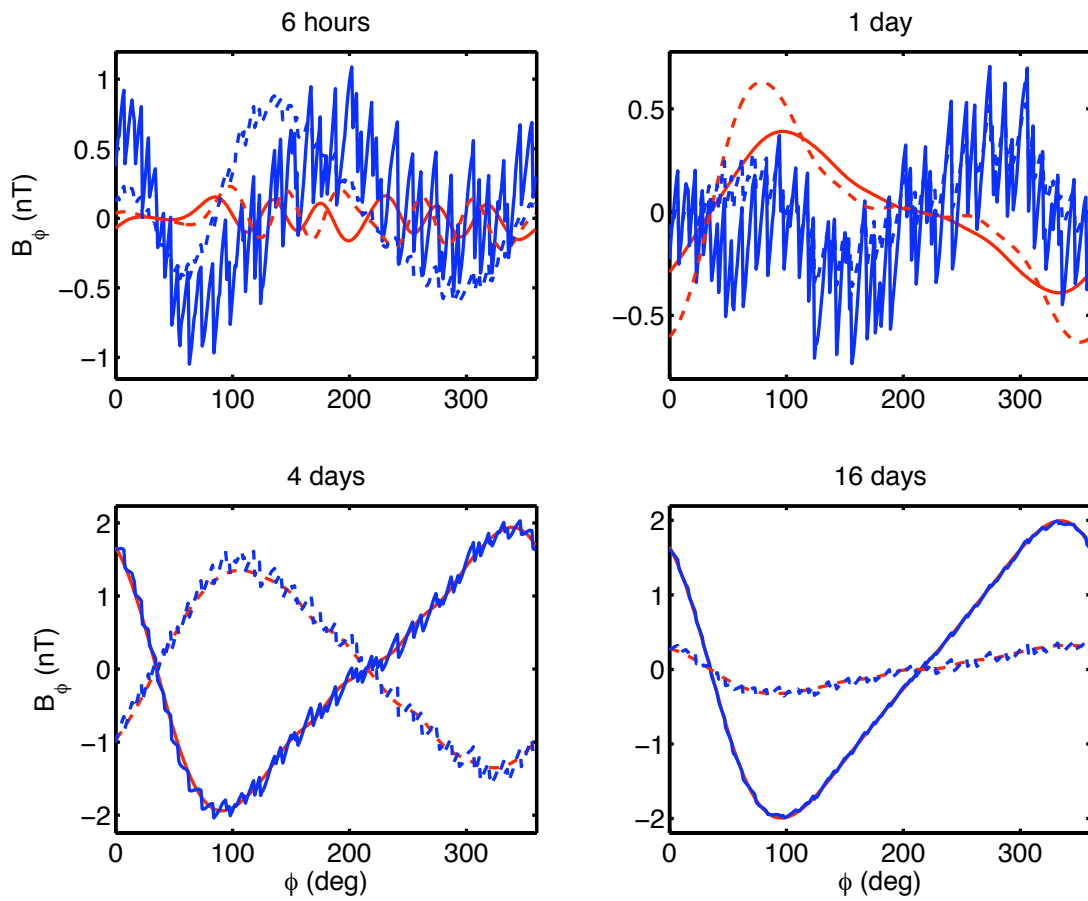


Figure 4.34: Meridional profiles of the real (solid) and imaginary (dashed) parts of B_ϕ for longitude $\theta = 135^\circ$ in Model 3 for periods of 6 hours, 1 day, 4 days, and 16 days as calculated by the author with FlexPDE (blue). The semi-analytic solution is shown in red.

Table 4.7: Electrical conductivities used in Models 6.

Depth (km)	σ (S/m)
0–400	0.01
400–800	0.1
800–2871	1.0
2871–6371	5×10^5

Table 4.8: Runtimes for Model 6.

Period	Runtime (hours)
16 days	25.25
4 days	13.5
1 day	33.5
6 hours	97

4.5 Model 6: 3D Surface Conductance Map Over Radial Conductivity Model

Earth is represented in Model 6 as a set of four concentric uniform spheres with conductivities described in Table 4.7, overlain at the CVI by an infinitely thin $1^\circ \times 1^\circ$ conductance map (Everett *et al.*, 2003) representing the realistic conductivity of Earth’s oceans and continents, as seen in Figure 4.35. The external dipole field is aligned with the GM axis, the North pole of which is located at geographic longitude $\phi_g = -72^\circ$, and geographic colatitude $\theta_g = 10^\circ$.

This model is computationally analogous to Model 2, although the conductivity profile is different, and the FlexPDE method computes solutions for five complex variables. However the conductance map of Model 6 is more complicated than that of Model 2, which can increase runtimes, described in Table 4.8

As with Model 3, no other researchers have yet presented their solutions for Model 6, however in this case there is no analytic or semi-analytic solution to compare with the FlexPDE solution. Thus there is little basis for judging the accuracy of the FlexPDE solutions, which are presented in Figures 4.37 – 4.54 along the same profiles as were used for Model 3. Nonetheless, the analytic solutions for a 1D version of Model 6 that lacks a surface conductance map can be used as a

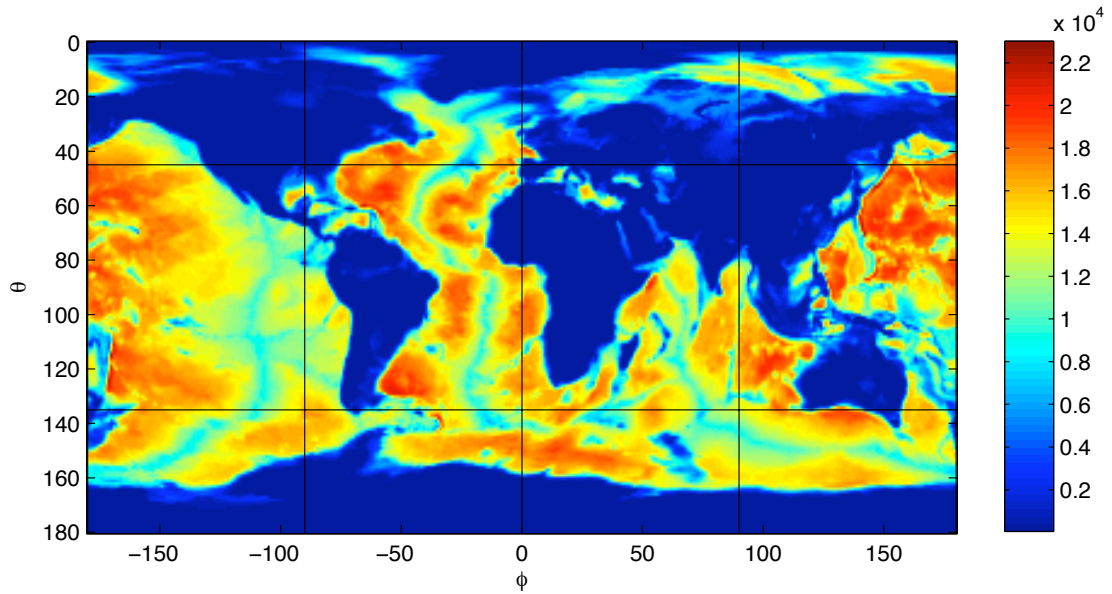


Figure 4.35: Map of the surface conductance τ used for Model 6, shown here in terms of geomagnetic colatitude θ and geomagnetic longitude ϕ . The color scale is in units of S. Black lines indicate the azimuthal and meridional profiles along which the synthetic data is collected to generate the plots in Figures 4.36 – 4.54.

qualitative comparison, and are plotted in the same figures.

It is notable that the deviations of the 3D solutions from the 1D solutions follow a systematic pattern. Short wavelength spikes in B_r and B_θ are present at conductivity contrasts (northern and southern coastlines) along the meridional profiles, while longer wavelength anomalies are visible in B_ϕ along eastern and western coastlines. These features indicate the *coast effect* (Parker, 1968), the channeling of electric current within the surface layer that is caused when an east-west directed oceanic electric current encounters a resistive continent and deviates poleward along the coast. These north- or south-directed currents generate a significant amplitude in B_ϕ , which vanishes in an azimuthally symmetric model. The deviated currents then curve around the northern or southern coast of the continent, which greatly enhances the azimuthal current density in the oceans near these coasts, and generates anomalies in B_r and B_θ . The coast effect manifests in the azimuthal profiles with long wavelength patterns in B_r and B_θ that clearly indicate the locations of the oceans and continents, and sawtooth patterns in B_ϕ

that clearly indicate the coastlines.

The coast effect can be seen in maps of the anomalous radial field, $B_{r,a}$ calculated by

$$B_{r,a} = B_r - B_{r,1D}, \quad (4.4)$$

where $B_{r,1D}$ is the radial field from an Earth model that has equivalent conductivity, but lacks surface conductance. Such a map is shown in Figure 4.36 for a source period of 6 hours, and clearly delineates the continental coastlines, especially the northern and southern coasts. This effect can lead to anomalous results in response functions estimated from observatories located near these coastlines, such as the one in Hermanus, on the southern coast of Africa (Constable, 1993; Kuvshinov *et al.*, 2002b).

The coast effect is more pronounced at shorter periods, for which the magnetic skin depths are small enough to concentrate the electric current in the heterogeneous outer layer. At longer periods, the magnetic fields penetrate deeper into the mantle, and more of the current flows in a homogeneous medium where it is less necessary to divert from azimuthal pathways. Once other researchers have calculated similar profiles, it will be possible to compare the bimodal solutions to our unimodal solutions, and to characterize the differences in the coast effect between the two methods.

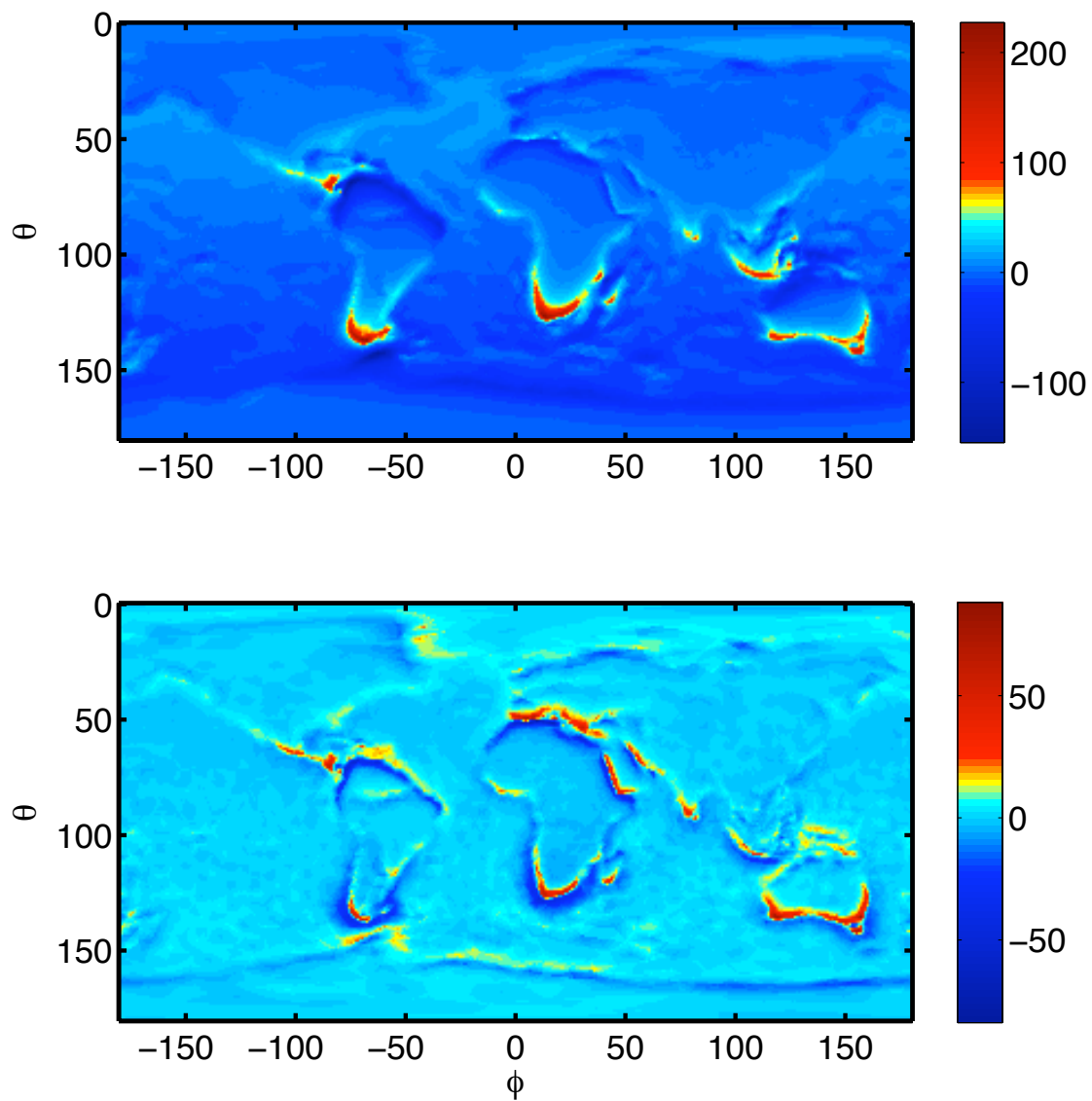


Figure 4.36: Contour map of the real (top) and imaginary (bottom) parts of the anomalous radial field $B_{r,a}$, illustrating the coast effect for Model 6 at a period of 6 hours as calculated by FlexPDE. The color scale is in units of nT.

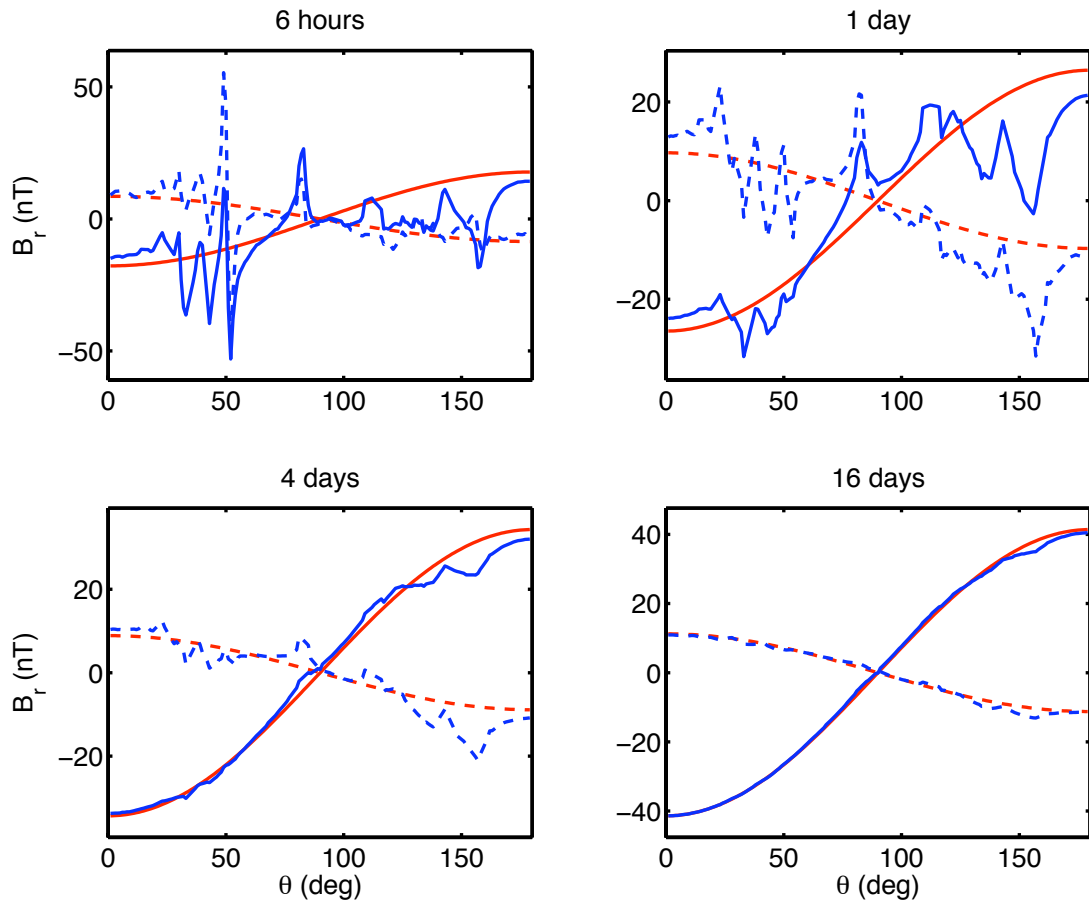


Figure 4.37: Meridional profiles of the real (solid) and imaginary (dashed) parts of B_r for longitude $\phi = 0^\circ$ in Model 6 for periods of 6 hours, 1 day, 4 days, and 16 days as calculated by the author with FlexPDE (blue). The red curves show the analytic solution for a model with the same 1D mantle conductivity, but without the surface conductance map.

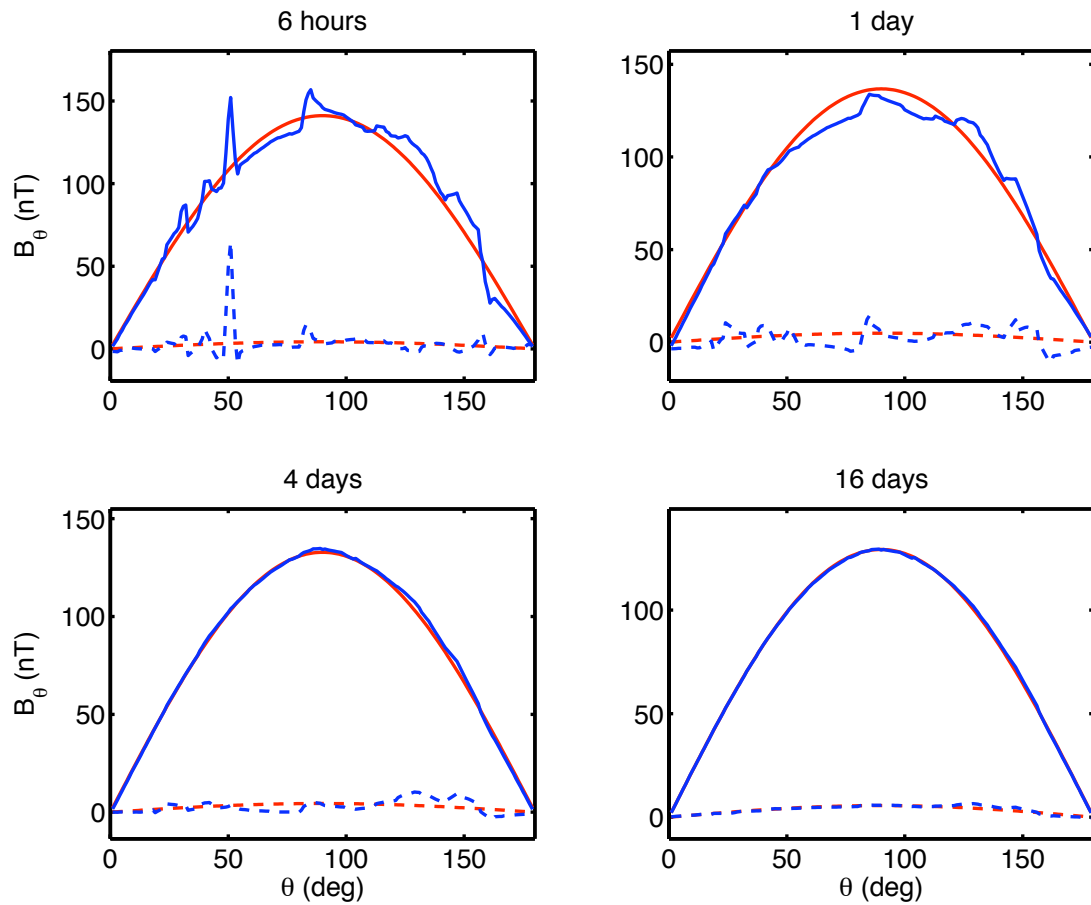


Figure 4.38: Meridional profiles of the real (solid) and imaginary (dashed) parts of B_θ for longitude $\phi = 0^\circ$ in Model 6 for periods of 6 hours, 1 day, 4 days, and 16 days as calculated by the author with FlexPDE (blue). The red curves show the analytic solution for a model with the same 1D mantle conductivity, but without the surface conductance map.

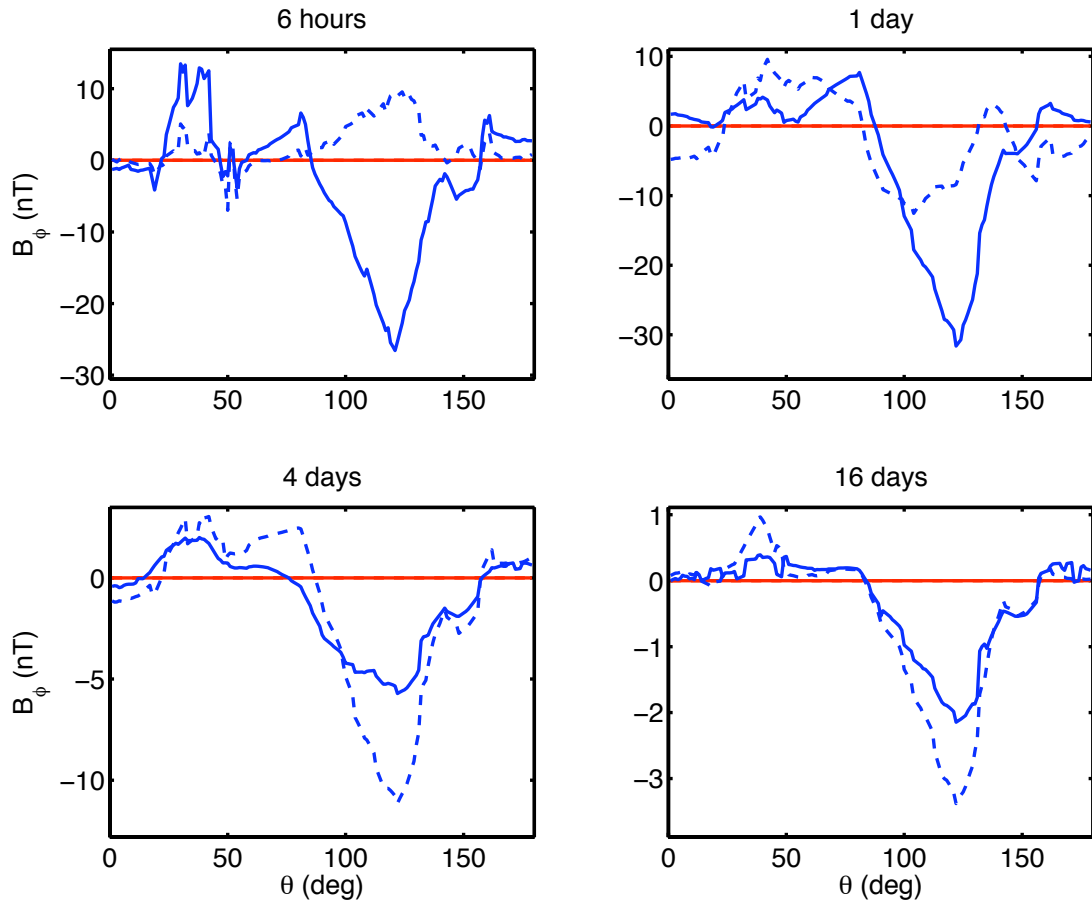


Figure 4.39: Meridional profiles of the real (solid) and imaginary (dashed) parts of B_ϕ for longitude $\phi = 0^\circ$ in Model 6 for periods of 6 hours, 1 day, 4 days, and 16 days as calculated by the author with FlexPDE (blue). The red curves show the analytic solution for a model with the same 1D mantle conductivity, but without the surface conductance map.

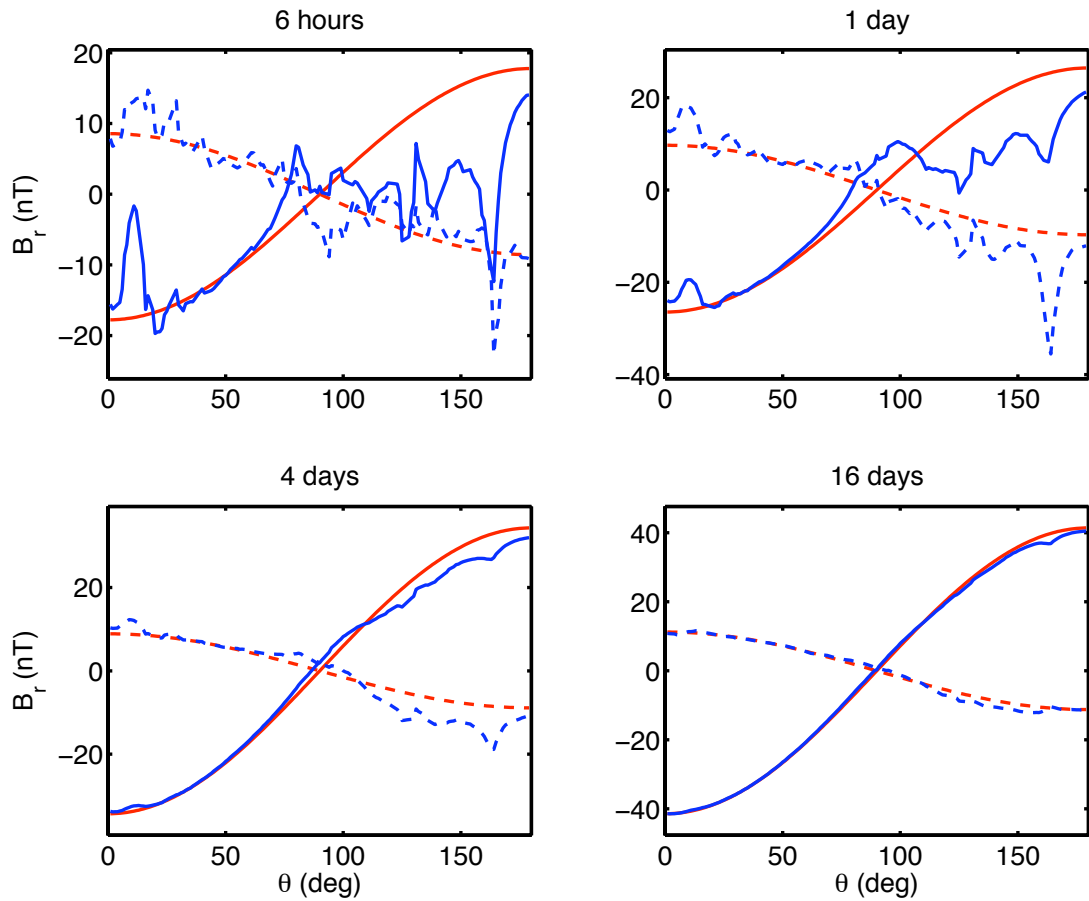


Figure 4.40: Meridional profiles of the real (solid) and imaginary (dashed) parts of B_r for longitude $\phi = 90^\circ$ in Model 6 for periods of 6 hours, 1 day, 4 days, and 16 days as calculated by the author with FlexPDE (blue). The red curves show the analytic solution for a model with the same 1D mantle conductivity, but without the surface conductance map.

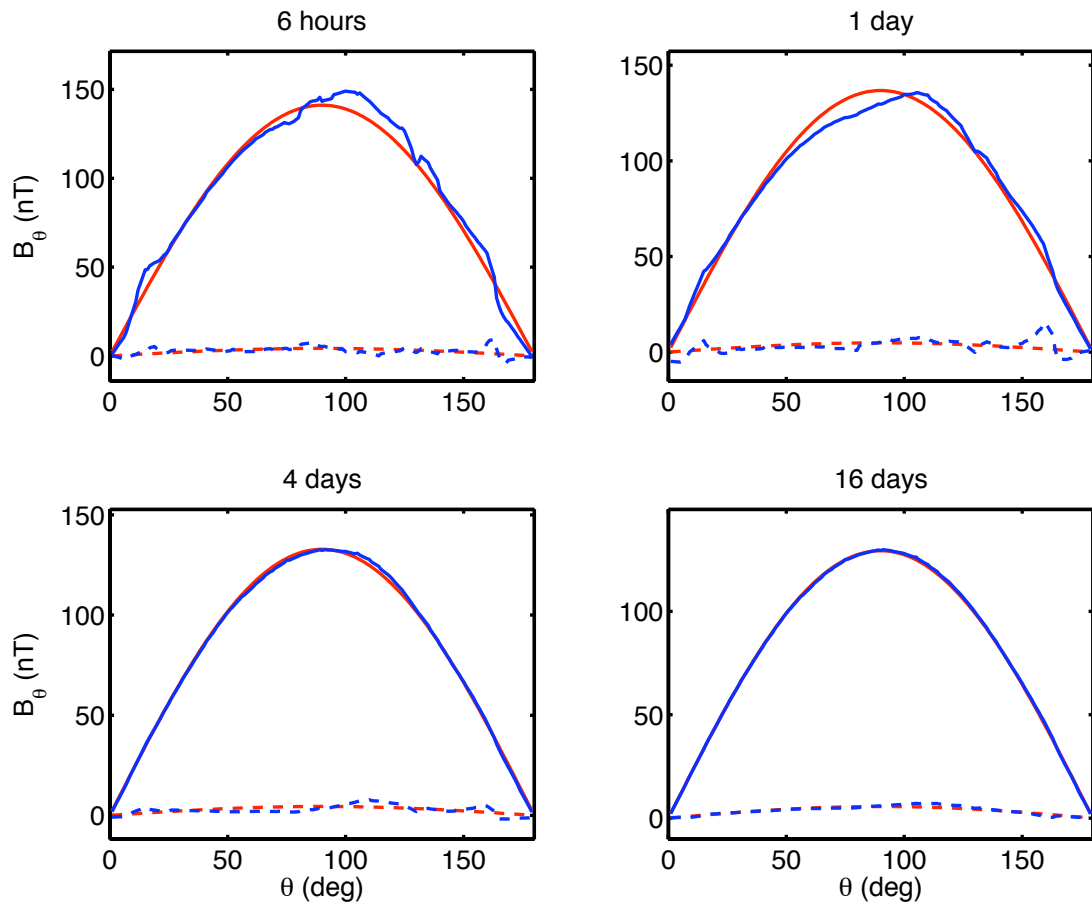


Figure 4.41: Meridional profiles of the real (solid) and imaginary (dashed) parts of B_θ for longitude $\phi = 90^\circ$ in Model 6 for periods of 6 hours, 1 day, 4 days, and 16 days as calculated by the author with FlexPDE (blue). The red curves show the analytic solution for a model with the same 1D mantle conductivity, but without the surface conductance map.

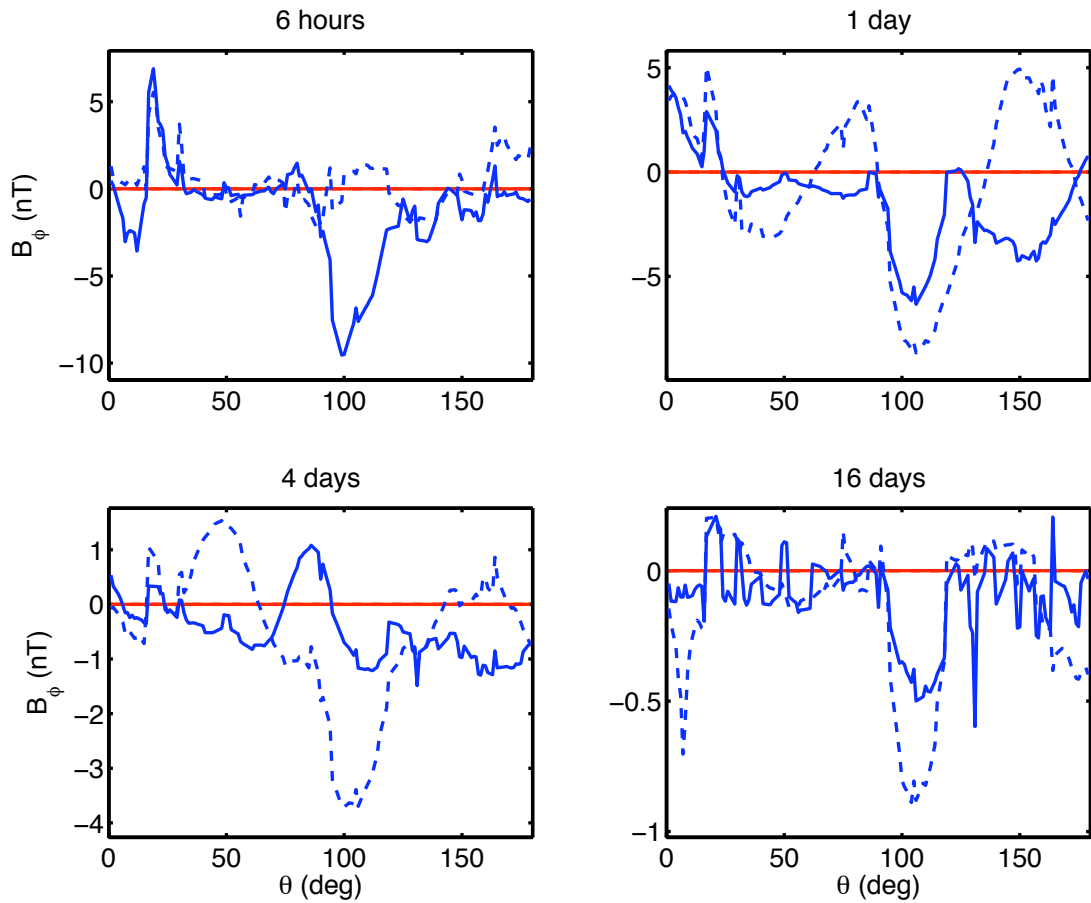


Figure 4.42: Meridional profiles of the real (solid) and imaginary (dashed) parts of B_ϕ for longitude $\phi = 90^\circ$ in Model 6 for periods of 6 hours, 1 day, 4 days, and 16 days as calculated by the author with FlexPDE (blue). The red curves show the analytic solution for a model with the same 1D mantle conductivity, but without the surface conductance map.

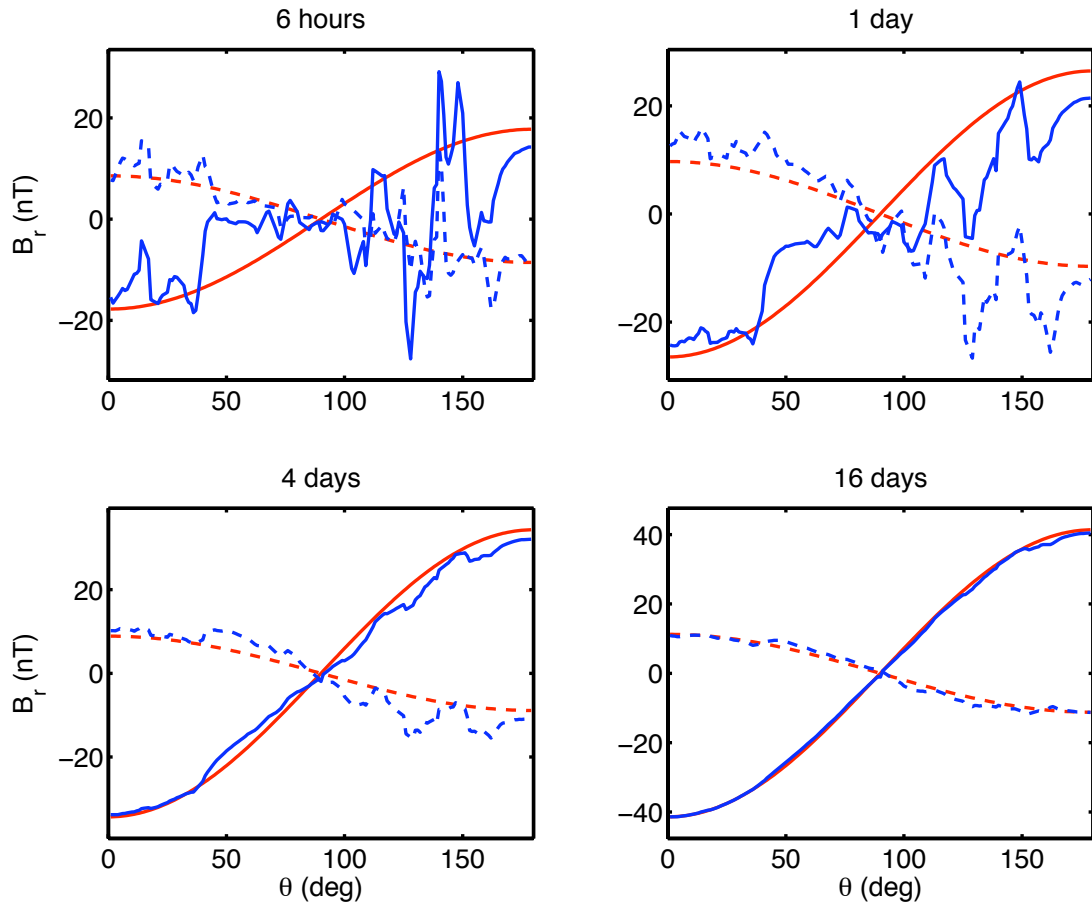


Figure 4.43: Meridional profiles of the real (solid) and imaginary (dashed) parts of B_r for longitude $\phi = 180^\circ$ in Model 6 for periods of 6 hours, 1 day, 4 days, and 16 days as calculated by the author with FlexPDE (blue). The red curves show the analytic solution for a model with the same 1D mantle conductivity, but without the surface conductance map.

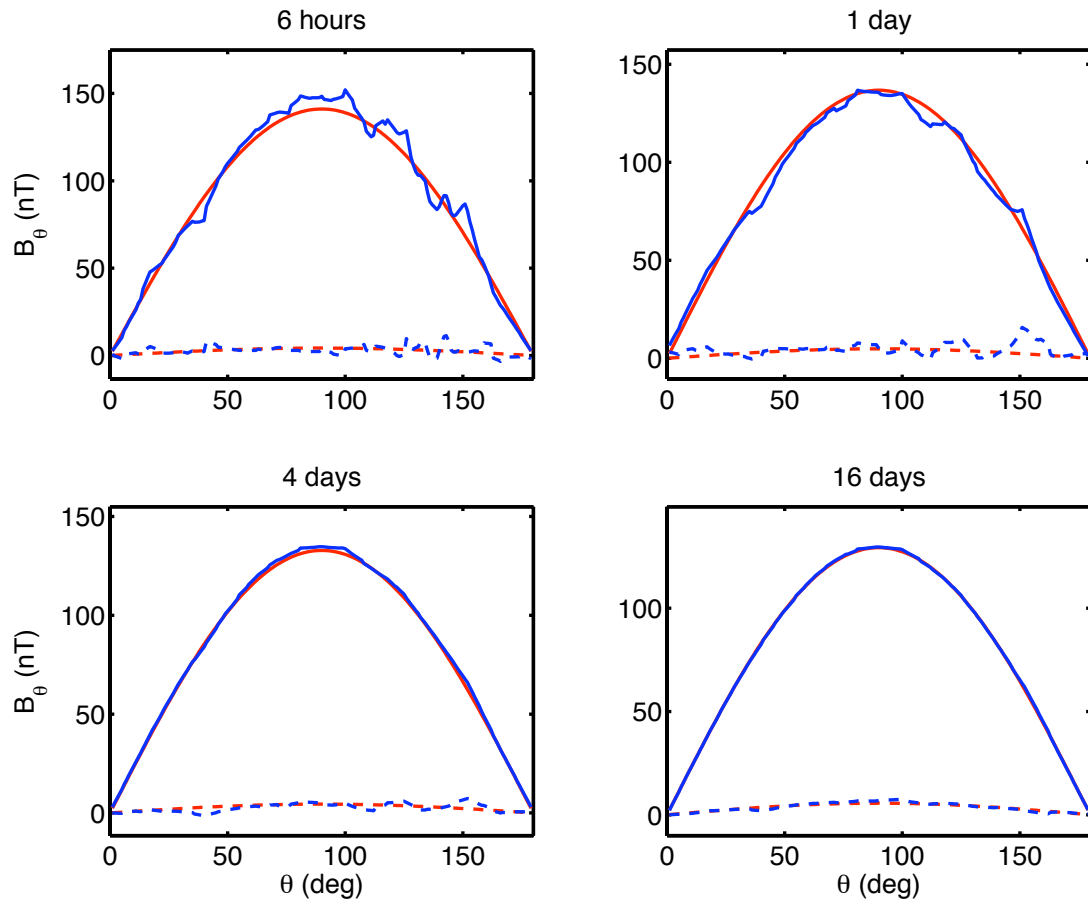


Figure 4.44: Meridional profiles of the real (solid) and imaginary (dashed) parts of B_θ for longitude $\phi = 180^\circ$ in Model 6 for periods of 6 hours, 1 day, 4 days, and 16 days as calculated by the author with FlexPDE (blue). The red curves show the analytic solution for a model with the same 1D mantle conductivity, but without the surface conductance map.

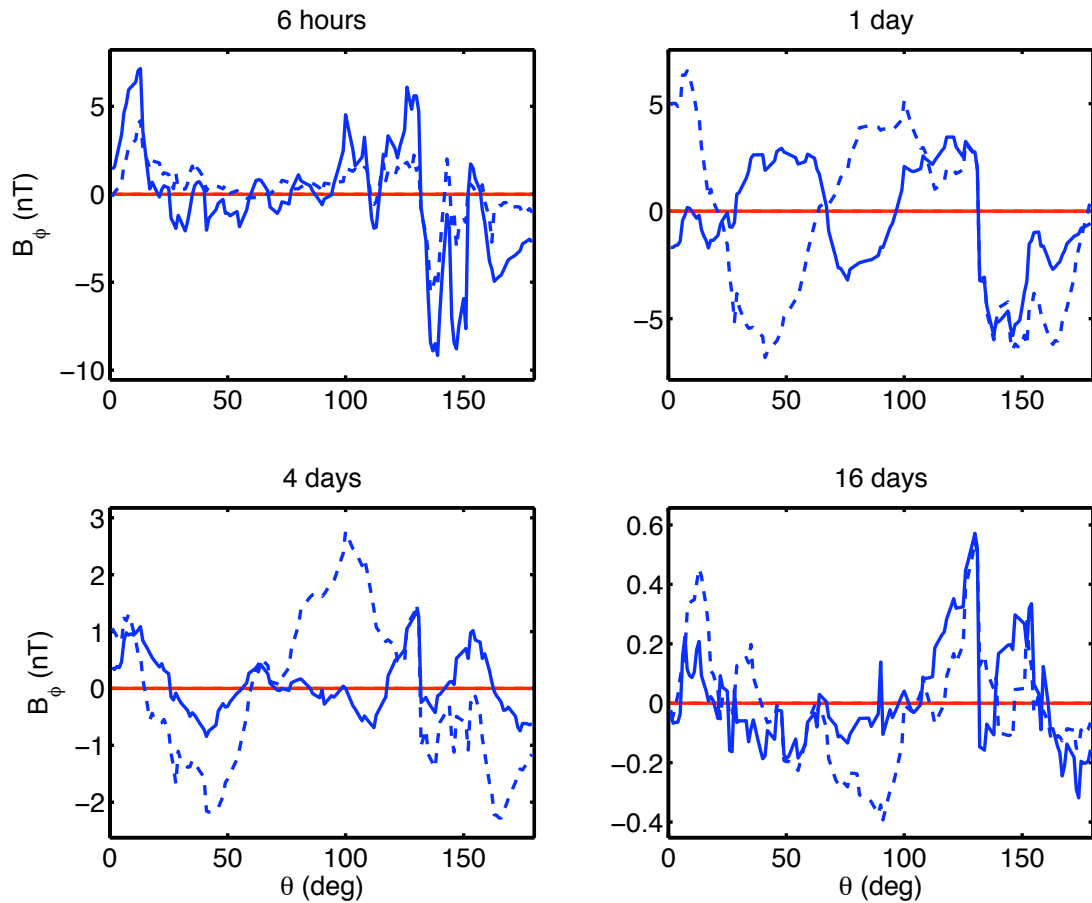


Figure 4.45: Meridional profiles of the real (solid) and imaginary (dashed) parts of B_ϕ for longitude $\phi = 180^\circ$ in Model 6 for periods of 6 hours, 1 day, 4 days, and 16 days as calculated by the author with FlexPDE (blue). The red curves show the analytic solution for a model with the same 1D mantle conductivity, but without the surface conductance map.

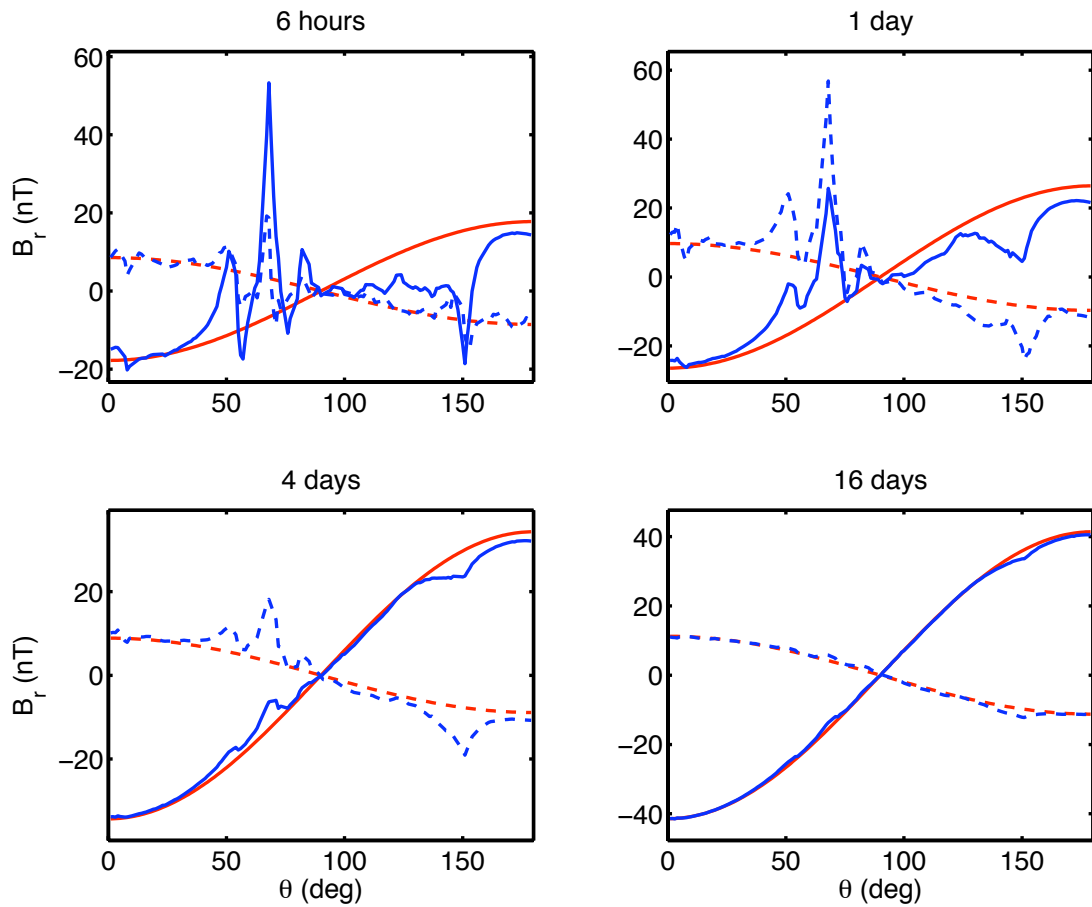


Figure 4.46: Meridional profiles of the real (solid) and imaginary (dashed) parts of B_r for longitude $\phi = 270^\circ$ in Model 6 for periods of 6 hours, 1 day, 4 days, and 16 days as calculated by the author with FlexPDE (blue). The red curves show the analytic solution for a model with the same 1D mantle conductivity, but without the surface conductance map.

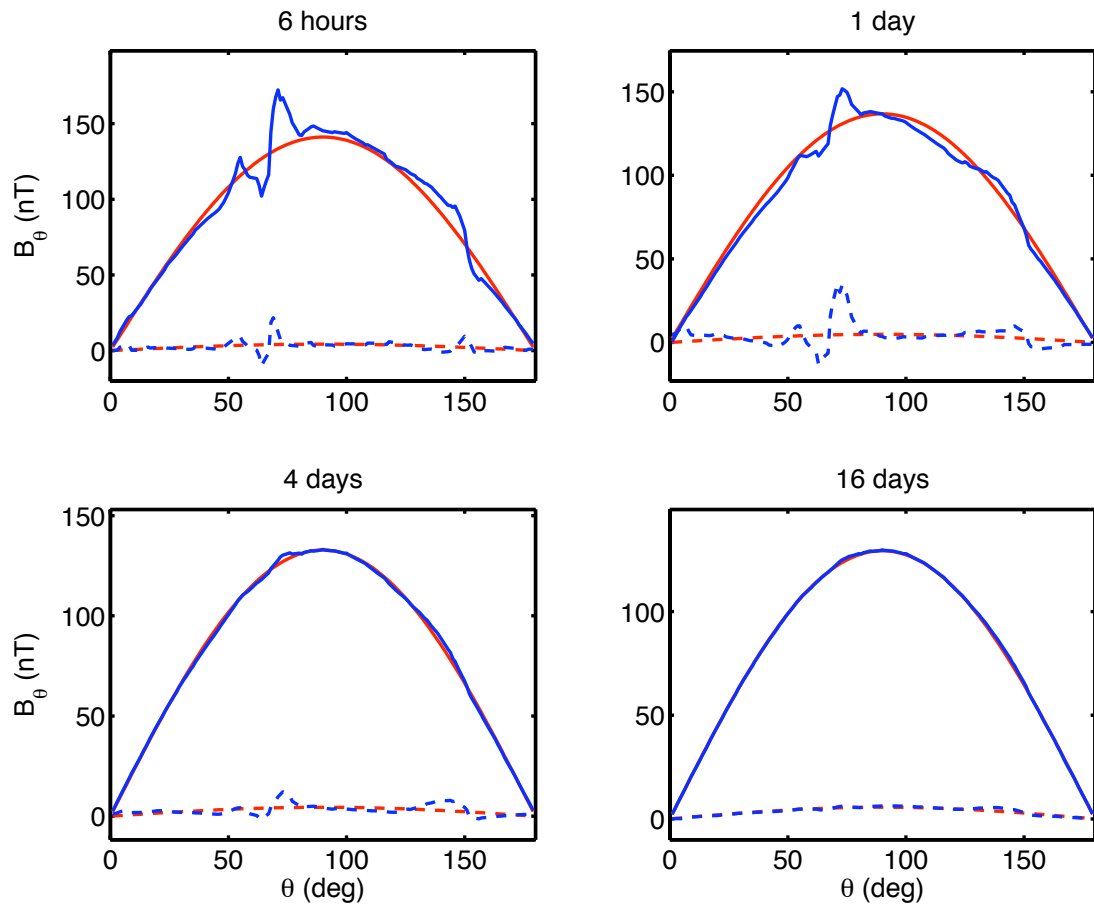


Figure 4.47: Meridional profiles of the real (solid) and imaginary (dashed) parts of B_θ for longitude $\phi = 270^\circ$ in Model 6 for periods of 6 hours, 1 day, 4 days, and 16 days as calculated by the author with FlexPDE (blue). The red curves show the analytic solution for a model with the same 1D mantle conductivity, but without the surface conductance map.

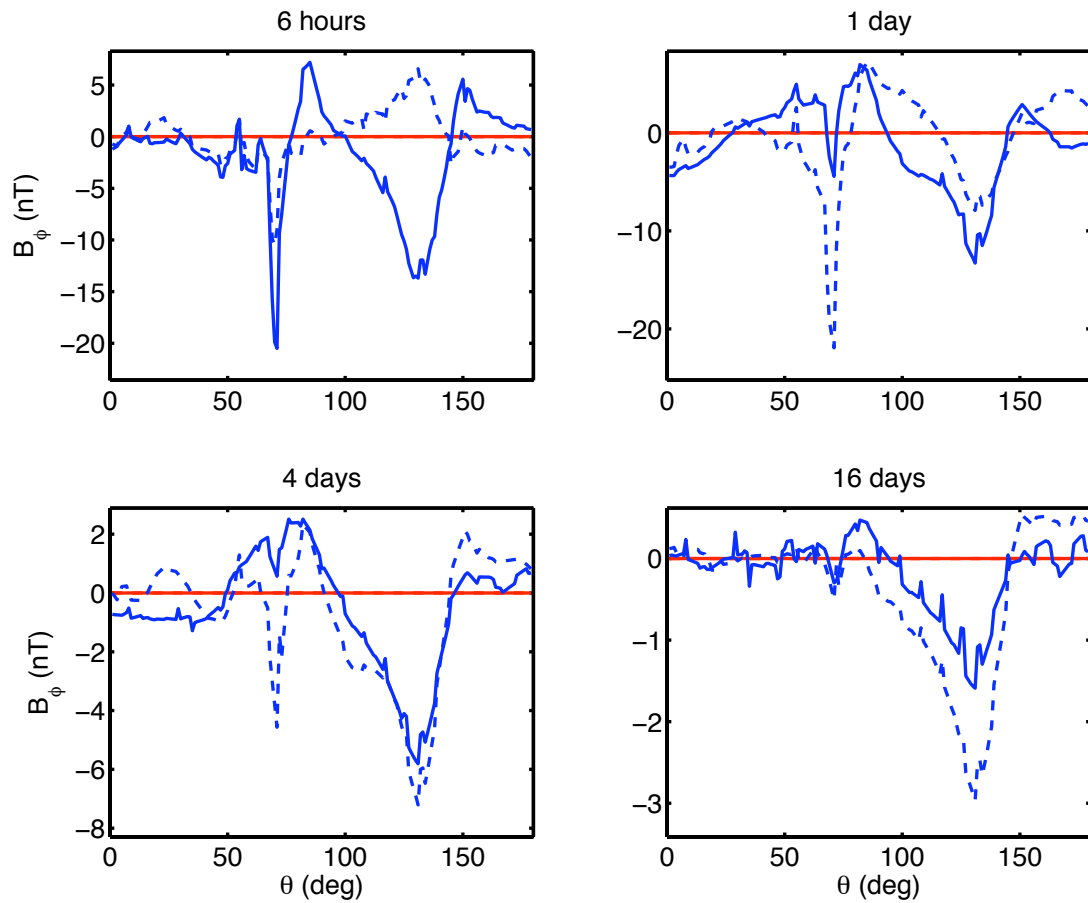


Figure 4.48: Meridional profiles of the real (solid) and imaginary (dashed) parts of B_ϕ for longitude $\phi = 270^\circ$ in Model 6 for periods of 6 hours, 1 day, 4 days, and 16 days as calculated by the author with FlexPDE (blue). The red curves show the analytic solution for a model with the same 1D mantle conductivity, but without the surface conductance map.

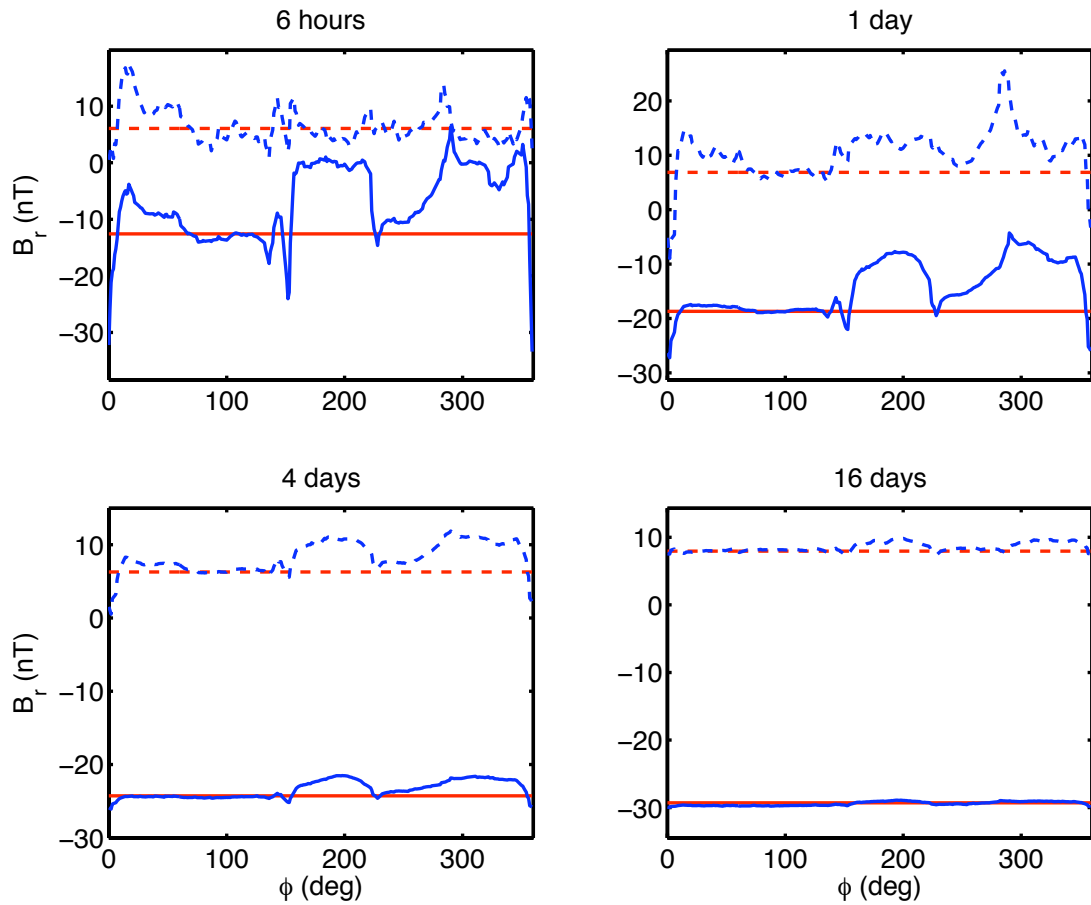


Figure 4.49: Azimuthal profiles of the real (solid) and imaginary (dashed) parts of B_r for longitude $\theta = 45^\circ$ in Model 6 for periods of 6 hours, 1 day, 4 days, and 16 days as calculated by the author with FlexPDE (blue). The red curves show the analytic solution for a model with the same 1D mantle conductivity, but without the surface conductance map.

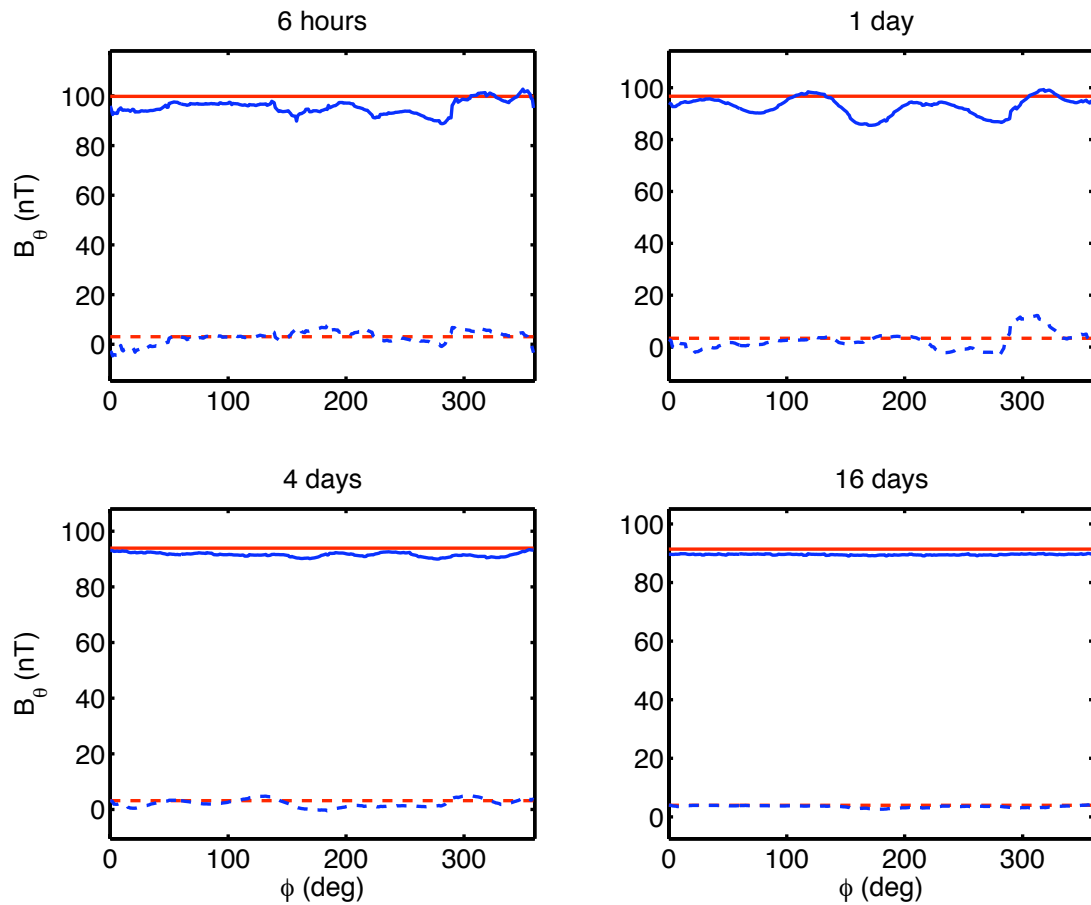


Figure 4.50: Meridional profiles of the real (solid) and imaginary (dashed) parts of B_θ for longitude $\theta = 45^\circ$ in Model 6 for periods of 6 hours, 1 day, 4 days, and 16 days as calculated by the author with FlexPDE (blue). The red curves show the analytic solution for a model with the same 1D mantle conductivity, but without the surface conductance map.

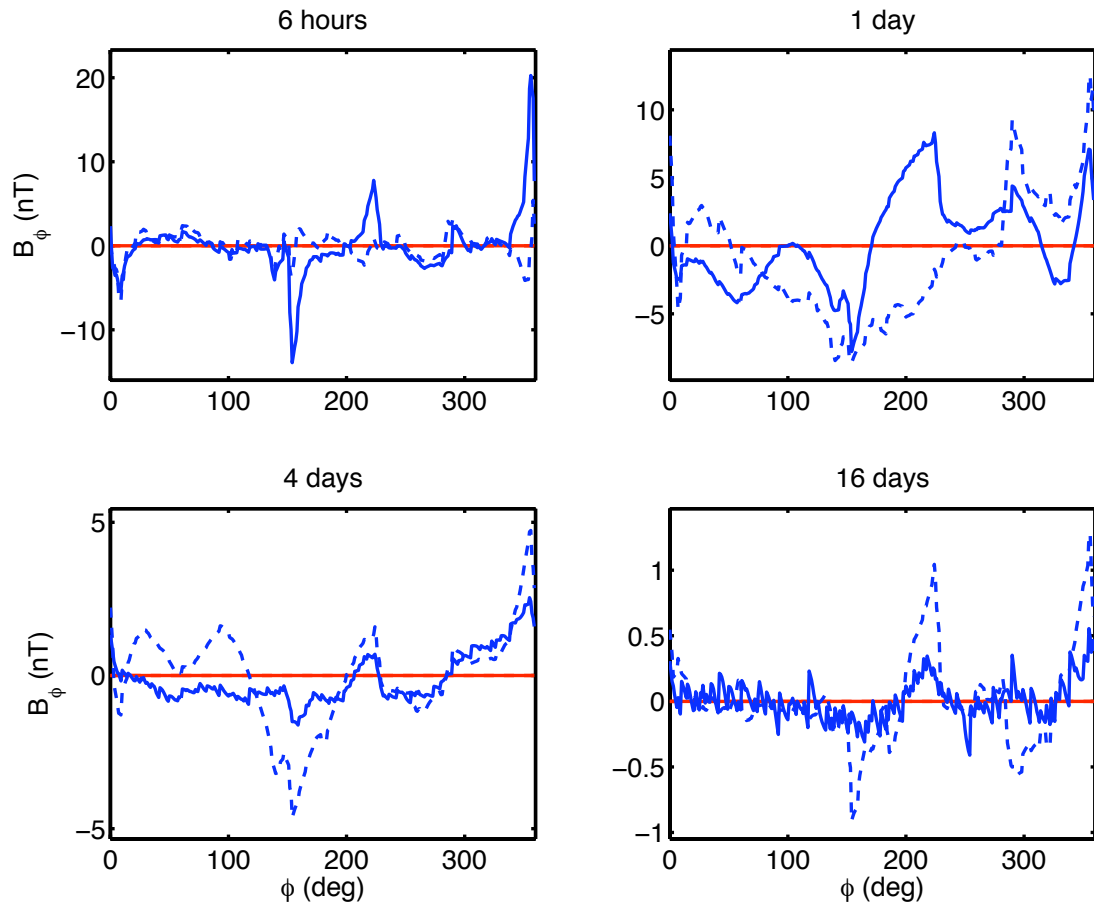


Figure 4.51: Meridional profiles of the real (solid) and imaginary (dashed) parts of B_ϕ for longitude $\theta = 45^\circ$ in Model 6 for periods of 6 hours, 1 day, 4 days, and 16 days as calculated by the author with FlexPDE (blue). The red curves show the analytic solution for a model with the same 1D mantle conductivity, but without the surface conductance map.

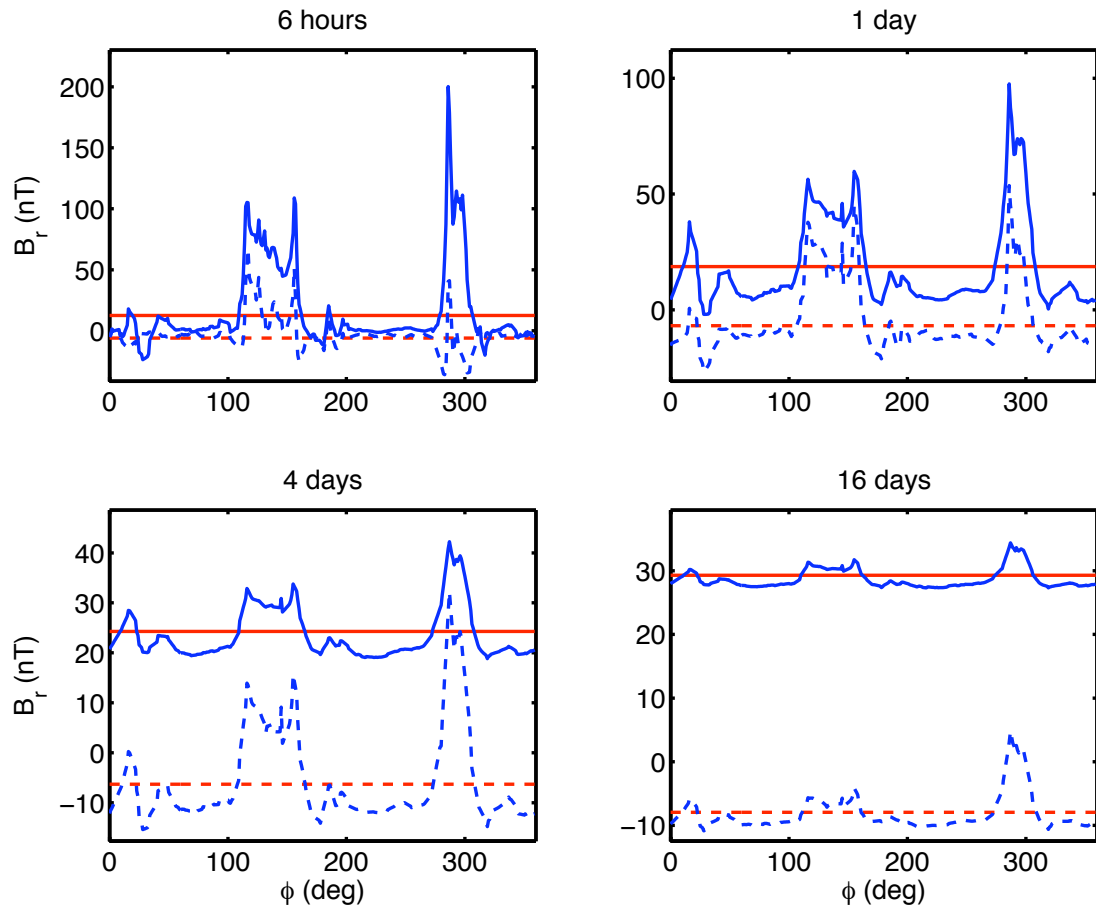


Figure 4.52: Azimuthal profiles of the real (solid) and imaginary (dashed) parts of B_r for longitude $\theta = 135^\circ$ in Model 6 for periods of 6 hours, 1 day, 4 days, and 16 days as calculated by the author with FlexPDE (blue). The red curves show the analytic solution for a model with the same 1D mantle conductivity, but without the surface conductance map.

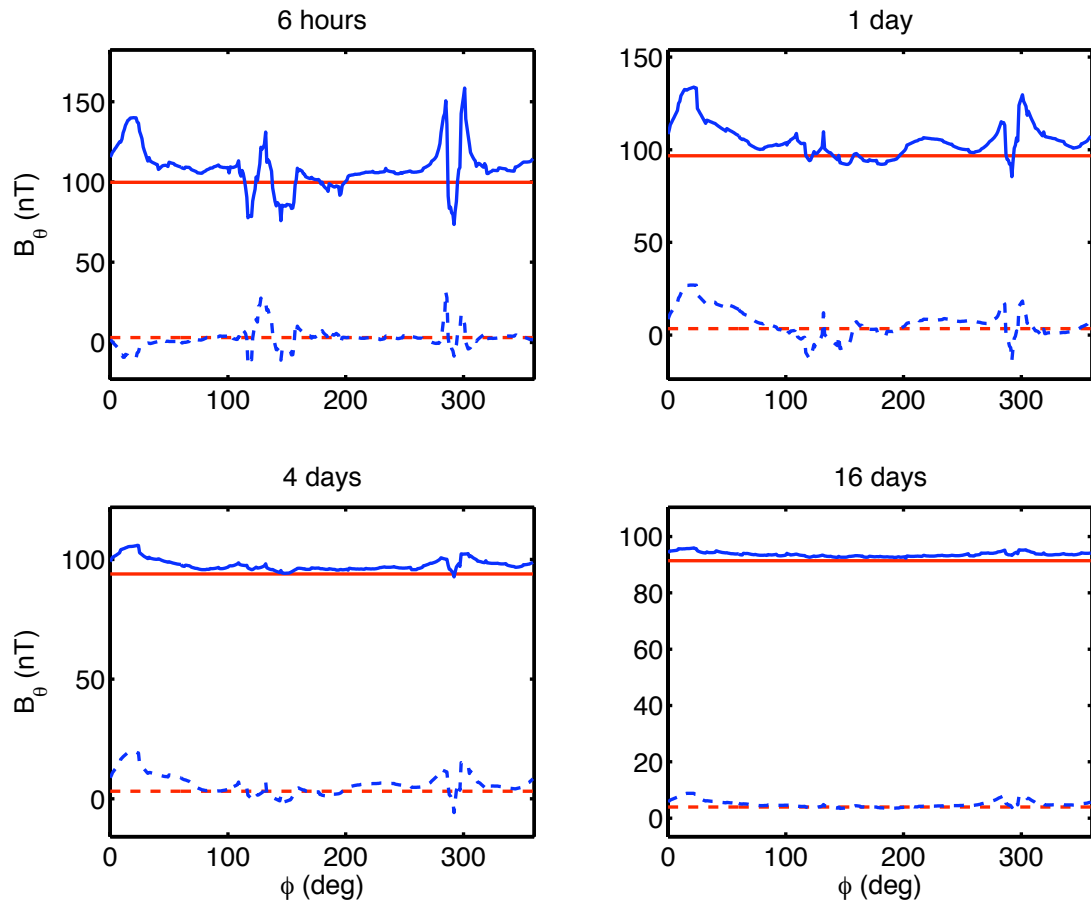


Figure 4.53: Meridional profiles of the real (solid) and imaginary (dashed) parts of B_θ for longitude $\theta = 135^\circ$ in Model 6 for periods of 6 hours, 1 day, 4 days, and 16 days as calculated by the author with FlexPDE (blue). The red curves show the analytic solution for a model with the same 1D mantle conductivity, but without the surface conductance map.

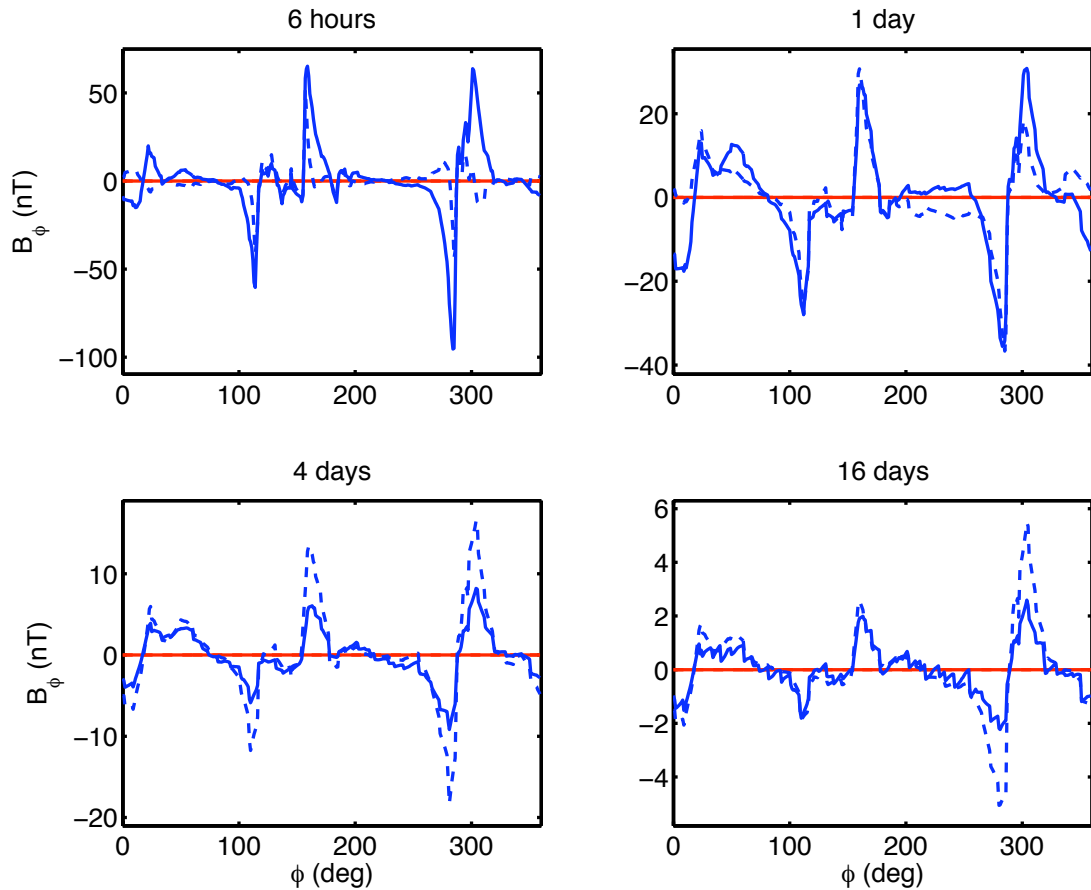


Figure 4.54: Meridional profiles of the real (solid) and imaginary (dashed) parts of B_ϕ for longitude $\theta = 135^\circ$ in Model 6 for periods of 6 hours, 1 day, 4 days, and 16 days as calculated by the author with FlexPDE (blue). The red curves show the analytic solution for a model with the same 1D mantle conductivity, but without the surface conductance map.

4.6 Summary

FlexPDE solutions have been calculated for the magnetic fields in four global benchmark models, and show good agreement with the other available solutions, especially for B_r and B_θ . The solutions for B_ϕ are slightly noisier than the other two, but not excessively so. The FlexPDE solutions for azimuthally asymmetric models which include a surface conductance show systematic differences from bimodal solutions, particularly at short periods near coastlines. At longer periods these differences become minimal. The differences between bimodal and unimodal solutions with respect to the coast effect are easily distinguished in the presence of discontinuities in surface conductance. When other researchers provide solutions for Model 6, it will be possible to quantify how pronounced these artifacts are in the presence of more realistic conductances that are spatially continuous.

4.7 Acknowledgments

This work was supported by NASA Headquarters under the NASA Earth and Space Science Fellowship Program - Grant NNX07AQ94H. The author would also like to thank Cathy Constable for guidance and collaboration on this work, Alexei Kuvshinov for useful discussions and for providing his numerical solutions for Models 1 and 2, and Jakub Velimský for providing his numerical solutions for Models 1 and 2 and analytic solutions for Model 3.

References

- Constable, S., 1993: Constraints on mantle electrical conductivity from field and laboratory measurements. *J. Geomagn. Geoelectr.*, **45**(9), 7070–728.
- Everett, M., Constable, S., and Constable, C., 2003: Effects of near-surface conductance on global satellite induction responses. *Geophys. J Int.*, **153**(1), 277–286.
- Everett, M., and Schultz, A., 1996: Geomagnetic induction in a heterogenous sphere: Azimuthally symmetric test computations and the response of an undulating 660-km discontinuity. *J. Geophys. Res.*, **101**(B2), 2765–2783.
- Jeanloz, R., 1990: The nature of the earth’s core. *Annual Review of Earth and Planetary Sciences*, **18**(1), 357–386.
- Kuvshinov, A., Avdeev, D., and Pankratov, O., 1999: Global induction by sq and dst sources in the presence of oceans: bimodal solutions for non-uniform spherical surface shells above radially symmetric earth models in comparison to observations. *Geophys. J Int.*, **137**(3), 630–650.
- Kuvshinov, A., Avdeev, D., Pankratov, O., Golyshev, S., and Olsen, N., 2002a: Modelling electromagnetic fields in a 3d spherical earth using a fast integral equation approach. *Methods in Geochemistry and Geophysics*, **35**, 43–54.
- Kuvshinov, A., Olsen, N., Avdeev, D., and Pankratov, O., 2002b: Electromagnetic induction in the oceans and the anomalous behaviour of coastal c-responses for periods up to 20 days. *Geophys. Res. Lett.*, **29**(12), 14409.
- Martinec, Z., 1998: Geomagnetic induction in multiple eccentrically nested spheres. *Geophys. J Int.*, **132**(1), 96–110.
- Parker, R., 1968: Electromagnetic induction in the oceans. In *The Sea*, editor A. Maxwell, 695–730. Wiley.
- Uyeshima, M., and Schultz, A., 2000: Geoelectromagnetic induction in a heterogeneous sphere: a new three-dimensional forward solver using a conservative staggered-grid finite difference method. *Geophys. J Int.*, **140**(3), 636–650.

- Velínský, J., and Martinec, Z., 2005: Time-domain, spherical harmonic-finite element approach to transient three-dimensional geomagnetic induction in a spherical heterogeneous earth. *Geophys. J Int.*, **161**(1), 81–101.
- Weiss, C., 2010: Triangulated finite difference methods for global-scale electromagnetic induction simulations of whole mantle electrical heterogeneity. *Geochem. Geophys. Geosyst.*, **11**(11), Q11010.

Chapter 5

Conclusions and Future Outlook

The work presented in this document describes new and flexible tools and methods for forward-modeling the global induction problem with a combination of numerical and analytic techniques. These methods allow for nearly arbitrary conductivity and primary field models, and include the ability to account for surface conductance and Earth rotation.

In Chapter 2 the numerical methods were shown to accurately calculate the magnetic fields for global induction problems with analytic solutions including concentric spheres, eccentrically nested spheres, and rotating uniform conductors in uniform primary fields. While the accuracy of the solution is highly dependent on model parameters, solution options, and measurement locations, errors of less than 1% are attainable for the problems we describe. The method is sufficiently powerful to model complicated and scientifically interesting problems, but they are specified in a short and fairly simple script. This means that new variations can be created in a short amount of time by a researcher with mathematical and physical expertise, but little FEM experience.

We demonstrated in Chapter 3 that it is possible to recreate the previously reported bias in local time $c_1(\omega)$ estimates by including coherent, non-zonal structure in the primary fields, but that the magnitude of the asymmetry in these fields must be larger than that empirically estimated by other researchers. We showed that the biasing effect of non-zonal structure is more influenced by the geometry of the fields than the discrepancy in the magnitude of the response functions for higher

degree structure, and that the addition of Y_2^1 structure to a primary field that is otherwise purely dipolar is more effective at biasing c_1 than longitude weighting of the dipolar primary field. We also demonstrate that, if present, non-zonal structure in the primary field causes greater bias in response functions estimated from scalar anomaly measurements than from vector component measurements. With little modification, the methods described in this chapter could be adapted for use with inclusion of other spherical harmonic terms in the primary fields. This may be useful as the structure of Earth's primary fields become known with greater precision.

Finally, in Chapter 4 we showed that the FlexPDE magnetic field solutions show good agreement with the solutions from other numerical techniques for two models with radial conductivity in heterogeneous surface conductance, but show some systematic differences from bimodal solutions near coastlines at short periods. The FlexPDE solutions for a non-concentric nested spheres model agree well with analytic results, while the solutions for the most realistic model considered, which includes a metallic core and Earth-like surface conductance, qualitatively reproduce the coast effect at short periods.

The FlexPDE method could be advanced by allowing for bimodal induction in the formulation of the surface conductance boundary condition, which would account for the known vertical leakage currents connecting the ocean and upper mantle. This would increase the accuracy of simulated coast effects. Another possibility is the formulation of a far-field boundary condition that could be imposed at the edge of modeled space. The resulting reduction in the size of the models would make it possible to decrease the runtimes and memory requirements, to calculate solutions of even greater accuracy, and/or to add conductivity structure that is too small to be included in the current computational meshes.

The numerical techniques described here could be easily adapted to other global induction problems, including studies of the outward propagation of the secular variation of Earth's core field through the mantle, sensitivity and resolution studies for GDS explorations of the D'' layer, explorations of the limits and possibilities of new and existing response functions for primary fields with complicated

source fields and lateral variations in conductivity, and for conductivity studies of other planets and moons with global magnetic fields. With a small modification of the script, solutions for localized flat-Earth models can be calculated in 2 and 3 dimensions, and MT and CSEM problems could be explored with the inclusion of electric fields in the calculations.